ALGORITHM THEORETICAL BASIS DOCUMENT (ATBD)

for the

SENSOR DATA RECORD (SDR) ALGORITHM

LIMB PROFILER
OZONE MAPPING AND PROFILER SUITE (OMPS)

NATIONAL POLAR-ORBITING OPERATIONAL ENVIRONMENTAL SATELLITE SYSTEM PREPARATORY PROJECT (NPP)

Prepared by

Glen Jaross, Science Systems and Applications Inc, Lanham, Maryland

Co-authors
Didier F. Rault, NASA Langley Research Center, Hampton, Virginia

Mark Kowitt, Grace Chen, Michael Haken
Science Systems and Applications Inc, Lanham, Maryland

Table of Contents

Abbreviations

ADC	Analog to Digital Converter
APID	Application Packet Identification
BATC	Ball Aerospace and Technology Corporation
CCD	Charge-Coupled Device
CHG	Center High Gain
CLG	Center Low Gain
EDR	Environmental Data Record
FWHM	Full Width at Half Maximum
HDF5	Hierarchical Data Format version 5
IFOV	Instantaneous Field Of View
IPO	Integrated Program Office
LED	Light-Emitting Diode
LHG	Left High Gain
LLG	Left Low Gain
LP	Limb Profiler
LPS	Linear Polarization Sensitivity
MEB	Main Electronics Board
NIR	Near-InfraRed
NIST	National Institute of Standards and Technology
NP	Nadir Profiler
NPP	NPOESS Preparatory Project
OMPS	Ozone Mapping and Profiler Suite
PSF	Point Spread Function
RDR	Raw Data Record
RHG	Right High Gain
RLG	Right Low Gain
SDR	Sensor Data Record
SNR	Signal to Noise Ratio
TC	Total Column
UV	UltraViolet
VIS	Visible

1 INTRODUCTION

This document provides the physical theory and mathematical background underlying the Ozone Mapping and Profiler Suite (OMPS) / Limb Profiler (LP) Sensor Data Record (SDR) algorithm. The SDR algorithm is the step in the data processing chain that takes Raw Data Records (RDRs) from the sensor and converts them into a form suitable for use by retrieval algorithms. The approach used to process the OMPS/LP sensor data is described, as is the mathematical basis for the correction algorithms. This document also identifies the sources of input data that are required by the algorithms and describes the SDR primary products.

This document is sub-divided into 5 primary sections. The introduction provides general information on the OMPS mission, and details of the OMPS Limb sensor design. This section also includes a brief overview of pre-launch sensor characterizations and describes how the sensor is operated. The remaining sections describe in turn the main components of the algorithm, beginning with an overview of the SDR process and how it relates to subsequent retrieval algorithms. Though this document is not a description of data flow, an outline of the structure is necessary to understand the relationship between components.

1.1 OMPS mission overview: objectives and scope

The OMPS suite is a main component of the National Polar-Orbiting Operational Environmental Satellite System (NPOESS). *OMPS* is one of the five instruments manifested on the NPOESS Preparatory Project (NPP) satellite, with a scheduled launch in Spring 2011. The OMPS dataset is aimed at building up the Environmental Data Records (EDRs) to describe the global vertical, horizontal and temporal distribution of ozone in the Earth's atmosphere.

OMPS was conceived *[Graf et al., 2000; Leitch et al., 2003]* and built to allow the scientific community to continue the long-term record of ozone and aerosol measurements initiated more than 30 years ago by the Stratospheric Aerosol and Gas experiment (SAGE) family of sensors *[McCormick, 1989, Mauldin, 1998]*, the *Total Ozone Mapping Spectrometer* (TOMS) *[McPeters, 1991]* and the Solar Backscatter Ultraviolet Instrument (SBUV) *[Heath et al. (1975), Frederick et al. (1986), and Hilsenrath et al. (1995)]*.

1.2 OMPS Mission description

The OMPS instruments were designed and built by Ball Aerospace and Technology Corporation (BATC) under contract from the Integrated Program Office (IPO). As described by *[Flynn et al., 2007]* and as shown in Figure 1-1, OMPS is composed of three instruments, namely the Total Column mapper (TC), the Nadir Profiler (NP) and the Limb Profiler (LP). These three instruments have heritage respectively from TOMS, SBUV and the Shuttle Ozone Limb Sounding

Experiment//Limb Ozone Retrieval Experiment (SOLSE/LORE) *[McPeters et al., 2000]*. The nadir system has two focal planes; one operating from 300 to 380 nm for total column ozone observations; the other operating at 250 to 310 nm for profile ozone observations. The limb system has one focal plane operating from 290 to 1000 nm for high vertical resolution profile ozone observations. The three instruments were designed to be flown as a suite, though the Limb and Nadir instruments can be separated and the Profiler can be eliminated from the Nadir portion.

The suite was designed to fly in a sun-synchronous, polar orbit with a local time at the ascending node (LTAN) between 0930 hr. and 1430 hr. The first OMPS mission will be on the NPP satellite, which will operate in a near circular, sun-synchronous orbit, with a 1330 hr ascending-node orbit and an altitude of 824 km.

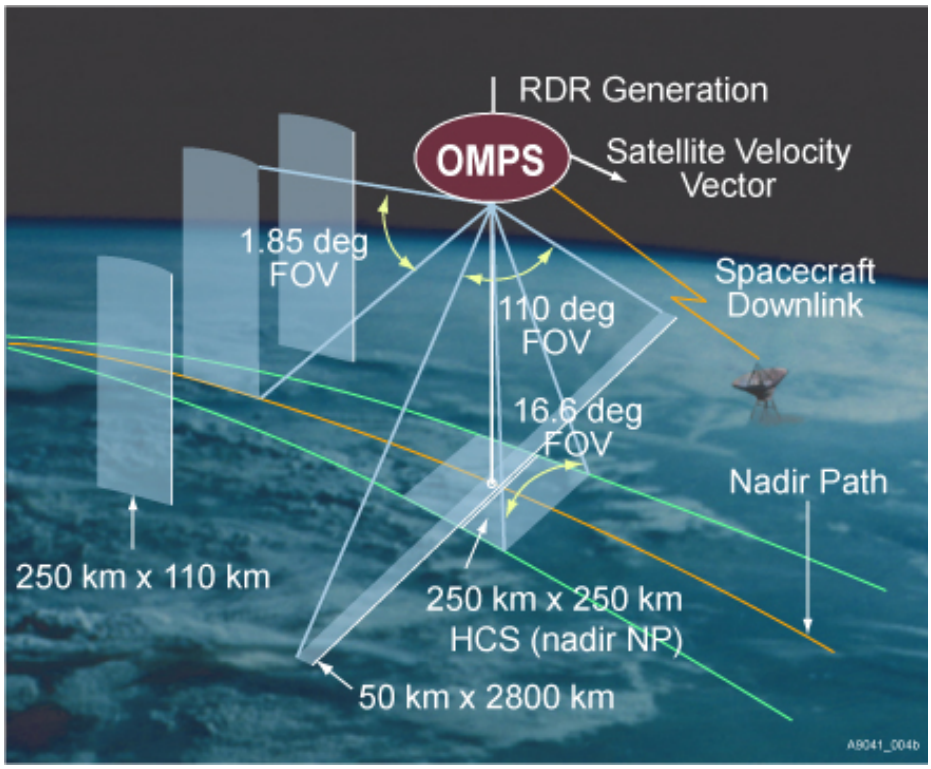

Figure 1-1 OMPS instruments: TC, NP and LP sensors. The OMPS/LP views the Earth's limb through three thin vertical slits (approximately 105 km extent at tangent point) in the spacecraft aft direction. (Courtesy of BATC)

1.3 OMPS/LP mission objectives

Unlike the OMPS Nadir sensors, OMPS/LP is not an operational sensor. This means that there are no requirements levied by the IPO to produce derived products with a specific frequency or with specific users in mind. The IPO does require that RDRs are produced, but this is subordinate to the

production of Nadir RDRs. In other words, should an operational conflict arise between Limb and Nadir measurements, the latter have priority.

The OMPS/LP sensor is programmatically a "research" instrument. The OMPS/LP sensor has no performance requirements, though the sensor was designed, built, and tested with specific product performance objectives in mind. The objectives, listed in Table 1-1, are treated as goals rather than hard requirements. The product objectives were in turn used to derive sensor performance objectives. The sensor performs at or above these objectives in most areas, and to the extent that this is a predictor for product performance OMPS/LP should be capable of meeting the Table 1-1 objectives.

Table 1-1 OMPS/LP Ozone Measurement Objectives

Item	Performance
Horizontal Cell Size	250 km
Vertical Cell Size	3 km
Horizontal Coverage	≤ 80° solar zenith angle
Vertical Coverage	Tropopause – 60 km
Measurement Range	0.1 – 15 ppmv (0.3 lower limit: tropopause – 25 km)
Measurement Accuracy	Greater of 20% or 0.1 ppmv (tropopause – 15 km) Greater of 10% or 0.1 ppmv (15 km – 60 km)
Measurement Precision	10% (tropopause – 15 km) 3% (15 km – 50 km) 10% (50 km – 60 km)
Long-term Stability	2% over 7 years
Mapping Uncertainty	25 km
Local Average Revisit Time	4 days

The OMPS/LP mission will be considered successful if it meets the following objectives.

(1) Produce high quality ozone profile products from all sensor data collected.
(2) Characterize the sensor on-orbit performance.
(3) Evaluate sensor capabilities toward meeting performance objectives.
(4) Investigate SDR and EDR algorithms to meet and improve upon product performance objectives.

Efficient ozone retrievals are essential to meeting these 4 objectives. Timely evaluation of data quality and sensor performance requires that the data are processed as fast as collected. Repeated reprocessing of the full data collection is also an important aspect of improving data quality. As a consequence of these requirements an additional objective is to perform SDR + EDR processing in 3-5 CPU minutes per sensor slit.

1.4 The Limb Scatter method

The OMPS/LP is a Limb Scatter (LS) sensor. It is designed to observe the Earth's limb radiance in the 290-1000 nm spectral range where the prime source of light is solar irradiance scattered back to space by atmospheric molecules (Rayleigh scatter), suspended liquid and solid particulates (aerosols), clouds, and the Earth's surface.

To interpret the radiance measurements made by the OMPS/LP sensor requires an understanding of how the Earth's atmosphere interacts with Ultraviolet (UV), visible (VIS), and near infrared (NIR) radiances. Incoming solar radiation undergoes Rayleigh scattering and absorption by atmospheric constituents such as ozone and aerosols. Radiation that reaches the ground is scattered by surfaces of widely varying reflectivity. To retrieve ozone vertical distribution from the tropopause to 60 km, a series of spectral channels are selected to observe a range of strongly absorbing to weakly absorbing features in the Hartley-Huggins and Chappuis bands. Within these ozone bands, absorption by other atmospheric components is relatively negligible. The ozone absorption coefficients differ from band to band, with the strongest absorption at shorter wavelengths. The stronger the absorption, the higher the altitude at which the atmosphere becomes optically thick. Consequently, measurements of scattered radiation at shorter wavelengths yield information on the ozone profile at higher levels of the atmosphere than measurements at longer wavelengths.

In order to retrieve ozone vertical profiles it is unnecessary to measure radiances at all wavelengths over the full extent of the required vertical range. Radiances at each wavelength are typically used over only 15 km, sometimes less, sometimes more. This greatly reduces the requirements for sensor calibration and the volume of data brought down from the instrument. One technique used by many retrieval algorithms to reduce sensitivity to calibration errors is altitude normalization. The ratio of a radiance measured at one altitude to another measured at a much higher altitude varies less with changes in the underlying surface reflectivity than does the unnormalized radiance. As a consequence radiances are needed over a greater altitude range. The reduced need for calibration accuracy outweighs any disadvantage of the broadened altitude range.

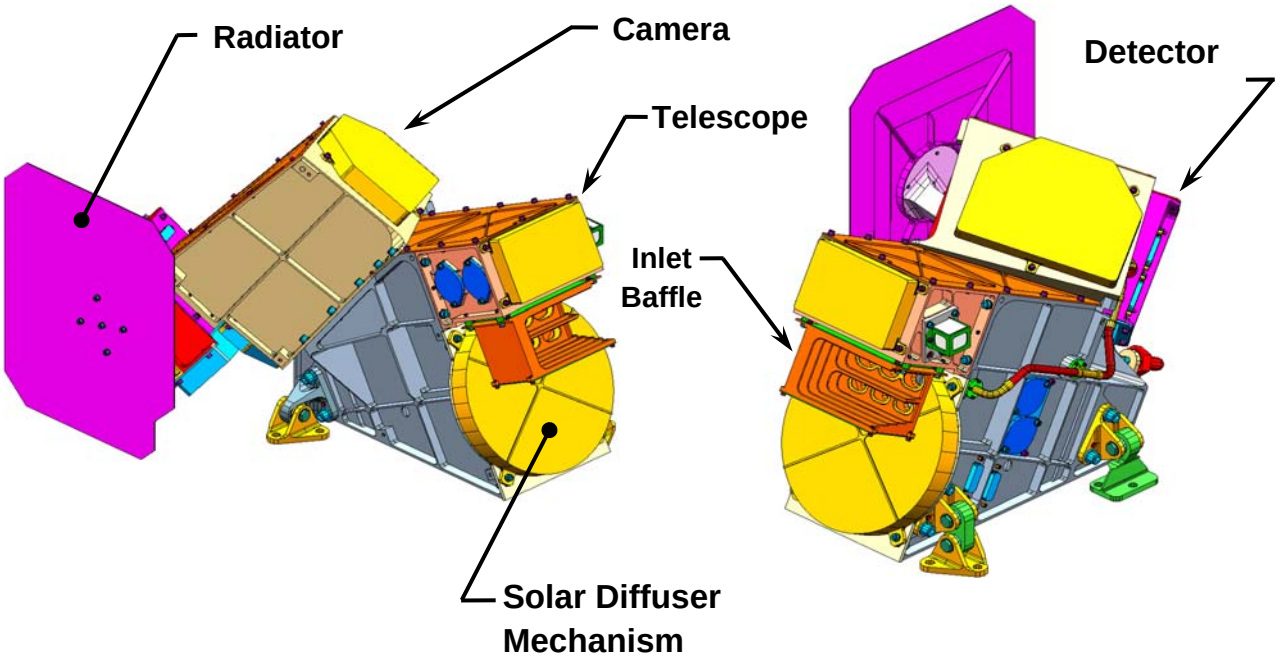

Figure 1-2 The OMPS LP instrument viewed upside down, as in the laboratory. The 27° tilt relative to the spacecraft platform places the field of view at the Earth limb. Solar measurements are obtained through transmissive diffusers that rotate in front of the entrance apertures. (Courtesy of BATC)

1.5 OMPS/LP sensor description

The OMPS/LP sensor simultaneously images the whole vertical extent of the Earth's limb, with a fixed vertical Field-Of-View (FOV) of about 1.85° covering the 10-60 km nominal altitude range after allowing for boresight misalignment, spacecraft pointing error, and orbit altitude variation. The instrument boresight points down approximately 27° relative to the spacecraft velocity vector in order to image the limb. It is a triple-slit prism spectrometer that senses the limb radiance and solar irradiance over the wavelength range of 290 to 1000 nm. One of the slits is centered on the satellite ground track while the other two are pointing 4.25 deg (250 km) on either side (see Figure 1-1).

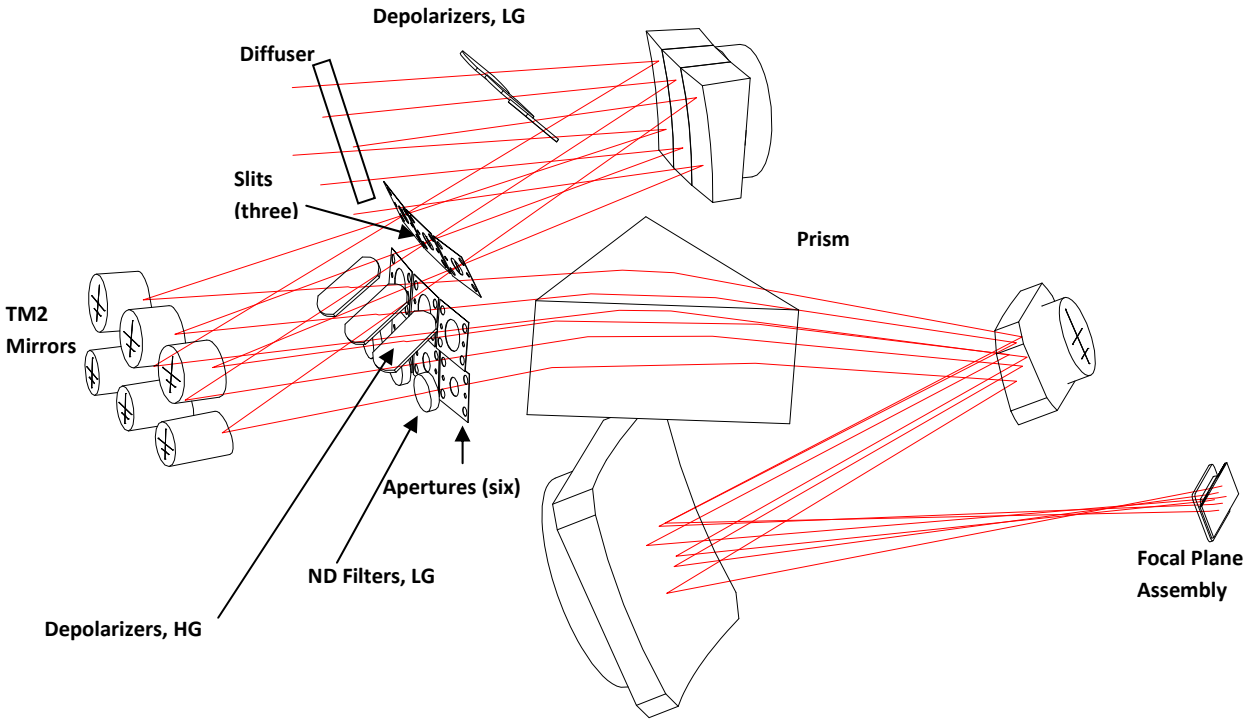

Figure 1-3 Optical layout of the OMPS LP instrument. In this diagram, HG refers to the 3 high gain (i.e. large) apertures, and LG refers to the 3 low gain (i.e. small) apertures. (Courtesy of BATC)

Light entering the OMPS/LP instrument slits (see Figure 1-3) is dispersed by a prism and focused onto a single two-dimensional Charged Couple Device (CCD) detector. The prism dispersion is uniquely suited for the OMPS/LP, providing high spectral resolution in the features-rich UV region and lower resolution in the somewhat featureless VIS and NIR regions, as shown in Figure 1-4.

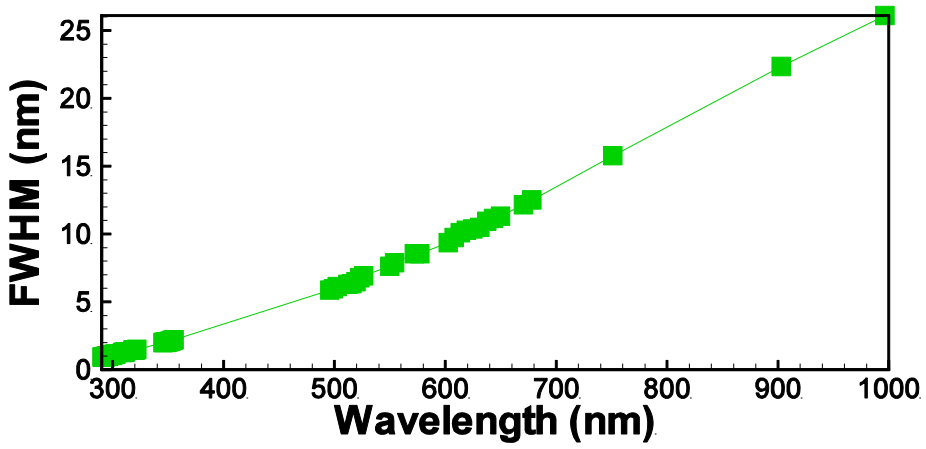

Figure 1-4 OMPS/LP dispersion characteristics. The prism produces variable spectral resolution, from 1 nm in the Ultraviolet to 25 nm in near InfraRed.

1.5.1 Earth-view measurements

The primary technical challenge associated with Limb Scatter measurements is the large dynamic range of the limb signal, which typically varies by 4-5 orders of magnitude across the spectral/spatial ranges of interest. The sensor accommodates this dynamic range while maintaining adequate signal-to-noise ratios (SNR) through the use of 4 gain levels, 2 optical and 2 electronic. Light entering each slit passes through a small and a large aperture, thus producing six complete limb images on the CCD focal plane (see Figure 1-5). The large apertures (high gain) collect approximately 4 times the photons collected by the small apertures (low gain). Additionally, two different integration times are used to create a short and a long exposure image of the CCD. Both the short and the long images are made of a series of sub-exposures (15 short frames and 10 long frames) that are interleaved and co-added on-board the spacecraft. The pattern of exposures during the 18.7 sec report period is S:L:S:L:S, S:L:S:L:S, S:L:S:L:S, S:L:S:S:L, S:L:S:L:S. The number of photons collected in the short and long images differs by a factor of 30. The OMPS/LP sensor thus produces four simultaneous limb images per slit with gain ratios up to 120.

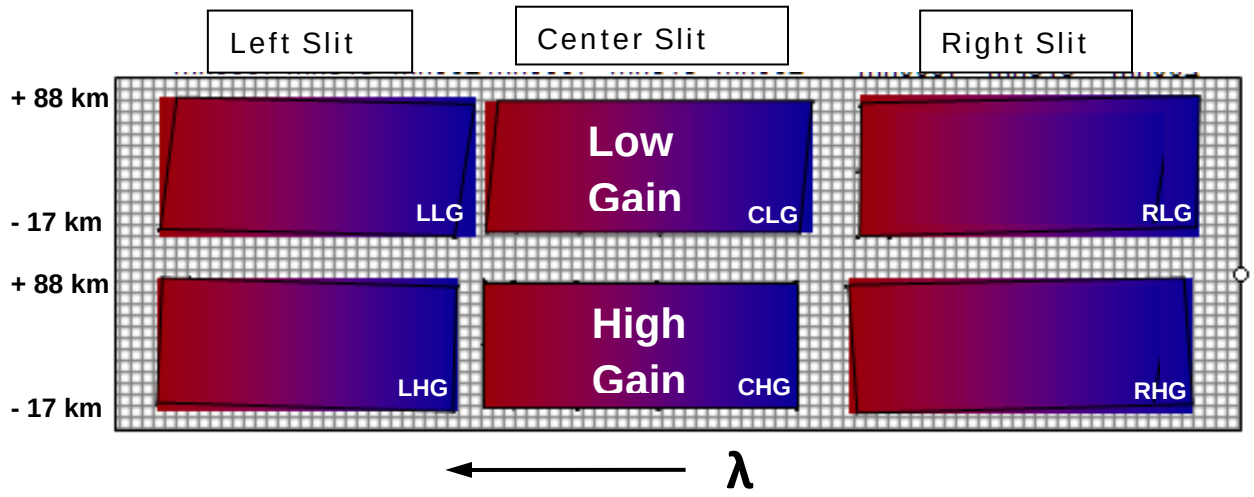

Figure 1-5 OMPS/LP CCD array layout. The three slits are imaged onto a single 740x340 CCD array. Each slit image passes through 2 apertures - low and high gain. The 6 aperture images are labeled with the 3-letter mnemonics as shown. UV and visible filters are used to reduce cross-channel straylight. Altitude extent of slits assumse a boresight at 35 km tangent height. (Courtesy of BATC)

Since a full limb image is always collected in all 4 gains, some of the images will contain saturated pixels. This situation is illustrated in Figure 1-6. When a pixel at a given wavelength and tangent altitude saturates, a pixel in the next lower gain can be used in its place, unless it too is saturated. Sensor timing and signal amplification have been set so that the lowest gain (low gain, short integration time) image never saturates. Since radiances decrease with altitude, multiple gains are needed to obtain a full radiance profile at most wavelengths. A low gain can be used at high altitudes, but the SNR will be lower than when using a higher gain.

The detector provides approximately 200 spectral channels for each detector image, but the available data rate limits the number that can be sent to the ground.

Table 1-2 OMPS/LP instrument design specifications

Item	Specification
Spectral range	290 - 1000 nm
Spectral sampling interval	2 pixels per Full Width Half Maximum (FWHM)
Spectral resolution (FWHM)	1 - 30 nm (prism)
Field-of-View (FOV)	1.85° (3 slits, 4.25 deg apart)
CCD Pixel FWHM	1-1.5 km in elevation, 3 km in azimuth
Integration times	Long: 1.248 second, coadded 10 times Short: 0.040 second, coadded 15 times
Signal processing	A/D conversion: 14 bit, Co-add register: 24 bit
Maximum data rate	196 kbits/second
Revisit time	4 days (average)
Vertical coverage	Tropopause — 60 km
Vertical cell size	resolution: 2 km, sampling: 1 km
SNR	320 (290nm at 60km) to 1200 (600nm at 15km)
Reporting period	19 seconds (130 km along track)
CCD image region	740 (spectral) x 340 (spatial) pixels

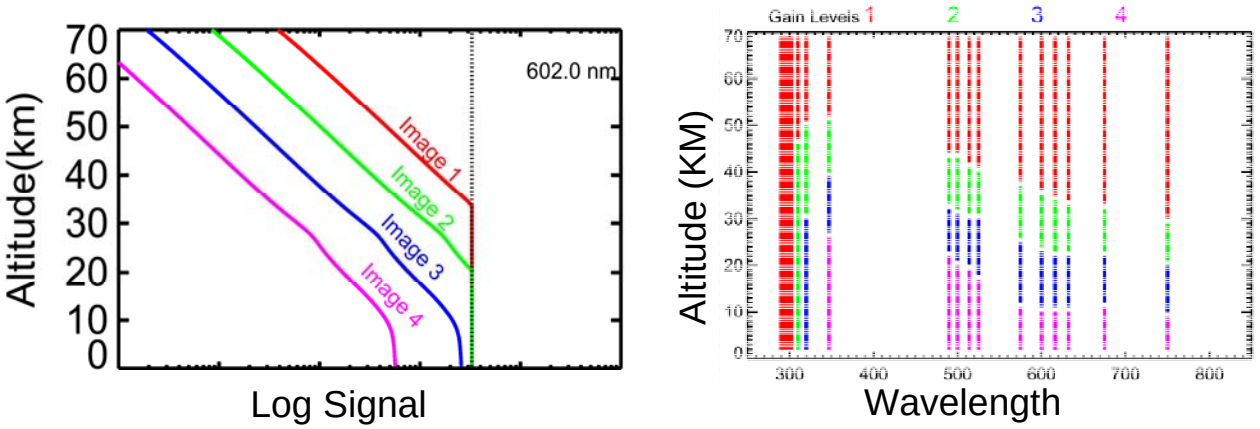

Figure 1-6 Detector response from a simulated 602 nm radiance profile (left) measured in each of the 4 limb images for a single slit. Each image corresponds to a different combination of optical gain and integration time (resulting in 4 "gains"). The dotted line indicates detector saturation. The gain use diagram (right) shows anticipated altitudes for optimum signals in each gain at selected OMPS/LP wavelengths. In order of decreasing gain, the images are 1) high gain – long integration, 2) low gain – long integration, 3) high gain – short integration, and 4) low gain – short integration. (Courtesy of BATC)

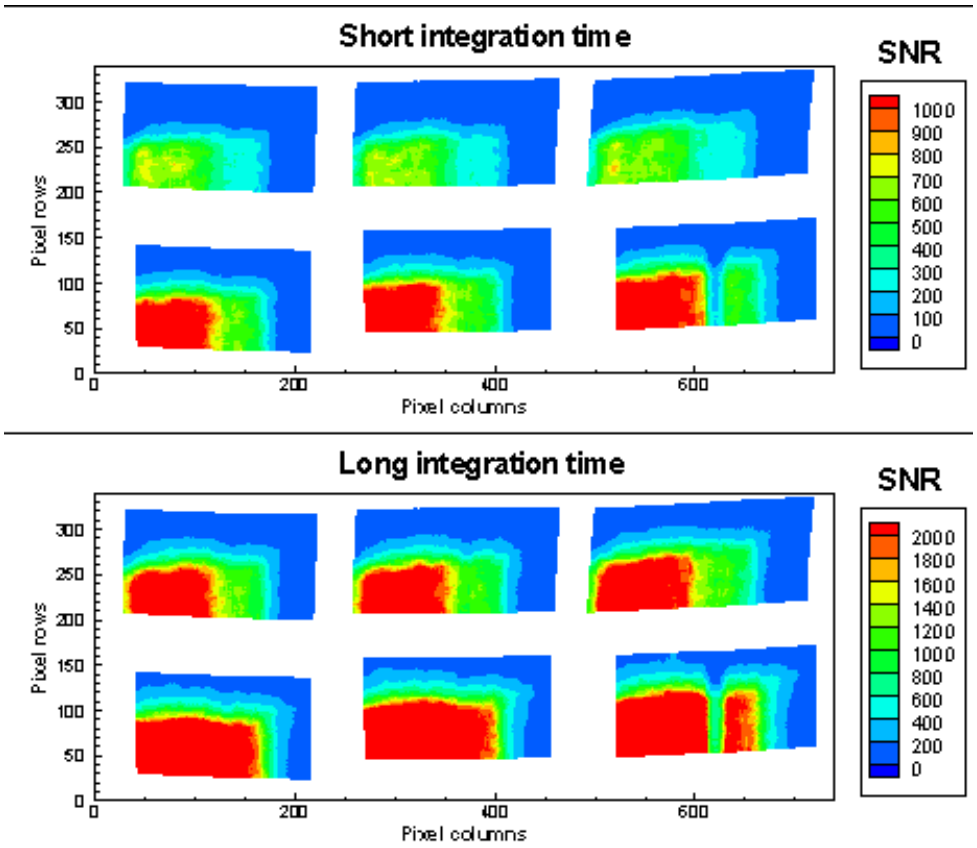

Figure 1-7 OMPS/LP sensor Signal to Noise Ratio at short and long integration times. A sense of the final SNR values comes from interpreting this figure via the information in Figure 1-6.

1.5.2 Stray light mitigation

The OMPS/LP optical design is susceptible to internally scattered light because the full vertical extent of the limb is imaged simultaneously at the focal plane. Radiances vary by approximately 4 orders of magnitude within a view angle range of less than 2°. Furthermore, the radiance spectrum from one slit is physically adjacent on the detector to that of its neighboring slit. The result is NIR photons in close proximity to UV photons. Instrument models suggested that stray light as a percentage of the useful signal could be significant, prompting several design changes intended to minimize stray light or its effects.

The vertical slit height and sensor orientation can have a major effect on stray light fractions. A slit that is too long and extends too far below the horizon collects a large number of photons that are not useful in any retrievals but can scatter to higher altitudes. The slit vertical extent was decreased to the minimum necessary to accommodate mounting tolerances and Earth oblateness effects. Light scattered from the high gain path into the low gain region can also be significant. The TM2 mirrors (see Figure 1-3) were adjusted to maximize the physical separation between the high and low gain images.

A problem that is generic to UV sensors is out-of-band stray light, particularly VIS signals being scattered into the UV portion of a detector. A UV-pass, VIS-blocking filter was deposited on the under side of the detector window, but only in regions corresponding to UV wavelengths. This filter, seen in Figure 1-8, had to be carefully shaped to match the wavelength registration contours of the detector. A separate filter was used for each slit. A feature of the multi-slit design is that nothing prevents photons entering a slit from being dispersed across the entire width of the detector. For instance, 250 nm and shorter wavelength light entering the center slit is actually directed into the portion of the detector reserved for the right slit. The highest UV signals will occur at the IR end of the neighboring image (towards the right in Figure 1-5). To counteract this, the portion of the detector not covered by the UV-pass filter has a coating that rejects UV photons. On the other end of the spectrum, IR photons will bleed into neighboring images (towards the left in Figure 1-5). Since silicon-based CCDs are not sensitive to photons longer than ~1050 nm, these photons are effectively filtered.

The various detector filters are effective at rejecting stray light from neighboring slits. But the signal differential between the NIR and UV portions of the Earth spectrum is so great that a significant number of photons less than 1050 nm are still scattered into the UV side of the neighboring aperture to the left. An unfortunate aspect of the UV-pass filter is that it passes both UV and NIR photons. To mitigate this stray light source, a short-pass filter with a cutoff of ~750 nm was added between the High Gain entrance apertures and the prism. The result is a substantial decrease in UV stray light at the expense of High Gain signals in the range 750 – 1000 nm. Useful NIR signals can still be obtained via the Low gain apertures, which have no additional filter. UV stray light in Low Gain apertures presents little problem since the most useful UV signals come through the High Gain.

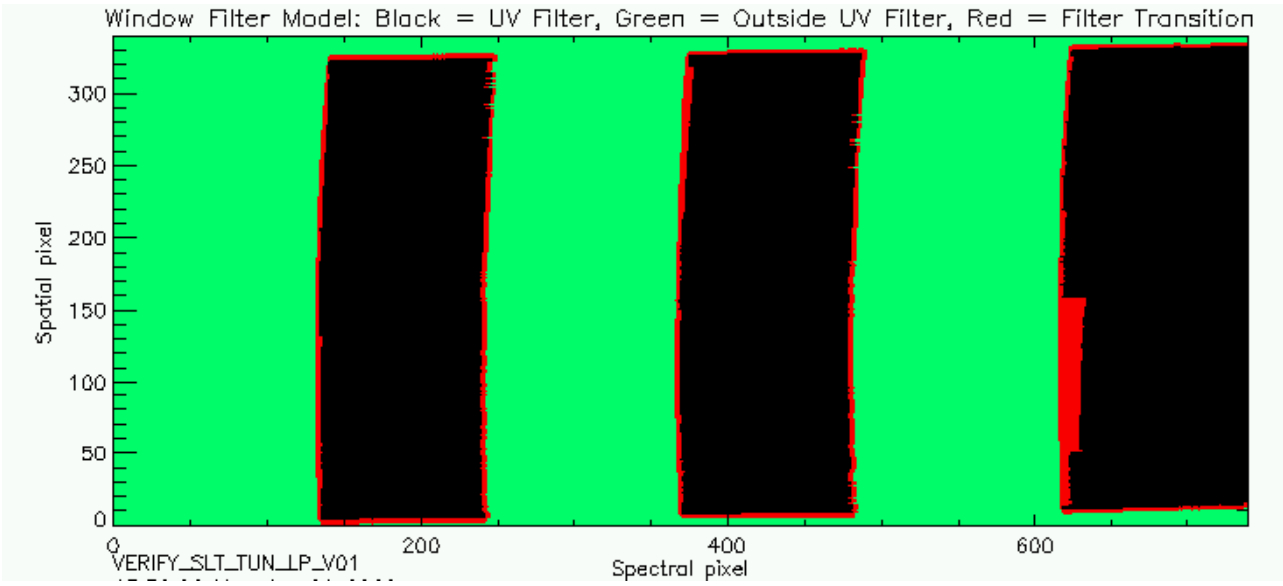

Figure 1-8 A map of the OMPS/LP CCD showing VIS-blocking filter regions (black) and VIS/NIR-pass regions (green). (Courtesy of BATC)

1.5.3 Calibration design

The sensor is designed with several means to monitor and maintain calibration. The solar diffuser mechanism (see Figure 1-2) deploys either of two transmission diffusers in front of the OMPS/LP entrance apertures. Solar measurements are the primary means for monitoring and correcting sensor response changes while in orbit, and for monitoring channel band centers. OMPS has no lamps or independent means to monitor radiometric changes. The Reference diffuser is infrequently deployed, and is used to monitor changes in the Working diffuser. The arrangement of diffusers in relation to the entrance apertures is shown in Figure 1-9. There are actually two Working and two Reference diffusers, one for each aperture size (LG and HG). The two share the micro-lens design, but the HG diffusers include a neutral density filter to equalize high and low gain solar signals.

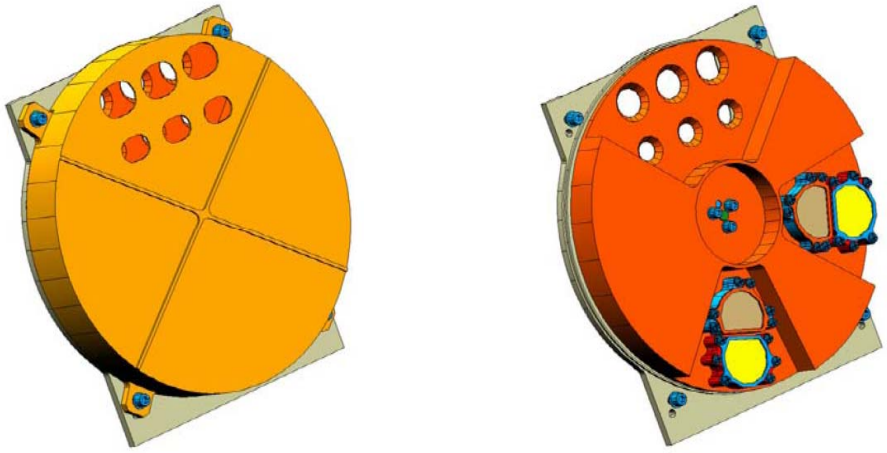

Figure 1-9 The solar diffuser assembly with the 6 entrance apertures in the cover (left), and without the cover (right). The rotating portion in orange contains the 2 Working and 2 Reference transmission diffusers and the 6 inlet baffles. (Courtesy of BATC)

A red light-emitting diode (LED) is positioned directly in front of the focal plane and illuminates all detector image region pixels. This lamp serves the dual purpose of verifying pixel aliveness and monitoring detector linearity. The LED illumination yields a more or less constant rate of photoelectrons which, when sampled at different integration times, covers the full dynamic range of signals encountered in science measurements. Precise knowledge of the integration times and of lamp variations allows for an evaluation of linearity.

1.5.4 In-flight signal processing

A schematic of the OMPS/LP signal flow is shown in Figure 1-10. The signal processing is primarily analog within the sensor and mostly digital within the Main Electronics Box (MEB).

During data acquisition the electron content of all 283,920 pixels is read out and amplified sequentially within the CCD package. This on-chip amplification is the primary source of non-

linearity in the system. The CCD is maintained precisely at a temperature near –45 °C, so dark currents and sources of detector noise are very low, even after radiation damage.

The analog signals pass from sensor to MEB, where they are first converted to digital signals by the 14-bit analog to digital converter (ADC). Next, they pass through a dedicated Field Programmable Gate Array (FPGA) processor designed to quickly apply corrections for non-linearity. This correction is a simple table lookup, where a "correct" digital number replaces each of the 2^{14} possible ADC output values. The flight software (FSW) can be commanded to load updated tables into the linearity FPGA as needed.

Following linearity correction the signals pass into the co-addition FPGA. This dedicated processor collects the signals from each CCD readout in 283,920 separate registers, one for each pixel. Each successive frame (there are currently 10 and 15 frames per image, respectively, for long and short integration times) is added in these registers until the FPGA is told to pass the co-added values to the flight software.

The flight software (FSW) applies the sample table to the pixel data. The sample table contains a code for each pixel that tells the FSW how that pixel is to be handled. Multiple sample tables reside in memory, and any one can be used upon command. Like the linearity correction table, new tables can also be uploaded as needed. The codes in the sample tables indicate whether the pixel should be ignored or placed in the output buffer. Codes also indicate if the pixel should be "binned," i.e. combined with an adjacent pixel. Binned pixels are referred to as macropixels. Binning has the advantage of reducing data rate in cases where individual pixel resolution is not needed. In the current version of the FSW, at most 95,000 pixels or macropixels in a sampled frame can be sent to the output buffer. Use of a sample table is optional. When no sample table is selected, all 283,920 pixels are sent to the output buffer. This is referred to as full frame data.

The output buffer collects data waiting to be read out to the spacecraft through the 1553 data bus. Because the maximum bus rate is only 196 kilobits/second, it is quite easy for OMPS/LP to generate data at a faster rate and fill the buffer. Data acquisition ceases when this occurs. The maximum average data rate over the course of an orbit cannot exceed approximately 6000 pixels or macropixels per second. Since this rate must be shared with the Nadir sensors, the OMPS/LP limit is even lower. Over a nominal 18.7 s report period OMPS/LP cannot sample more than ~91,500 pixels, to be shared between long and short integration times.

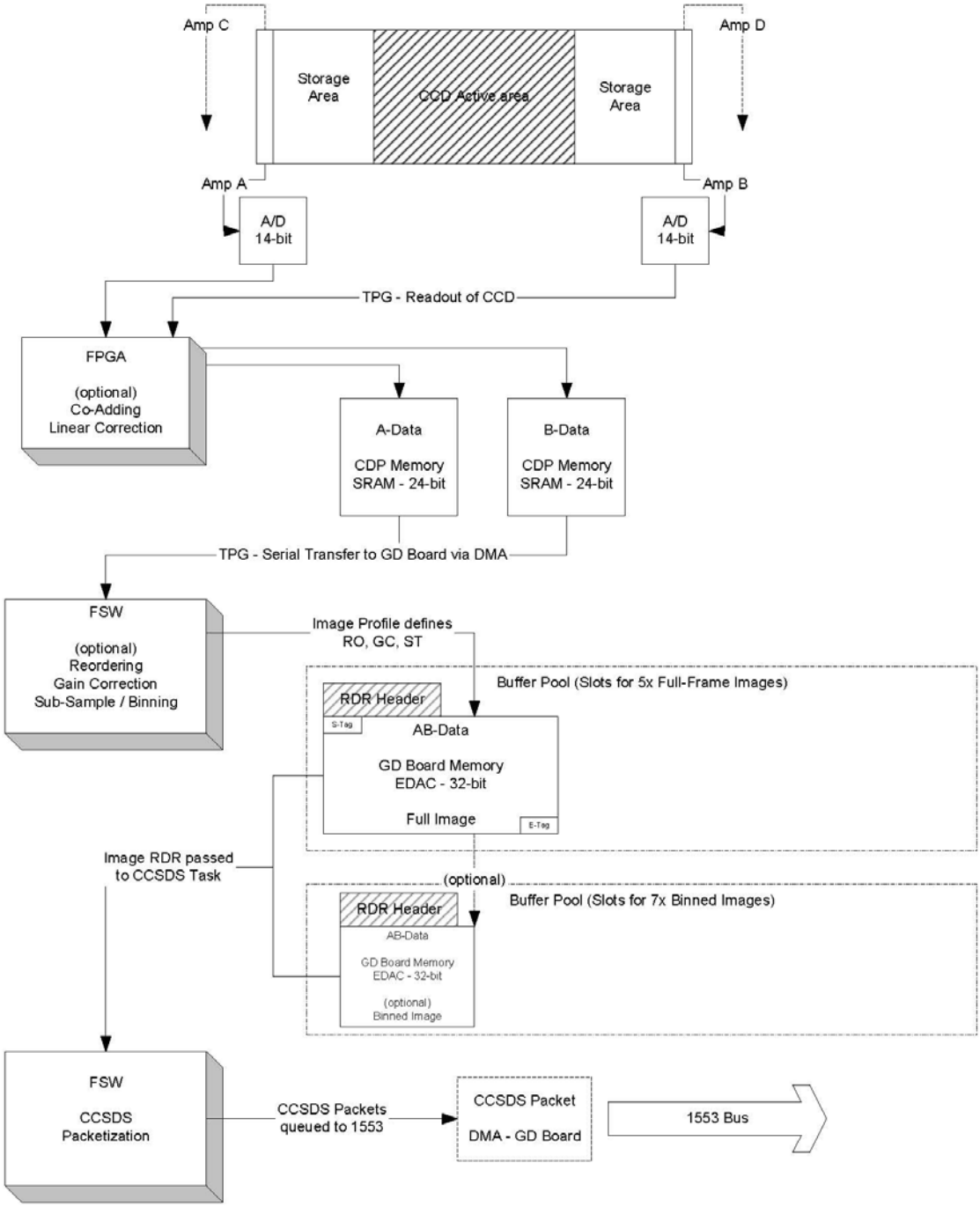

Figure 1-10 OMPS data flow, beginning at the CCD serial registers and ending at the OMPS/spacecraft 1553 interface. The split frame architecture of the CCD is maintained until signals are combined in the flight software. (courtesy of BATC)

1.6 Concept of Operations

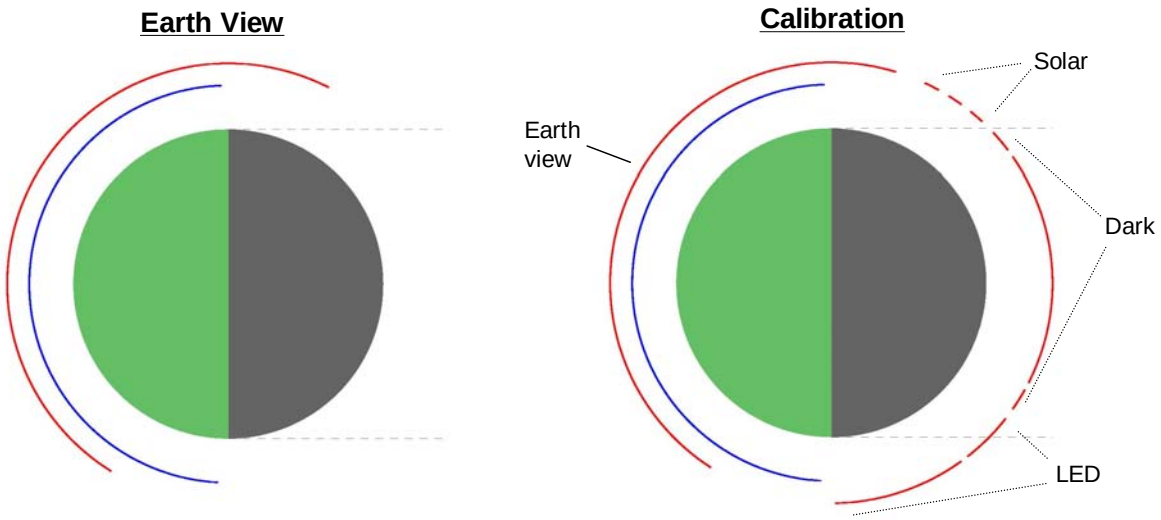

Figure 1-11 Two basic orbit types of OMPS/LP, Earth-view and Calibration. In these figures the sun illuminates the globe from the left, and the spacecraft moves clockwise. The LP sensor looks backward along the ground track. Red lines indicate satellite positions where LP data are collected, and blue lines indicate Nadir data collection.

Whereas the OMPS/LP sensor design is loosely based on the predecessor SOLSE and LORE limb sensors, its operations concept is most like that of the Total Ozone and Mapping Spectrometer (TOMS). Earth-view data is obtained during dayside portions of the orbit in a constant and consistent data acquisition sequence. Calibration data is independently obtained on the night-side or at the day-night boundary. The calibration data is downlinked to Earth in distinct data packets and subsequently processed separately from Earth-view data. The different classes of data packets are tagged with an Application Packet Identification (APID), as illustrated in Table 1-3.

Table 1-3 OMPS/LP Application Packet Identifications (APIDs)

Application Packet Identification (APID)	Data packet class
563	Earth-view: nominal
566	Calibration: nominal
579	Earth-view: diagnostic
582	Calibration: diagnostic

Data that is packetized by the flight software (FSW) can be labeled Nominal or Diagnostic. Nothing differentiates data as either one or the other besides the assignment of the APID. The purpose of this classification is to ease data management in the ground processing system. In general, data is assigned a nominal APID only if it will pass through the full ground processing system. During early sensor checkout operations much of the data are labeled Diagnostic to facilitate their segregation from data taken under more typical conditions. The remainder of the discussion will concentrate on nominal measurements.

During nominal Earth-view operations, all three sensors are imaging and sending data to the MEB, which necessitates a careful coordination of the individual integrations for all three sensors so as to prevent buffer pool overflow and the subsequent loss of data. In Earth-view the nadir and limb sensor measurements typically cover the same range of solar zenith angles (up to 88 deg.), but begin their respective imaging sequences at different points along the orbit. The reporting periods are also different. Since the LP views the limb in the anti-velocity direction, it begins imaging about 7 minutes after the TC and NP sensors (see left diagram in Figure 1-11). The reporting periods, which must accommodate the science objectives of each sensor, are respectively: 18.7 sec. for the LP, 7.6 sec. for the TC and 37.4 sec. for the NP. At times, the LP will be interrupted to allow for calibration activities on the nadir sensors.

Because the timing of the 3 OMPS sensor measurements must be carefully coordinated, changing integration times or the report period (total time of co-added frames) of any is not a simple undertaking. The Earth-view timing pattern, once chosen, remains fixed for most of the mission. Pixel sampling is an optimization involving science requirements, calibration and monitoring needs, pixel performance, Earth scene variability, sensor pointing variations within an orbit, and the gain characteristics as shown in Figure 1-6. Sampling can be changed at any point in the orbit, but it results in a data gap. For this reason pixel sampling is expected to be fixed for a considerable period of time, though it can be changed frequently should the need arise. The size of the sample table size is reduced by eliminating CCD pixels that are either always saturated (such as pixels corresponding to high gain and long integration times at low altitudes and in the visible), or alternatively have a low signal (such as pixels corresponding to low gain and low integration times at high latitudes and in the visible).

Because OMPS/LP Earth measurements occur only over the sunlit portion of the globe, the data are naturally divided into orbits and it is possible to talk of orbit types. The most frequently occurring orbit type, shown on the left in Figure 1-11, is the nominal Earth-view orbit. The calibration orbit, shown on the right in Figure 1-11, is nominally scheduled every week. Other orbit types, which occur daily and monthly, are minor variations of the calibration orbit shown.

1.6.1 Solar measurements

The primary OMPS/LP calibrations are solar measurements, which are nominally scheduled weekly and occur just before the spacecraft enters Earth eclipse near the north pole. The two Working (or Reference) diffusers are rotated in front of one pair of apertures (left, center, or right) and measurements taken through 3° of elevation. The diffusers are moved to the next aperture pair and measurements are repeated, then again with the final pair.

Unlike the Earth limb radiances, solar signals are nearly equivalent across the spatial dimension and between high and low gain apertures. Only one integration time is used, and the data are co-added to create 5 separate images for each of the 3 diffuser positions. All pixels within an aperture are sampled, approximately 50,000 pixels. No binning of image region pixels takes place. This results in an unsustainable data rate, but the idle period following solar measurements allows the buffer pool to drain.

1.6.2 Dark current measurements

Dark measurements are needed to provide a per pixel estimate of the detector current in the absence of photons. It is important to duplicate the environmental factors that affect the dark currents. The detector temperature is maintained throughout the orbit, thus keeping thermal electron currents constant. Measurements are scheduled to avoid the South Atlantic Anomaly to minimize particle hits. It is not possible to eliminate these hits, but the measurement sequence is designed to make their detection straightforward. The primary long exposure measurement is bracketed by two shorter exposures. Any disagreement between the measured currents results in elimination of that pixel's measurement.

1.6.3 LED measurements

The LED measurements are primarily designed to monitor response linearity, though they can also be used to check pixel aliveness. After a 5 minute lamp warmup the, CCD is taken through a series of 83 images with varying integration times. Integration times are varied from 0 to 2.4 seconds in order to cover the full dynamic range of the sensor. There are 41 integrations with times incrementing in steps of 60 ms, interleaved with 42 0.5 sec integration measurements. The purpose of these reference measurements is to monitor and help correct for any lamp changes.

1.7 Pre-launch sensor characterization

The OMPS/LP sensor has been subjected to a series of calibration and characterization measurements in the laboratory. Characterizations were performed for spectral and spatial relative response, radiometric response, linearity, polarization sensitivity, and stray light sensitivity. The basic measurements are described in subsections below.

Following analysis of the characterization measurements by the sensor vendor, Ball Aerospace and Technology Corporation (BATC), a set of calibration databases were prepared for OMPS/LP. These databases, which have a nearly one-to-one correspondence with the key sensor tests, contain the sensor characteristics needed by the SDR algorithm. This set is composed of the 10 datafiles, which are listed in Table 1-4.

Table 1-4 OMPS/LP sensor calibration databases

Datasbase	Database definition

mnemonic	
CBC	Band center wavelength of each pixel
SRG	Unit vectors describing each pixel's line of sight toward the limb
BPS	Spectral response function of each pixel
FOV	Spatial (vertical) response function of each pixel
RAD	Radiance calibration coefficient of each pixel
IRD	Irradiance calibration coefficient of each pixel
GON	Irradiance goniometric response
SLT	Point Spread Functions and ghosts (straylight)
LED	Non-linearity correction table (as loaded into the sensor)

1.7.1 Channel Band Centers (CBC)

Channel band centers record the maximum of each pixel's spectral response function. The values are not needed by the SDR algorithm except as a first guess for the post-launch wavelength calibration algorithm. The channel band centers are included in the SDR output products as a matter of convenience to subsequent retrieval algorithms.

The pre-launch pixel wavelength registration was measured by BATC using a combination of a tunable laser and a monochromator source illuminating an integrating sphere at 26 separate wavelengths. For each of the 26 nominal wavelengths the spectral position (in pixel number) of the peak response was found. A polynomial fit to these positions for each spectral line reduced the noise in the peak positions. The dispersion relation for each spatial location was determined by fitting

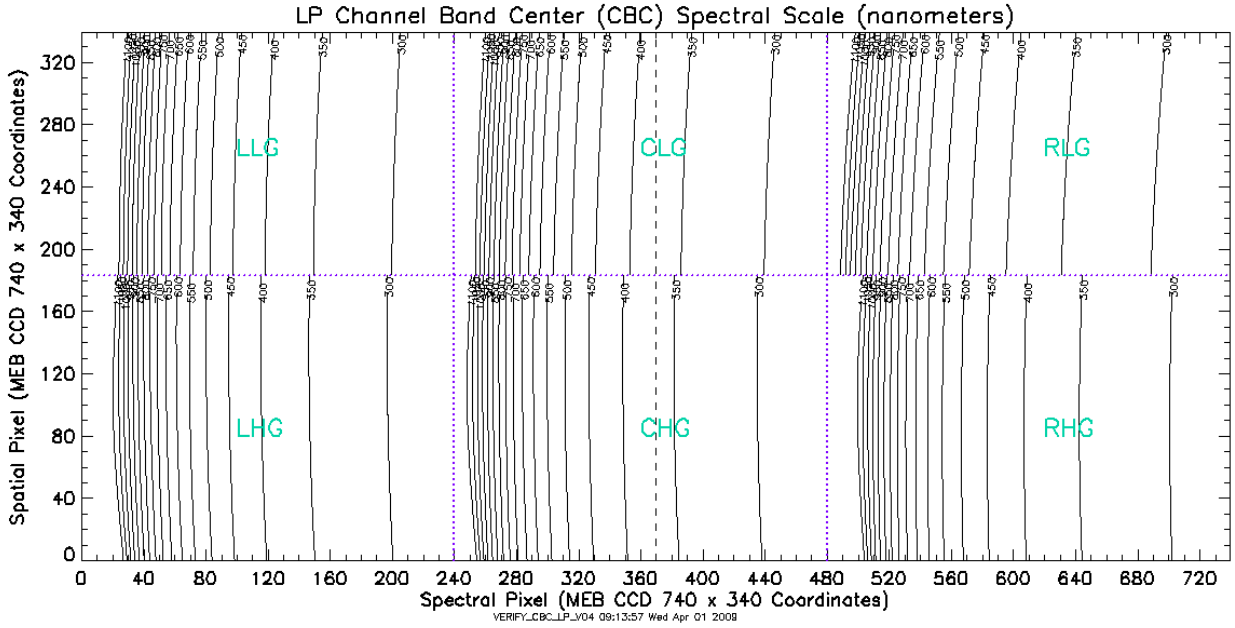

Figure 1-12 Iso-spectral contours representing the OMPS/LP spectral registration are shown in each of the 6 aperture regions. (courtesy of BATC)

a 7^{th} order polynomial with spectral pixel index as the independent variable and λ^{-2} of the source as the dependent variable. The resulting relationship between pixel index (CCD row number) and wavelength in each CCD column forms the basis of the OMPS/LP spectral registration.

The delivered database contains band centers for all pixels in the CCD image region as well as polynomial coefficients describing the relationship between CCD row number and band center wavelengths.

Database uncertainty
The delivered band center characterizations met the uncertainty goal of 0.01 FWHM in the UV and 0.03 FWHM in the VIS and NIR. This goal, which was established for post-launch wavelength registration, is tighter than necessary for pre-launch characterizations. These band centers are used as inputs to radiometric calibration, stray light characterizations, and other analyses where pixel band center knowledge is needed. Post-launch band centers are expected to differ significantly compared to pre-launch characterizations due to changes in the thermal environment, so the delivered values cannot be used after launch. Section 5.1 contains a discussion of post-launch pixel wavelength registration.

1.7.2 Spatial registration (SRG)

The spatial registration of a pixel is the angle at which a photon enters the sensor telescope and results in a maximum response in that pixel. It is sometimes referred to as pixel pointing because each vector is projected out the front of the sensor and toward the Earth during the geolocation process. When combined with spacecraft attitude and ephemeris information, spatial registration provides the input necessary to locate the tangent point for each pixel's field of view.

To measure the pre-launch spatial registration BATC used highly collimated broad band and spectral line sources to illuminate the sensor entrance aperture via a slit plate. The sensor was first rotated horizontally (azimuth) to find the angle of peak response. Once positioned at the optimum azimuth the sensor is rotated vertically over 2° in steps of 0.1°. Each of these 21 pixel responses is fit to find the spatial pixel (column number) of maximum response. This is repeated for all wavelengths across each aperture. A surface fit is applied to the grid of response maxima (21 spatial indices for every spectral index within an aperture) with the known elevation angle as the dependent variable, resulting in the vertical pointing vector of each pixel.

The delivered database contains the look vectors (azimuth and elevation angles) for all pixels in the CCD image region. The characterized angles have been rotated to the spacecraft coordinate system using the measured mounting angles of the sensor.

Database uncertainty
Pixel pointing knowledge is the primary source of uncertainty for FOV tangent height. Uncertainty in the absolute pointing knowledge is driven by factors external to this database, such as sensor

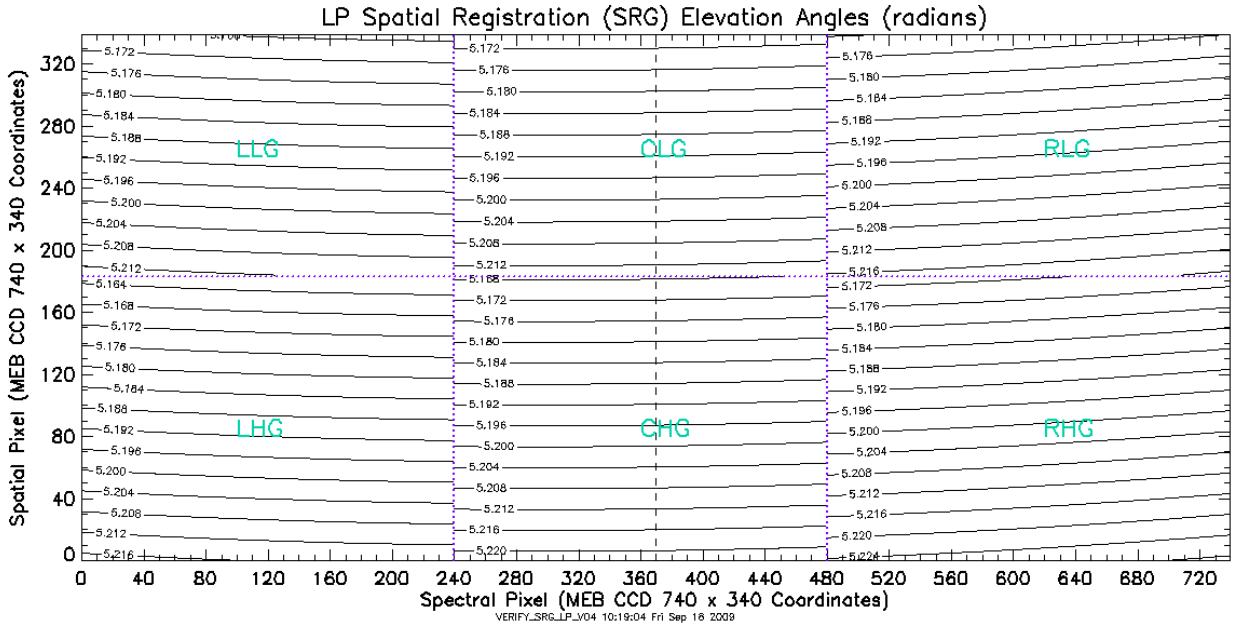

Figure 1-13 Iso-elevation contours representing the OMPS/LP vertical registration are shown in each of the 6 aperture regions. (courtesy of BATC)

mounting errors and on-orbit variations. The database itself easily meets the performance objective of 0.5 arcmin. (1σ). The pixel relative pointing uncertainty is less than 0.1 arcmin. RMS.

In addition to precise knowledge of the pixel pointing, the elevation angle alignment of the optics and detector must fall within ±6 arcmin. in order to provide adequate tolerance for sensor mounting errors, orbit altitude changes, and other sources of variation. This specification was met for all but the left low gain aperture (LLG), whose central boresight points high by less than 3 arcmin. (~ 3km at the tangent point).

1.7.3 Band pass (BPS)

The pixel band pass function, sometimes referred to as its spectral or slit function, is the relative response of a pixel to illumination at different wavelengths. This function is derived over ±5 pixels, or approximately 5 times the FWHM of the response. All response outside that range is considered stray light. Like the channel band centers, the band pass functions are not used by the SDR algorithm except when performing wavelength registration. These functions are not provided in any SDR output product.

The measurement of these functions proceeded in a similar manner to the channel band center measurement except that instead of discrete wavelengths, the laser and monochromator were tuned over a wavelength range of ±2 pixels for each of the 24 band centers. Since the wavelength step size is coarse, approximately 0.4 pixels, 5 adjacent pixel responses are interpolated to a fine grid and combined to form a single observed band pass function. The result is a function reported in 241 intervals.

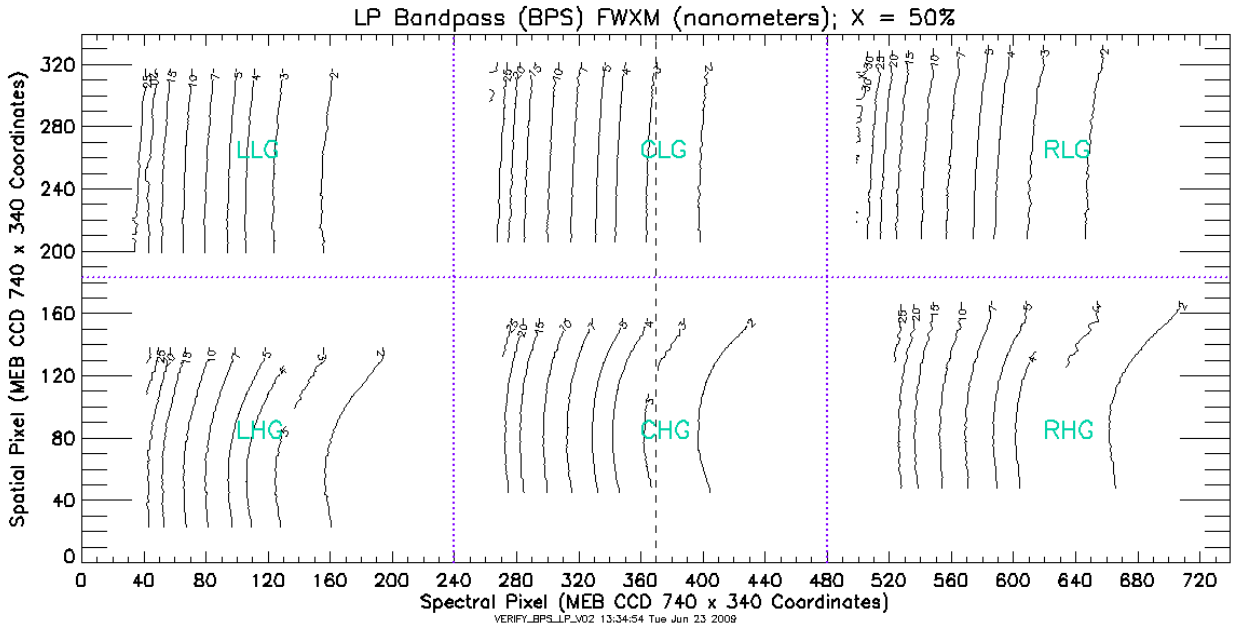

Figure 1-14 The Full Width at Half Maximum of the OMPS/LP band pass functions are shown in each aperture as iso-width contours. (courtesy of BATC)

The delivered database contains the relative spectral response values for each pixel in the CCD image region. This response is reported two ways. Firstly, each of 241 response values (spaced uniformly in steps of 0.02 pixels) is 2-D interpolated over each aperture. Secondly, each measured response is decomposed into orthogonal functions using at most 5 basis vectors. Data from multiple spatial positions (at most 30) are combined in each fit to reduce uncertainties. The resulting coefficients for these basis vectors are interpolated or extrapolated over all pixels in each aperture.

Database uncertainty

There are several sources of uncertainty in the delivered bandpass datasets. These fall into the broad categories of measurement errors and characterization errors. An estimation of measurement errors is shown in the lower portions of each image in Figure 1-15. These curves show the standard deviations of the measurements comprising a single composite bandpass, and are in normalized units. They suggest 1σ variations of the measurements of approximately 1%, which are assumed to be random. Systematic uncertainties were not estimated. Additive errors such as test setup stray light were likely large contributors.

Two characterization approaches were used for the delivered bandpasses, the interpolation method and the regression method. For interpolations, uncertainties were estimated by removing one of the

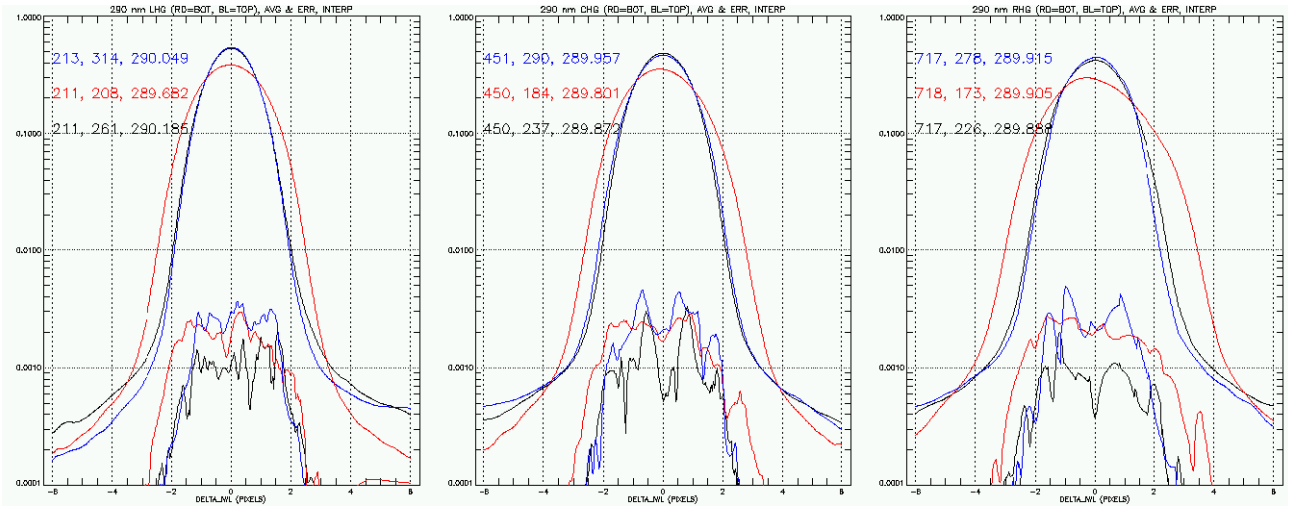

Figure 1-15 Averaged bandpass responses for high gain apertures as a function of the distance (in pixels) from the band center illumination. Measurements from each of 5 pixels are independently interpolated to a common grid, then averaged. Results are shown for near the top (blue), center (black), and near the bottom (red). Corresponding lines at the bottom of each image are the standard deviations of the 5-pixel ensembles. (courtesy of BATC)

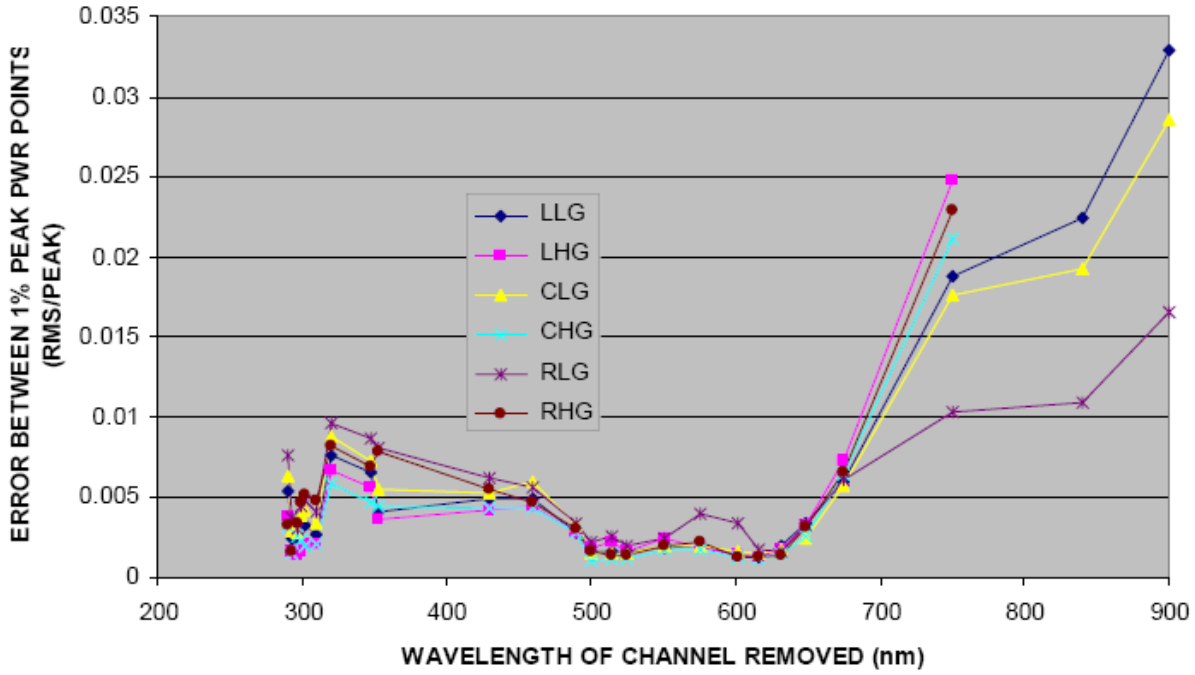

Figure 1-16 The bandpass interpolation error estimated by removing individual bandpass measurement sets in the interpolation grid. The plotted points are the RMS deviations between measured and predicted values. (courtesy of BATC)

measurements from the interpolation grid, then comparing the removed measurement with the predicted values. When this is repeated for every point in each bandpass (only those points with > 1% response) and all spatial positions, a large set of differences is accumulated for each wavelength and within each aperture. The RMS difference is plotted in Figure 1-16. For the regressions, the number of spatial locations over which each fit is used was reduced until the RMS deviation between measured and fit values was approximately 0.25%.

1.7.4 Pixel field of view function (FOV)

The instantaneous field of view function (IFOV) is the relative response of a pixel to illumination at different vertical (elevation) angles. The IFOV functions are not used at all by the SDR. These functions are not provided in any SDR product outputs.

The pixel IFOV functions are derived from the same test as the pixel pointing measurements (see Section 1.7.2). Five elevations were chosen within the 1.85° slit height. At each position the narrow horizontal slit was rotated over a range of 0.102° in steps of 0.003°. This scan effectively mapped out the vertical (elevation angle) response of each pixel. The initial horizontal scan also provided a coarse measure of the horizontal IFOV (azimuth angle), which is approximately 0.03° FWHM. Less care was taken with these measurements since ozone retrievals are rather insensitive to horizontal response variations. In a manner similar to that used to construct the bandpass functions, measurements from 7 spatially adjacent pixels were averaged to produce a single IFOV measurement set. Each set consists of 121 response points.

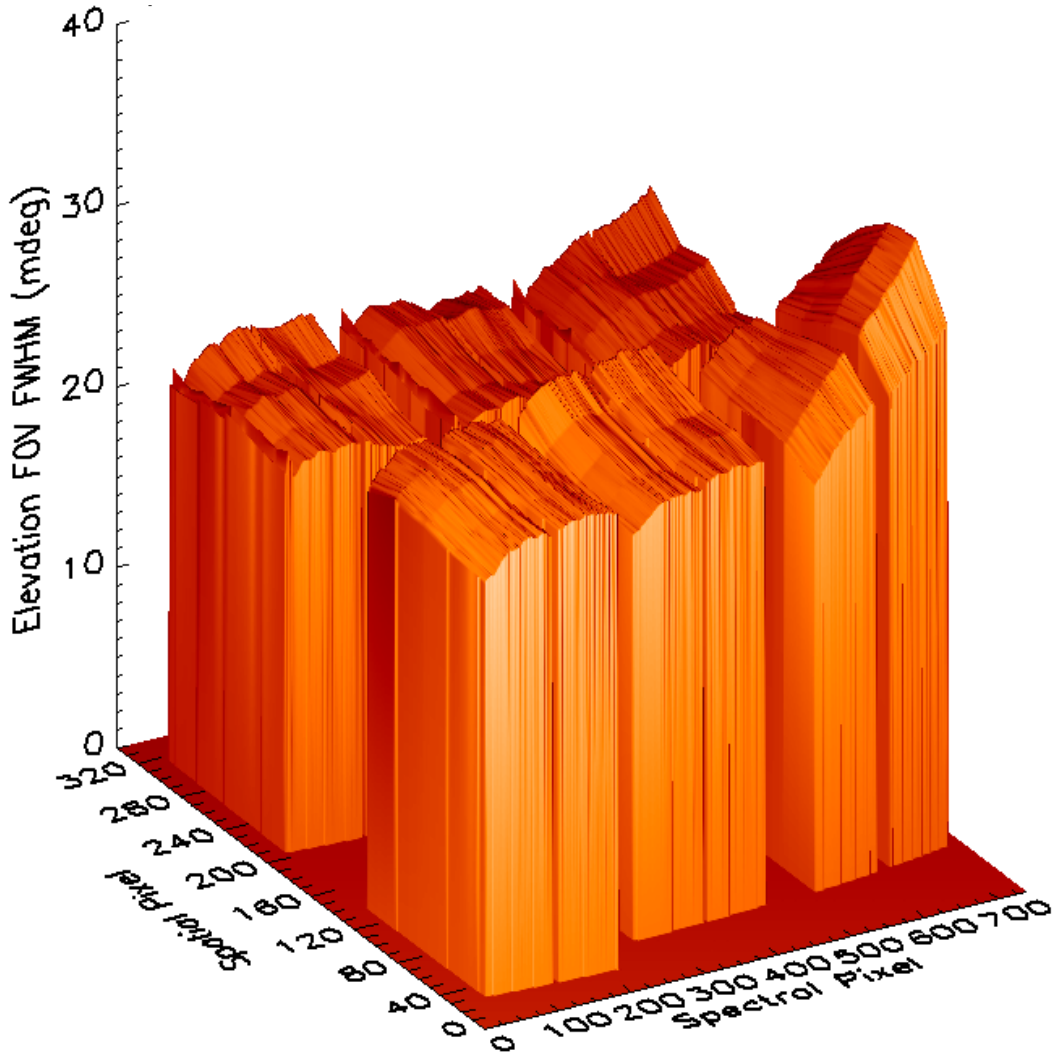

Figure 1-17 The Full Width at Half Maximum of the derived spatial response functions, reported for each pixel. At the tangent point 0.02° extends approximately1.15 km. (courtesy of BATC)

The delivered database contains the relative vertical response values for each pixel in the CCD image region. This response is reported two ways. Firstly, each of 121 response values (spaced uniformly in steps of 0.02 pixels) is 2-D interpolated over each aperture. Secondly, each measured response is decomposed into orthogonal functions using 5 basis vectors. The coefficients for each of these basis vectors are interpolated over all pixels in each aperture.

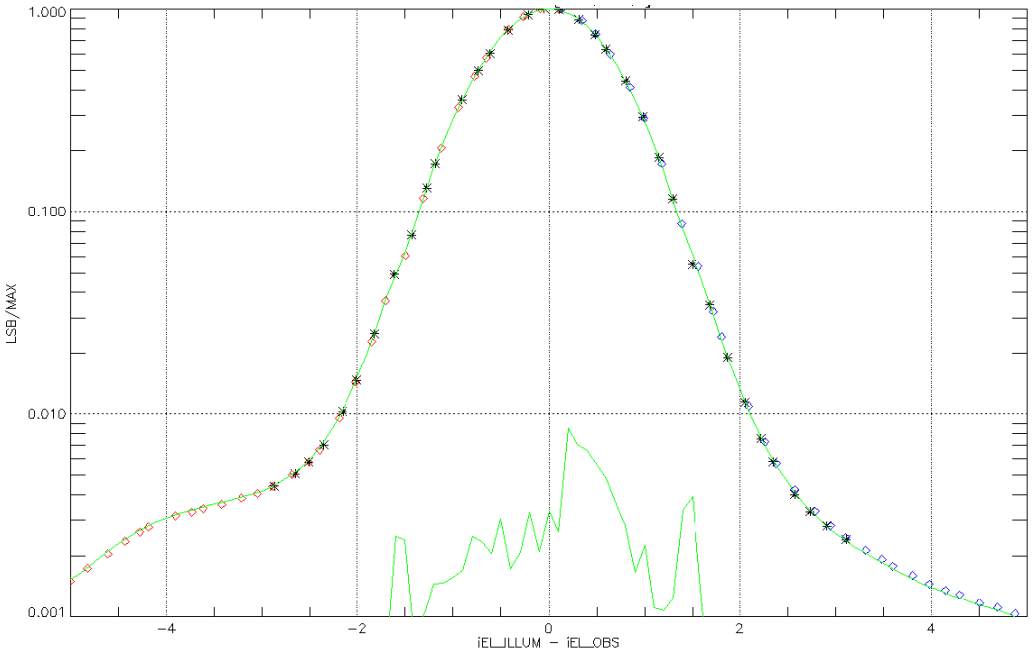

Figure 1-18 Averaged pixel IFOV response as a function of the distance (in pixels) from the center of illumination. Measurements from each of 7 pixels are independently interpolated to a common grid, then averaged. Average results are indicated by the solid line. Individual points are measured responses for pixels 1, 4, and 7 (not re-gridded). The green trace at the bottom is the standard deviation of the 7 measurements after re-gridding. (courtesy of BATC)

Database uncertainty

An estimation of the pixel IFOV measurement errors is shown in the lower portion of Figure 1-18. This curve shows the standard deviations of the measurements comprising a single composite IFOV, and are in normalized units. It suggests 1σ variations of the measurements of approximately 0.3%, which are assumed to be random. Some of the systematic uncertainties were estimated by comparing results obtained through different source slits. Interpolated pixel IFOV sets obtained from 3 separate slits, only one of which is used for the delivered data set, were compared and the RMS difference computed. These differences, computed for each aperture and normalized to the peak, are reported in Table 1-5. This estimation method ignores common systematic errors such as test setup stray light. A comparison between pixel IFOVs and point spread functions from the stray light test suggests additive errors in the IFOVs of as much as 0.2%.

For the regressions, the number of spatial locations over which each fit is used was reduced until the RMS deviation between measured and fit values was approximately 1%.

Table 1-5 Pixel IFOV parameterization uncertainties

Aperture	RMS difference of fit (fraction of peak response)
Left High Gain (LHG)	0.0109

Center High Gain (CHG)	0.0141
Right High Gain (RHG)	0.0172
Left Low Gain (LLG)	0.0061
Center Low Gain (CLG)	0.0042
Right Low Gain (RLG)	0.0066

1.7.5 Radiance calibrations (RAD)

The radiance calibration coefficients describe the amount of incident radiant energy that results in one digital count in each pixel. This number is the inverse of the instrument sensitivity for a given pixel. The values are used by the SDR algorithm to convert ideal Earth-view signals (signals corrected for detector and electronic processing effects) into units of radiance. The delivered values are not used directly, but are modified to account for estimated sensor degradation. This exact approach is discussed more completely in Section 4.1.

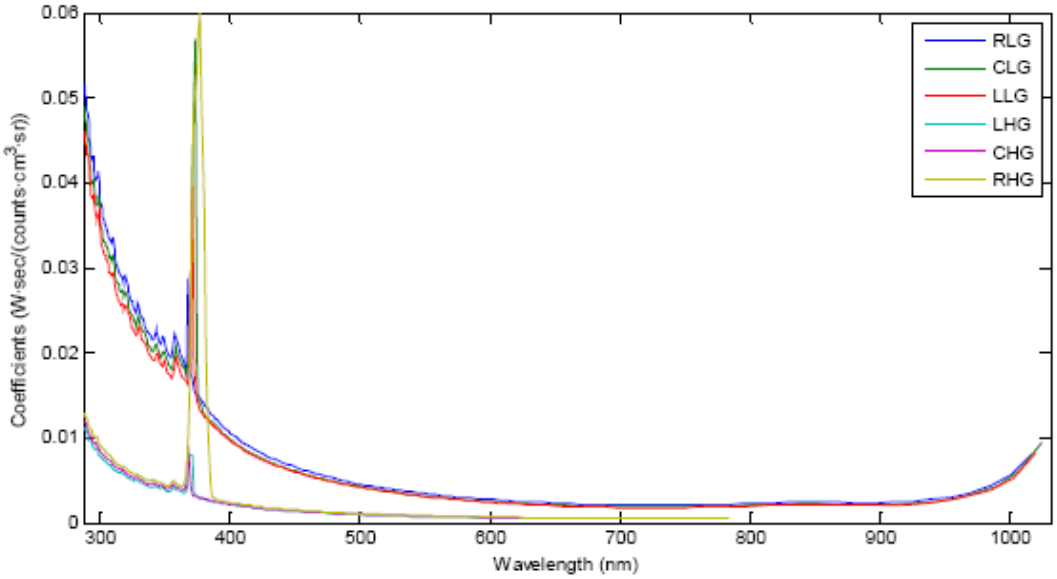

Figure 1-19 Radiance calibration coefficients averaged in the spatial dimension over each aperture. The coefficients are the inverse of sensitivity. (courtesy of BATC)

A NIST calibrated FEL lamp was used to illuminate a Spectralon™ diffuser. Since the reflective properties of the diffuser are known, it became a calibrated radiance source. The sensor was rotated to illuminate in turn each of the 6 limb apertures. During any given measurement the remaining 5 apertures were masked to eliminate inter-aperture scattered light.

The delivered database contains the radiance calibration coefficients for every pixel between 280 and 1100 nm and within the vertical extent of each aperture. These coefficients have the units Watt·sec·centimeter^{-3}·steradian^{-1}· count^{-1}. Values are provided both with and without a correction

for stray light present during the test. Stray light corrections used the characterizations described in Section 1.7.8.

Database uncertainty

The primary sources of uncertainty in radiance calibration are knowledge of the test source radiance and systematic differences between the test setup and the in-flight measurement configuration. Even in the best calibrated sensors radiometric errors of 2% are expected. Since this magnitude of error is unacceptable for many atmospheric retrievals, the algorithms are designed to take advantage of correlated errors in the calibration. Pairing of measurements in limb retrieval algorithms, both spatially and spectrally, is a common feature designed to minimize sensitivity to calibration errors. Many of the radiometric calibration error sources are systematic and are equal for all pixels. Retrievals based on the ratio of measurements are less sensitive to these common errors.

It is therefore important to report not only absolute radiometric uncertainties, but also inter-pixel uncertainties. These latter uncertainties are further divided into those for pixels with approximately the same pointing but differing band center wavelengths, and those with nearly the same wavelengths but differing pointing. The estimates listed in Table 1-6 are based primarily on the calibration error budget for OMPS/LP, but also with verification from the pre-launch tests. It is worth noting that sensor stray light corrections for UV radiance calibrations are 5-10%, with as much as a 13% correction at 290 nm. VIS and NIR corrections are below 1%. The associated uncertainties have been included in the table values.

Table 1-6 Radiance uncertainties (1σ)

	290 – 360 nm	380 – 1000 nm
Radiance: absolute	2.4%	2.3%
Radiance: wavelength-dependent	1.0%	0.5%
Radiance: spatially-dependent	0.3%	0.3%
Albedo: absolute	2.0%	1.7%
Albedo: wavelength-dependent	0.5%	0.4%
Albedo: spatially-dependent	0.1%	0.1%

Albedo calibration

In addition to spectral and spatial pairing, normalization of Earth radiance measurements by solar irradiance measurements is often used to cancel correlated pre-launch calibration errors. The OMPS/LP radiometric calibrations were designed so that radiance and irradiance calibrations shared many error sources. The ratio of radiance and irradiance calibration coefficients, referred to here as the albedo calibration, has generally smaller uncertainties than either radiance or irradiance calibrations alone (see entries in Table 1-6). One option for further reducing retrieval errors caused by calibration is to use normalized radiances, i.e. divide each pixel's radiance value by the measured solar irradiance at that pixel.

The albedo calibration of OMPS, shown in Figure 1-20, is closely related to the diffuser transmittance. The Low Gain portion of the diffusers was designed to be more transmissive than the High Gain portion to counteract the difference in aperture sizes.

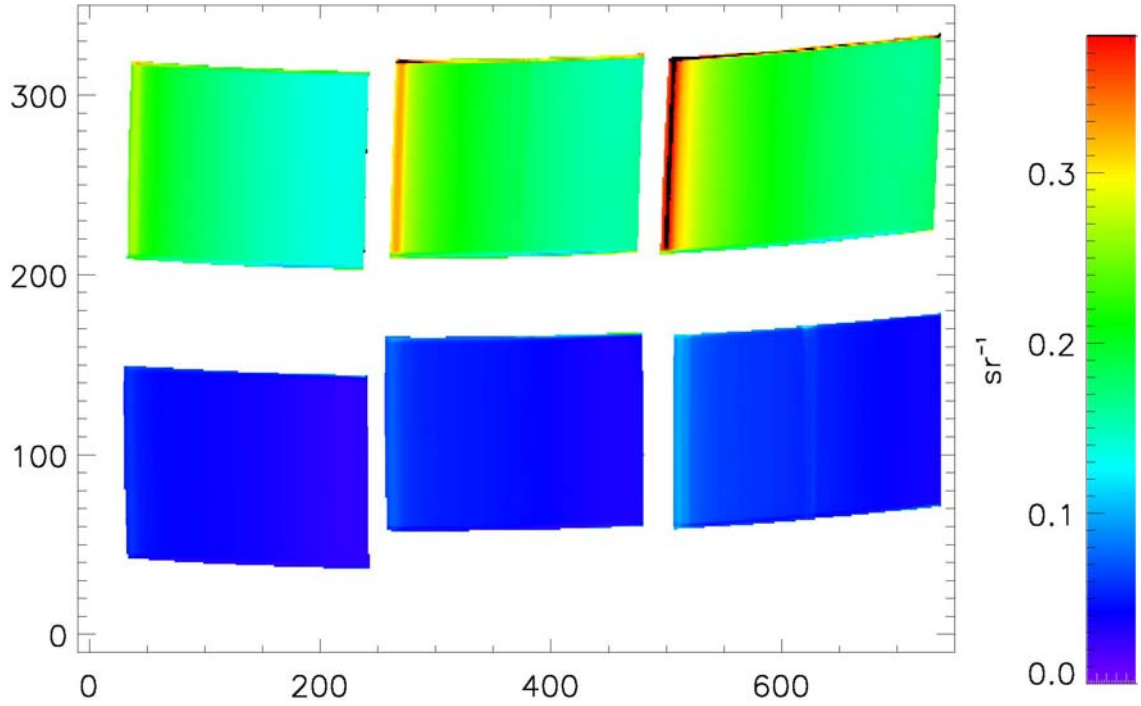

Figure 1-20 The OMPS/LP albedo calibrations (radiance coefficients divided by irradiance coefficients) are displayed for all pixels in the optics regions of the detector. These values are directly proportional to diffuser transmittance.

1.7.6 Irradiance calibrations (IRD)

The irradiance calibration coefficients describe the amount of solar energy flux that results in one digital count in a pixel. These values are used by the SDR algorithm to convert ideal solar signals (signals corrected for detector and electronic processing effects and for observation angle) into units of irradiance. This number is similar to the pixel's radiance coefficient except that it includes the reflective properties of the flight diffusers. If the Bi-directional Scattering Distribution Function (BSDF) of the diffuser and surrounding assembly were accurately known, radiance coefficients could be calculated from the product of the irradiance coefficients and the BSDF. As it is, the BSDF is derived (rather than measured) from the ratio of radiance and irradiance calibration coefficients, and is also referred to as the albedo calibration.

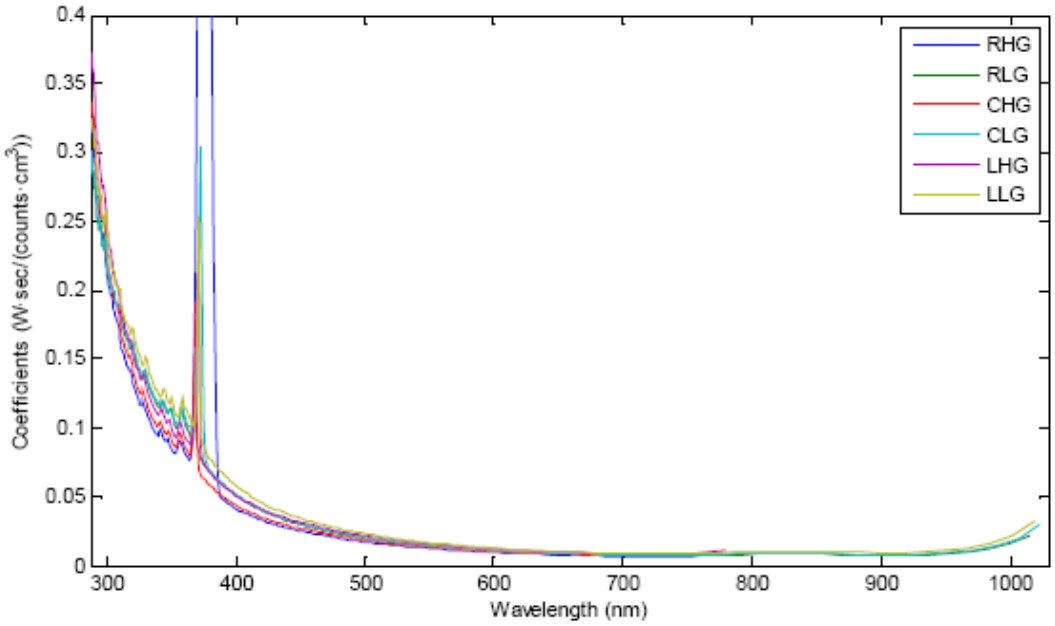

Figure 1-21 Irradiance calibration coefficients averaged in the spatial dimension over each aperture. The coefficients are the inverse of sensitivity. (courtesy of BATC)

A NIST calibrated FEL lamp directly illuminated the OMPS/LP flight diffusers. The sensor was rotated to illuminate in turn each of the 6 limb apertures. During any given measurement the remaining 5 apertures were masked to eliminate inter-aperture scattered light.

The delivered database contains the irradiance calibration coefficients for every pixel between 280 and 1100 nm and within the vertical extent of each aperture. These coefficients have the units Watt·sec·centimeter^{-3}· count^{-1}, and represent the sensitivity to irradiance incident at elevation -22.2° and azimuth 21.75°. There is a separate set of coefficients for the Working and Reference diffuser, and values are provided both with and without a correction for stray light present during the test. Stray light corrections used the characterizations described in Section 1.7.8.

Database uncertainty

Similar to the radiance calibration, irradiance calibration errors arise primarily from errors in the test source irradiance and incomplete representation by the test setup of in-flight conditions. The test diffuser, whose reflective properties are a major source of uncertainty in radiance calibrations, is not used for irradiance calibrations. However, illumination non-uniformity, lower signal levels, and stray light are among numerous factors that increase the irradiance calibration uncertainty. Like radiance calibrations, it is informative to break out uncertainties into spectrally and spatially dependent components, where many correlated errors cancel.

Table 1-7 Irradiance uncertainties (1σ)

	290 – 360 nm	380 – 1000 nm
Irradiance: absolute	2.6%	2.3%

Irradiance: wavelength-dependent	2.0%	0.5%
Irradiance: spatially-dependent	0.3%	0.3%

1.7.7 Goniometric calibrations (GON)

The irradiance sensitivity of OMPS/LP depends on the irradiance angle of incidence, primarily because the diffusers are not Lambertian. The goniometric correction factors account for this variation and allow a single set of irradiance calibration constants to be used when converting solar signals to solar irradiance. The appropriate set of factors for a given solar measurement is based on the spacecraft-centered solar angles at the time of the measurement. The solar signals are multiplied by these factors prior to conversion to irradiance units.

To determine the goniometry factors the sensor response was measured as it rotated across a 7x7 azimuth and elevation grid. The grid spacing was 3.25° in azimuth and 2° in elevation. The range of angles covers the anticipated extremes during a full year of solar measurements. A collimated Xenon source was used as a source during the measurements. One of the 49 angle pairs, called the reference angle, corresponds to the angle at which the irradiance calibration coefficients were derived. All remaining 48 response sets were normalized pixel by pixel to the responses at the reference angle. An example of the 4-dimensional measured response (spectral, spatial, azimuth, elevation) is shown in Figure 1-22 for one of the apertures.

The delivered database contains two 7x7 grids of correction factors for each of the CCD pixels, one grid for the Working diffuser and one for the Reference diffuser. In addition, each of these grids was fit to a polynomial in azimuth (3^{rd} order) and elevation (4^{th} order). The parameters of these fits were also included in the delivered database.

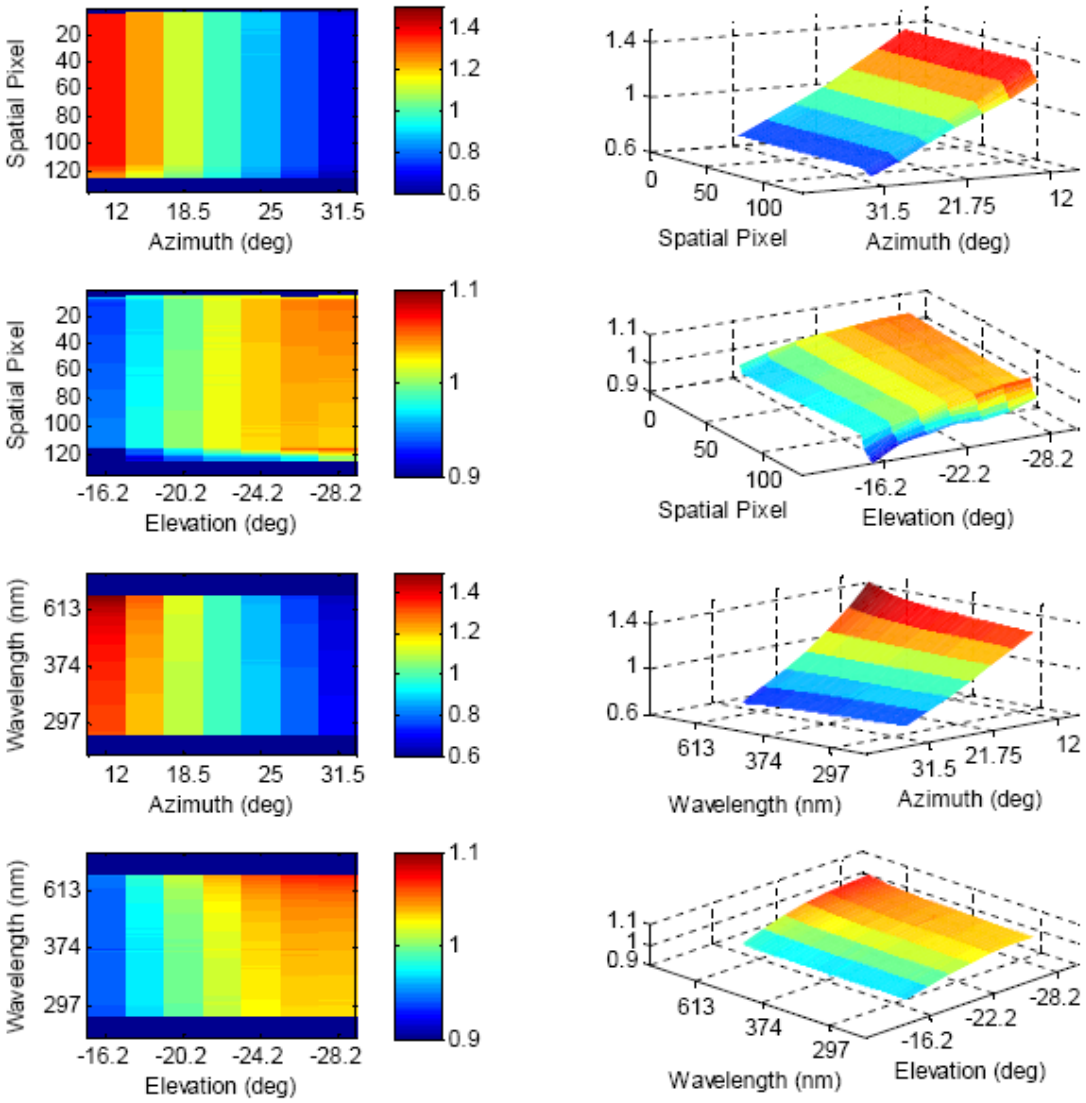

Figure 1-22 2-dimensional slices are shown through the 4-dimensional irradiance goniometry cube as delivered for the Working diffuser in the Center High Gain aperture. (courtesy of BATC)

Database uncertainty

The uncertainty in the goniometric characterization is primarily systematic. Random errors caused by measurement noise and lamp drift corrections are reduced to negligible levels by the smoothing procedure in the characterization. Significant systematic errors can arise from imperfect regression of the data in solar angle and non-sunlike test illumination. Test illumination angles in the spacecraft reference frame are known quite accurately. Because goniometry is a measure of relative irradiance response, many of the absolute irradiance error terms are not present. A conservative estimate for residual goniometry characterization errors is 0.2%.

1.7.8 Stray light sensitivity (SLT)

The stray light mitigation features of OMPS/LP described in Section 1.5.2 are insufficient to reduce stray light to a negligible level. A stray light characterization is necessary if residual stray light is to be removed in ground software. Stray light caused by optical surface roughness is best characterized by measuring the point spread functions (PSFs) of the sensor. Incident light at a specific angle and wavelength is destined for a unique spot on the CCD. Internal scattering causes the spot to spread in both the spatial and spectral directions. Each PSF is therefore the sensor response at all wavelengths and angles to a monochromatic point source. A full ensemble of PSFs convolved with the source radiance distribution yields an estimate of the stray light response at every pixel of the detector.

Another form of stray light, known as ghosts, results from back-reflections off transmitting optics. Both PSFs and ghosts were measured by illuminating the sensor with a series of monochromatic point sources from the tunable laser. Six wavelengths (293, 350, 430, 495, 700, and 1000 nm) were measured at the top, middle, and bottom of each slit. Each aperture was independently illuminated, yielding a total of 108 response images (see Figure 1-23). In addition, the sensor was tested for out-of-field stray light by illuminating the apertures above and below the elevation angle range of the slits. No signal above the background was observed during out-of-field illumination. This means that all sources of stray light are within the spectral and spatial measurement range of the instrument.

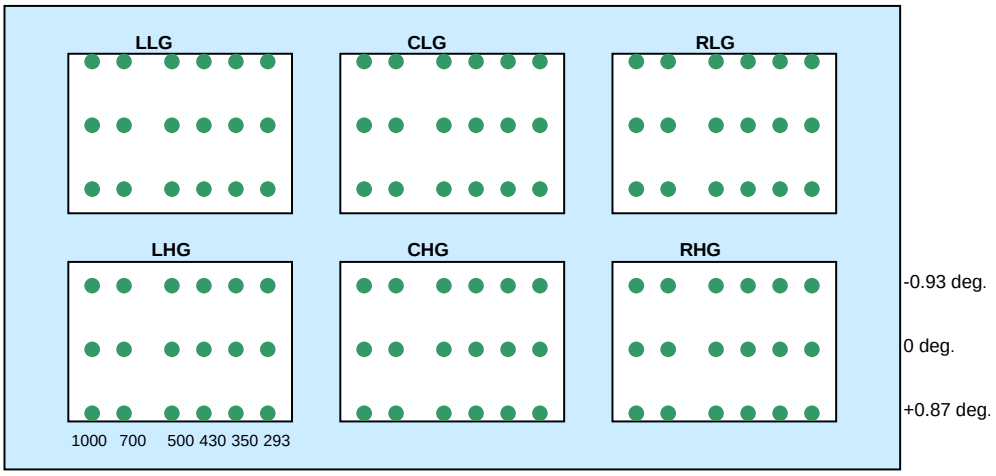

Figure 1-23 Schematic showing the laser source locations for the stray light characterization of OMPS/LP. (courtesy of BATC)

The estimation of stray light at a specific wavelength and altitude (the target pixel) requires knowledge of PSFs and ghosts at all wavelengths and altitudes that can potentially contribute signal (the source pixels). There are of order 100 source pixels for every target pixel in OMPS/LP. Earth signal differentials across the focal plane can be as large as 5 orders of magnitude. Combining these two facts means each source pixel's PSF or ghost contribution must be known with an accuracy of 10^{-9} relative to its signal in order to achieve 1% stray light knowledge in any target pixel. Thus the

PSF characterization requires that signals of 10^{-9} times the laser source signal must be detectable above the measurement noise level.

The challenge of stray light characterizations was achieving adequate SNRs for all portions of a PSF. Short integration times and neutral density filters allow measurements at the laser wavelength and elevation without saturation. Much longer integrations without the filters brings the PSF tails above the noise level but saturates pixels measuring in the central portion of the PSF. By combining, or stitching, the various measurements a full PSF and ghost response can be obtained without saturated or noisy pixels. Stitching starts at the PSF tails with the longest integration times. Pixels that are saturated in these data are replaced by data from the next shorter integration, which also contains some saturated pixels closer to the PSF peak. This substitution continues until no saturated pixels remain. The measurement sets are "stitched" together by scaling signal levels so they match in overlap regions. An example of stitched measurements for the Center Low Gain aperture is shown in Figure 1-24.

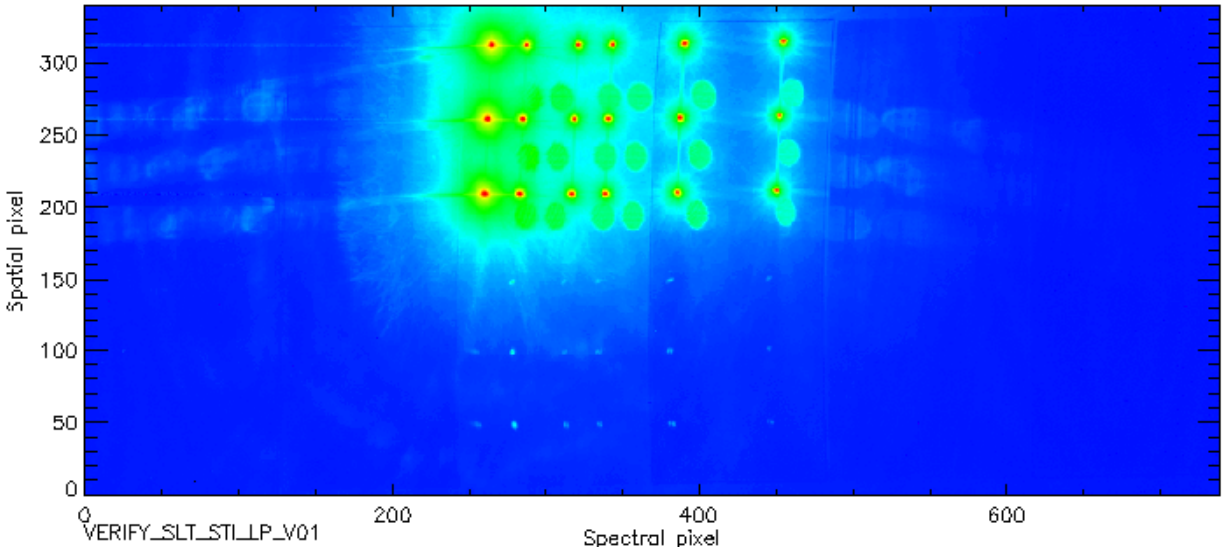

Figure 1-24 Stitched PSFs and ghosts shown combined for the 18 measurements in the Center Low Gain aperture. Source wavelengths and elevations are located at the red dots. Primary ghosts from the detector window are seen as ovals below and to the right of each source. False signals seen as dots in the low spatial indices are caused by a small light leak in the test setup. (courtesy of BATC)

The stitched results are not adequate for use in stray light corrections because they contain natural discontinuities whose locations depend on the exact wavelength and elevation of the laser source. These discontinuities must first be removed before the sparse grid of measured PSFs and ghosts can be interpolated to any pixel within an aperture. These discontinuities occur at filter boundaries and at the aperture boundaries. The step of the analysis, called reconstruction, also separates PSFs and ghosts. Figure 1-25 contains an example of a spectral slice through a PSF before and after reconstruction.

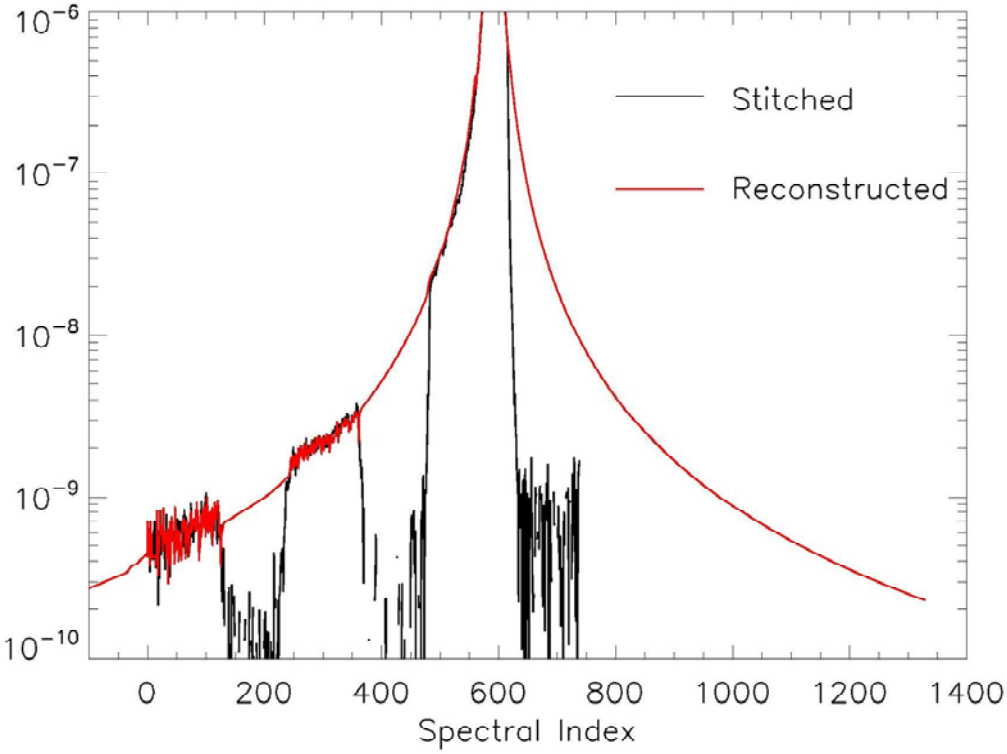

Figure 1-25 Spectral slices for the mid-slit stitched (black) and reconstructed (red) PSFs of the Right High Gain aperture, 430 nm. The data are normalized to the signal sum in an 11x11 pixel box surrounding the source.

The final step in creating PSF and ghost deliveries for use in the SDR algorithm is called tuning. As part of stray light verification, a Xenon arc source was used to illuminate each aperture over a limited elevation angle range. The wavelength range was also reduced through the use of cutoff filters. The result was a patchwork of illuminated regions that acted as stray light sources. Figure 1-26, Panel A contains an example of one of these patches.

The detector response, shown in Panel A, was simulated by convolving the reconstructed PSFs and ghosts with the source irradiance. A comparison of the simulated result, shown in Panel B, with the original yields percent ratios as shown in Panels C and E. Any deviation from 100% is an indication of an error in the stray light model – most likely in the PSF and/or ghost models. These errors arise from the sparse measurement set and from inadequate SNR in the PSF tails. Through a series of adjustments to the PSF tails and ghost model the stray light model is tuned to the broadband measurements. This is an iterative process involving all the other broadband patches within each aperture, 15 in all. The comparison between measured and post-tuning simulated signals for the selected patch in Figure 1-26 is shown in Panels D and F. The tuning was only applied to 1000 nm PSFs. No tuning was necessary at the 5 other wavelengths. The transmission characteristics of the window filter were also adjusted.

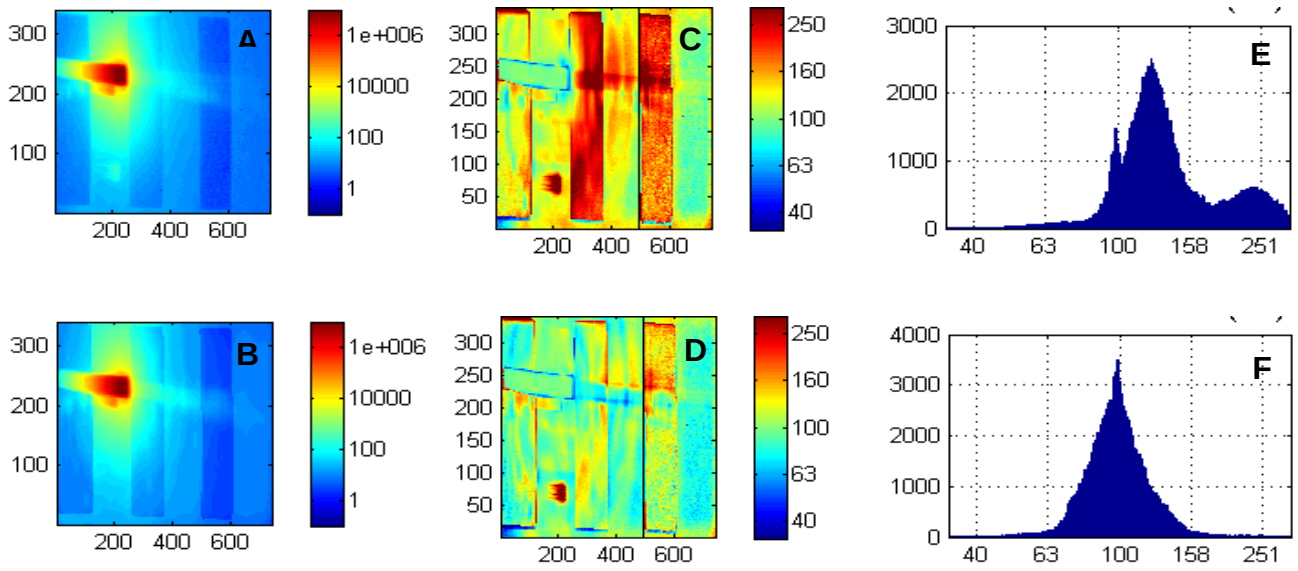

Figure 1-26 The stray light tuning process. Panel A contains the results of a single broadband measurement, and Panel B are the integrated PSF and ghost responses intended to duplicate Panel A. Panel C contains the ratio B/A prior to tuning, and Panel D contains the ratios afterward. Panels E and F contain the same results in histogram form. All ratios are expressed in percent. (Courtesy of BATC)

The delivered database consists of the tuned, reconstructed, and stitched PSFs, and the ghost model. Each database contains results for each of the 108 individual measurements. And for each of those measurements a normalized response is reported. Normalizations are relative to the signal summation within an 11×11 pixel grid centered on the wavelength and elevation of the laser source. For the stitched PSFs the total response is over the 340×740 detector pixels. The area is doubled to 680×1480 pixels for ghosts, reconstructed and tuned databases to ensure a PSF or ghost value regardless of which pixel is modeled as the source. The 90 stitched broadband measurements are provided in a separate database.

Database uncertainty

Pre-launch characterization errors had a variety of origins. Measurement time and sensor dynamic range constraints resulted in measurement noise of approximately 10^{-9} of the peak signal. While this may seem like an extremely small error source, the discussion earlier in this section indicates this is approximately 1% of the stray light signal in a given pixel. External stray light present in the measurement setup also contributed signal errors. These features were subtracted from the data when they could be identified. The PSFs themselves could not be completely measured due to the finite extent of the detector and the window filters. Full 2-dimensional PSFs were reconstructed from the data. Finally, comparisons with a set of stray light verification measurements indicated

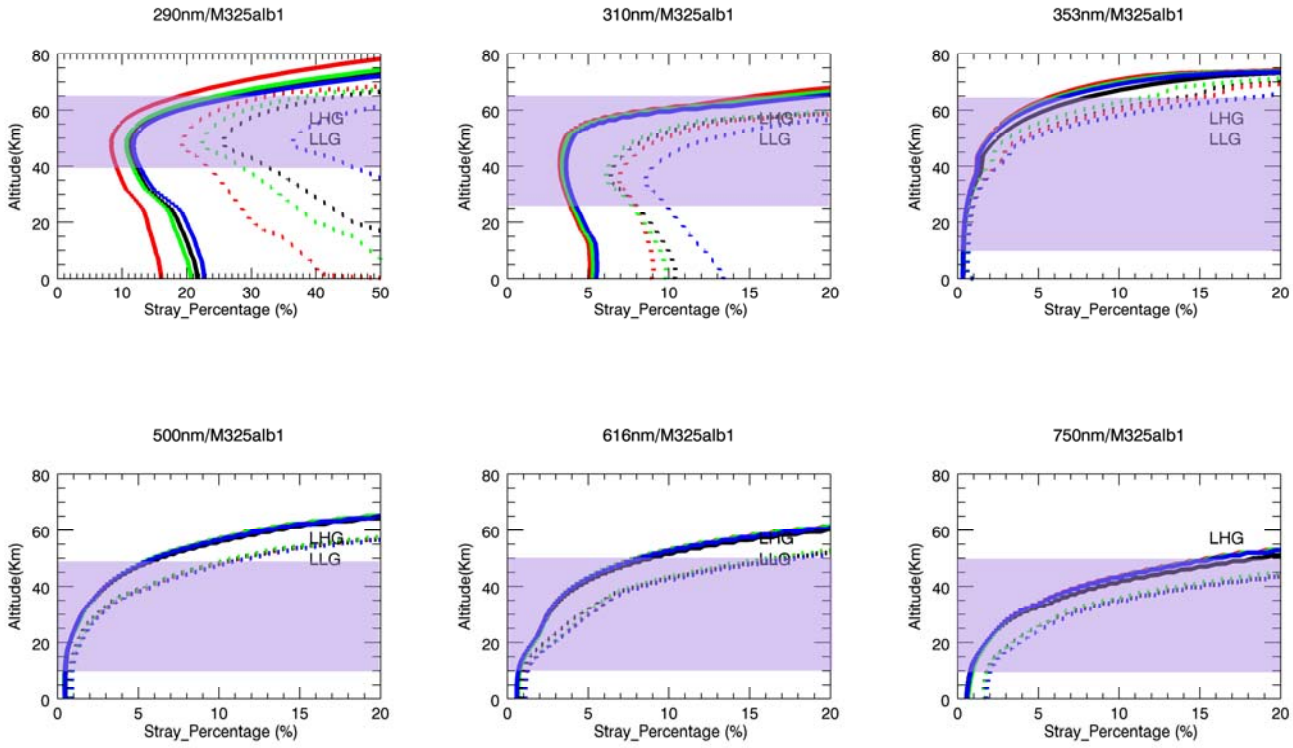

Figure 1-27 Plots of stray light in the OMPS/LP left slit for selected wavelengths. Solid lines are for the high gain aperture and dotted lines are for low gain. Red curves are the modeled stray light using the tuned PSFs and green curves utilize untuned PSFs. Blues curves are the result of adding 10^{-9} uniformly to the tuned PSFs. Shaded areas indicate the approximate altitude range over which the signal is important for retrievals.

errors in the reconstructed PSFs. In order to address these errors the PSFs were tuned until they agreed with the verifications.

The effect of these error sources on the stray light correction was estimated by introducing changes to the final, tuned PSFs and observing the resulting changes in modeled stray light. Changes were chosen to represent bounding cases. For example, stray light for typical Earth radiance scenes was modeled using tuned and untuned PSFs. Modeling was also performed with PSFs modified by the addition of 10^{-9} everywhere. Results for these tests are shown in Figure 1-27 for the left slit, which typically has the greatest stray light as a fraction of the signal.

The greatest stray light and the largest uncertainty occurs at the shortest UV wavelengths. Here, stray light differences between the various models approach a factor of 2 in the low gain. However, only the high gain aperture data are used in UV, and there the potential errors are 5–10%. Through much of the VIS and near-IR model differences do not exceed 1% below 45 km. Model differences at 1000 nm (not shown) can easily exceed 50% at 25 km.

1.7.9 Non-linear response (LED)

The variation in sensor electronic gain as a function of signal level is its non-linearity. In this context gain refers to the conversion from number of electrons generated at a pixel to digital counts produced by the analog to digital converter (ADC). The calibration coefficients, which convert incident energy to digital counts, are independent of signal level. Therefore, the non-linearity must be corrected before applying these coefficients to the counts. For Earth-view data this correction is performed by the flight electronics. The SDR algorithm therefore applies no correction. No in-flight correction is performed for calibration data. As a result the SDR must correct these data.

The linearity of the signal processing electronics is measured relative to the sensor timing clock by comparing signals obtained at different integration times. Since the clock controls the CCD integration time very precisely, the observed counts should scale with the integration time provided the electrons are generated at a constant rate. The degree to which these do not scale is a measure of the non-linearity. The source of photoelectrons for both the pre-launch linearity characterization and post-launch linearity monitoring is the on-board LED. The LED illuminates the entire CCD with integration times that vary (see Section 1.6.3) from 0 to well beyond the time needed to fill the pixel wells. Non-linearity correction factors are computed by fitting ideal counts as a function of the measured counts. The ideal counts are those that result from a linear system, and are found by scaling a reference count level by the integration times. The system is, by definition, linear at the reference count level. This count level is arbitrary. The only requirement is that linearity corrections used in deriving radiometric calibrations be based on the same reference count level.

The delivered linearity correction is a table with 16383 entries, where 2^{14} = 16,383 is the maximum count for a pixel from a single frame. Each entry is the regression result evaluated at the index of that entry. For example, to find the entry for an index of 10,000 means finding the ideal count for 10,000 measured counts. If the non-linearity is –2% at this signal level (meaning the system under-responds by 2%), the table entry is 10,200.

1.7.10 Polarization sensitivity

OMPS/LP is designed to be polarization insensitive, meaning it should have the same or similar response regardless of the polarization state of the incident light. The goal of 1% linear polarization sensitivity (LPS) was chosen because it represents a radiometric error that can be ignored. Since the LPS varies slowly with wavelength and most retrieval techniques utilize some form of wavelength differentials, the effective radiometric error is much less than 1%. Since the SDR algorithm performs no correction, no LPS characterization was delivered. Instead, the LPS was measured to ensure it met the 1% goal.

The polarization sensitivity was measured by rotating the plane of linearly polarized light incident at the sensor entrance aperture. The amplitude of the resulting signal variation yields the LPS. Linearly polarized light is created via the combination of a Wollaston prism and a half-wave plate. This prism produces two orthogonally polarized light beams, and the half-wave plate rotates the plane of polarization of each. Since half-wave plates work perfectly at only one wavelength, 2 plates were used and a correction factor applied for non-optimum wavelengths.

The resulting LPS is shown in Figure 1-28 for the right slit. The right slit is the only one not compliant with the 1% LPS goal. It should be noted that high altitude, UV-based retrievals tend to originate with measurements from the High Gain, and the lower altitude, VIS-based retrievals come more from the Low Gain. The Low Gain data shown in Figure 1-28 has better performance in the VIS and NIR (low spectral indices), and the High Gain has better performance in the UV (high spectral indices).

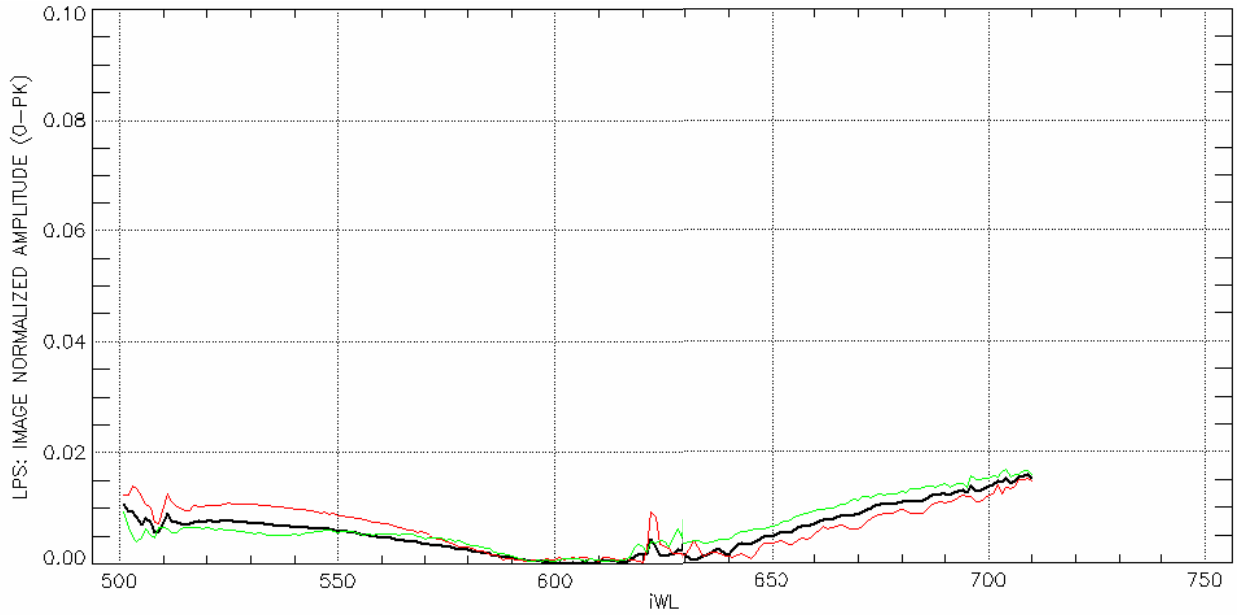

Figure 1-28 LPS is shown as a function of spectral index (inverse of wavelength) for the Right slit, Low Gain aperture. The red and green lines are independent results for the two Wollaston images. The black line is the result of comparing the two orthogonally polarized images. Spectral indices near iWL = 625 correspond to the UV filter boundary near 360 nm. (courtesy of BATC)

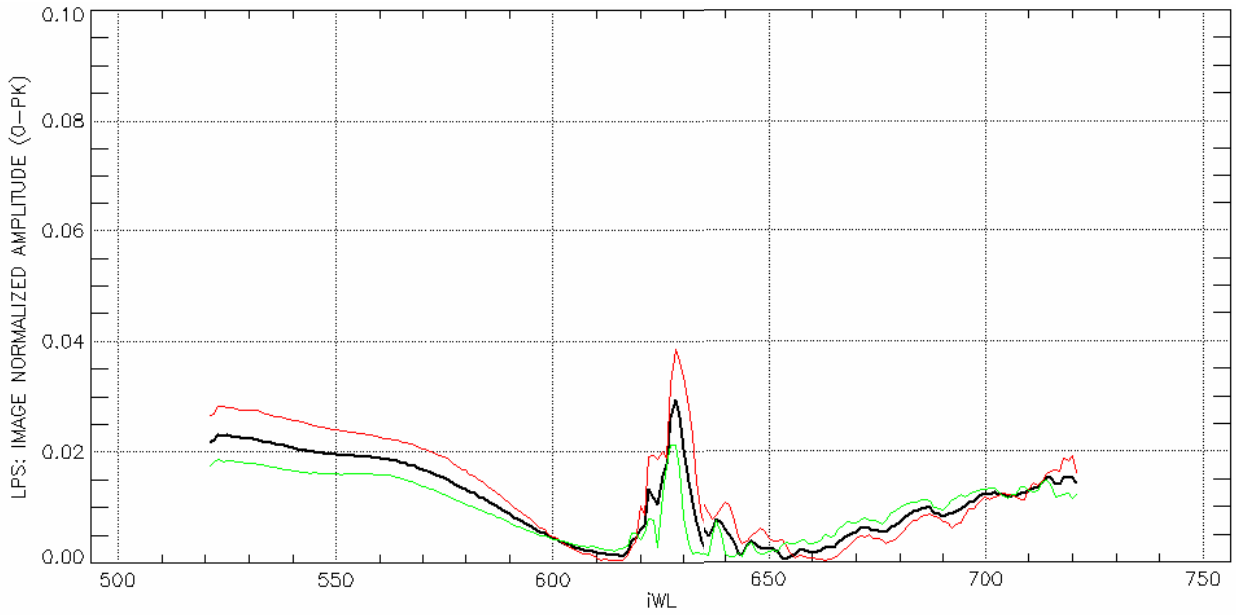

Figure 1-29 LPS is shown as a function of spectral index (inverse of wavelength) for the Right slit, High Gain aperture. The red and green lines are independent results for the two Wollaston images. The black line is the result of comparing the two orthogonally polarized images. Spectral indices near iWL = 625 correspond to the UV filter boundary near 360 nm. (courtesy of BATC)

2 SDR ALGORITHM OVERVIEW

2.1 Overall concept

The OMPS/LP Algorithm has two main modules:

1. The **Sensor Data Record (SDR)** algorithm, which
    a. converts raw Earth-view data from the sensor into calibrated, spectrally/spatially registered, and geolocated radiances.
    b. processes the on-board calibration data in order to maintain knowledge of sensor calibration and characteristics (some updates are automatically incorporated into data processing while others are not)
2. The **Environment Data Record (EDR)** algorithm, which retrieves science data from the SDR radiances.

The general philosophy of the SDR algorithm and associated SDR output file is that it include as much as possible the information needed in a subsequent retrieval algorithm. This philosophy has, for instance, led to inclusion of ancillary temperature and pressure data in the SDR output. The choice of what data to include and how it is matched to LP measurements is admittedly subjective, but the SDR user has the option to use it or introduce his own. Convolution of simulated radiances over the sensor band pass and field of view are traditionally performed in retrieval algorithms, and OMPS/LP is no exception. The functions defining the OMPS/LP band passes and fields of view are input directly to the EDR code, and are not written in the SDR output product.

The SDR output must serve multiple retrieval approaches, some known and others unknown. Doing so requires a balance be struck between providing the fundamental information that any retrieval algorithm can use, though with some difficulty, and providing more refined results that tend to be algorithm specific. For example, the SDR naturally produces calibrated radiances for each measured pixel. But because of the complicated relationship between pixel row/column and wavelength/altitude, many retrievals (including the EDR algorithm) cannot use pixel-level radiances. To accommodate the EDR and similar retrieval algorithms, the SDR algorithm produces calibrated radiance data in two formats, ungridded and gridded. The ungridded data is organized per CCD pixel, whereas the latter dataset uses a two-dimensional cartesian grid (wavelengths vs tangent altitude) to remap the radiance data from the original CCD-based format. The EDR algorithm uses gridded radiances. Including the ungridded radiances as well supports the use of alternative gridding schemes or entirely new retrievals that can use the ungridded data directly.

The OMPS/LP mission on NPP will be the first real test of this sensor design. Since the SDR algorithm is closely tied to sensor design and performance, it too is somewhat experimental. Throughout the remainder of this document an SDR algorithm approach is described that assumes predicted sensor performance. In general the algorithm is designed to be flexible and modular, so that when and if the sensor behaves unexpectedly disruptions to the code will be minimal. One area of flexibility is related to sensor operations, where pixel sampling and data collection timing are selectable. Though the proposed sensor operations utilize only a limited set of sampling/timing

combinations, the SDR algorithm is designed to accommodate the full flexibility of the sensor, should it be exploited in the future.

As shown in Figure 2-1, the SDR module reads the appropriate Raw Data Records (RDRs) and writes its output into the Hierarchical Data Format (HDF) Sensor Data Record (SDR) file that contains most of the dynamic information needed by the EDR Algorithm. The RDRs are little more than the data packets received directly from the sensor. The EDR algorithm in turn reads the SDR file, together with a series of ancillary files, performs the retrievals of ozone and aerosol profiles and writes its output into the HDF formatted Environmental Data Record (EDR) file.

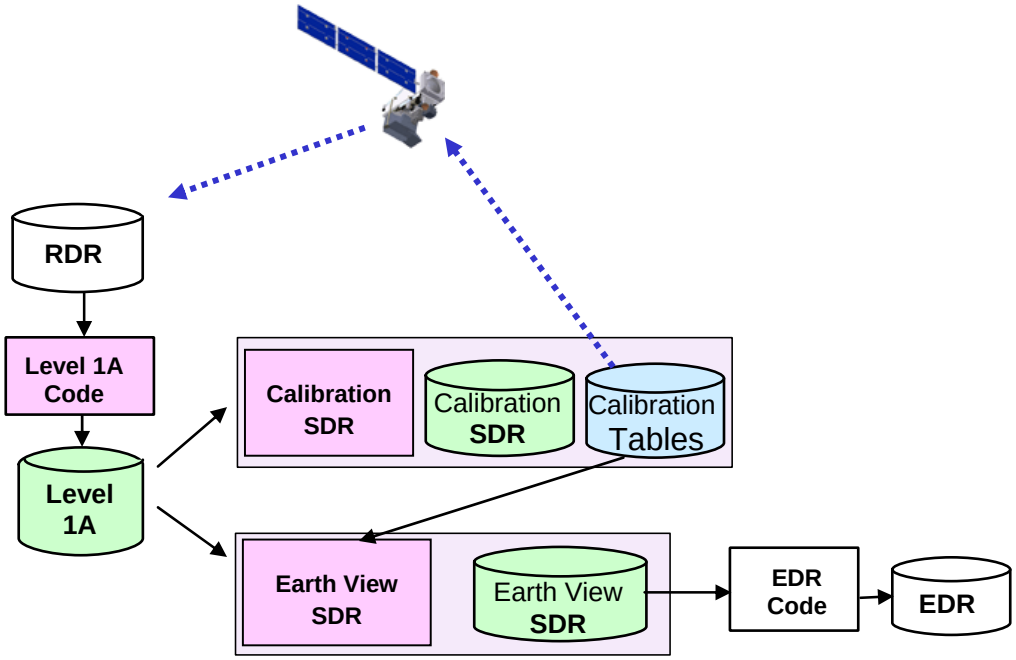

Figure 2-1 Schematic showing SDR processes (in color) in the context of the overall data flow. Green and blue objects represent data sets used and/or created by the algorithm.

The SDR algorithm processes two basic OMPS RDR types, Earth-view and calibration, to produce two corresponding SDR types. Calibration processing also produces a series of datasets that store the results of calibration analyses. The Earth-view SDR processing subsequently uses these calibration datasets to adjust the spectral and radiometric characteristics of Earth-view data. The signal correction and calibration analysis components of SDR processing are fully automated with some fault tolerance. Application of calibration adjustments can be automated as well, once it is deemed necessary. Key elements of the SDR code are as follows:

- Level 1A process

The Level 1A is an intermediate product intended to prepare raw data for ingest into the SDR codes. RDR files produced by the NPP ground systems are separated by APIDs (see Table 1-3), but may not necessarily be time-ordered and may contain duplication. The Level 1A code removes the packet structure used in telemetering the data, performs reordering and error-checking, and restructures the data.

- Level 1A data
  The data produced by the Level 1A processing is stored in an HDF5 file. Each Level 1A file represents a single orbit. Data within a file is organized according to its APID groups and Profile ID subgroups. Each OMPS Profile describes a unique combination of sensor settings such as measurement timing and pixel selection. Also included in the Level 1A file are the OMPS housekeeping data and spacecraft attitude and ephemeris.

- Earth view SDR processes
  Earth view data are processed through a series of algorithms that populate the final SDR output file. The separate algorithms include the main signal processing code, the geolocation code, and measurement re-gridding code.

- Earth view SDR data
  Earth view data are processed through a series of algorithms that populate the final SDR output product. The primary output is measured radiance at each pixel. Long and short integration measurements are merged, but high and low gain measurements are left separate. Other data are provided to make sense of the Earth view data, such as warning flags, geo-location information, external temperature and pressure profiles, and pixel band centers. Table 2-2 describes the organization of these data in the SDR output. The original input counts are provided along with the values of corrections used to transform these into the final radiances. Since many retrieval algorithms require radiances on a uniform tangent height altitude and wavelength grid, radiances interpolated to such a grid are also provided.

- Calibration SDR processes
  Data brought down with a Calibration APID are processed in a similar manner to Earth view data. The primary difference is that each type of calibration data requires different corrections and is stored differently in the output product.

- Calibration SDR data
  The calibration SDR product contains processed lamp solar and dark measurements organized by activity type. For example, LED data obtained for pixel aliveness testing are distinct from those used for linearity. All results are per image, meaning no temporal averaging or aggregation is performed. These data are suitable for input to subsequent analysis, trending, and monitoring algorithms.

- Calibration tables
  Averaged or otherwise trended calibration data are stored in what are generically referred to as tables. These tables are no more than files containing the appropriate results for each pixel.

Depending on how the table data are used, all results can be contained in a single or multiple files.

2.2 SDR inputs and outputs

Each of the SDR process elements described in the previous sub-section has a variety of inputs and outputs. Ultimately, only one output product matters, the Earth-view SDR. But the other ancillary products are essential, and knowing what they are and where they fit in aids the understanding of how the SDR process is structured. A list of inputs and outputs for the basic SDR components is given in Table 2-1. A high-level description of SDR contents is given in Table 2-2.

Table 2-1 SDR input/output files

Algorithms	Inputs	Outputs
Level 1A	- OMPS/LP Raw Data Record (RDR) - Spacecraft Attitude & Ephemeris Raw Data Record (RDR)	- Level 1A File
Earth-view SDR	- Level 1A File (APIDs 563, 579) - Pixel Sample Table - Sensor Timing Table - Characterization Databases - Calibration History Files - Temperature & Pressure Data	- Earth-view Sensor Data Record File (SDR)
Calibration SDR	- Level 1A File (APIDs 566, 582) - Pixel Sample Table - Sensor Timing Table - Characterization Databases - Calibration History Files	- Calibration Sensor Data Record File (SDR) - Calibration History Files - Sensor Upload Tables

Table 2-2 SDR output file data groups (HDF5)

Earth-view SDR	
Ancillary data	Group containing externals: NCEP data
Array pointers	Index arrays that map data in 1-D output vector to: CCD row/column, slit index, high/low gain index, spectral index
Calibration data	Group containing: raw data, data corrections applied, intermediate results, baseline irradiance, and selected sensor telemetry (temperatures)
Geolocation data	Standard geolocation information, at tangent point
Science data	Group containing: radiances, radiance uncertainties, flags
Gridded data	Science and ancillary data interpolated to

	wavelength/altitude grid
Calibration SDR	
Calibration data	Group containing: calibration coefficients, wavelengths, pointer arrays
Profile ID = 1 data	Group containing: corrections for PID=1 data, corrected or calibrated signals for PID=1 data
: **:**	The data group for a specific Profile ID appears in the output only if the input contained those data
Profile ID = n data	Group containing: corrections for PID=n data, corrected or calibrated signals for PID=n data

3 EARTH-VIEW SENSOR DATA RECORD (SDR) ALGORITHM

3.1 Earth-view corrections – physical basis

The purpose of SDR processing of Earth-view data is to produce the calibrated, geo-located radiances required for input to the retrieval process. Furthermore, a goal of the SDR processing is to include as much information within the SDR output product to support retrievals and eventual re-processing. This means that, for example, temperature and pressure profiles needed by the EDR processing code are bundled into the SDR product. Also, raw data from RDRs along with corrections applied within the SDR code are included in the output. In this way reprocessing of the SDRs can commence from the previous SDR process and might skip certain calculations that have not changed.

The SDR code reverses the process performed by the sensor when it converts Earth radiances L collected by the telescope into signals C_{ADC} telemetered to the ground. This conversion, for a single pixel identified by CCD row i and column j, is represented by the following idealized equations.

$$C_{ADC}(i,j) = C_{Bias}(i,j) + g \cdot \ell(Q_{tot}) \cdot Q_{tot}(i,j) \tag{3-1}$$

where

$$Q_{tot}(i,j) = Q_{photon}(i,j) + Q_{smear}(i,j) + Q_{dark}(i,j) \tag{3-2}$$

and

$$Q_{photon}(i,j) = \iint L(\lambda,\Omega)\, S_{i,j}(\lambda,\Omega)\, \tau(\lambda,\Omega)\, QE_{i,j}(\lambda)\, d\lambda\, d\Omega \tag{3-3}$$

$C_{ADC}(i,j)$	Digital counts output by the analog/digital converter for pixel i,j and telemetered to the ground
$C_{Bias}(i,j)$	electronic offset introduced prior to A/D conversion
$Q_{tot}(i,j)$	total number of electrons generated by the detector for pixel i,j
g	number of digital counts generated per detector electron
$\ell(Q_{tot})$	non-linearity in the electronic gain
$Q_{photon}(i,j)$	response in electrons of pixel i,j to incident photons
$Q_{smear}(i,j)$	photoelectrons collected during the parallel transfer of the CCD readout
$Q_{dark}(i,j)$	electrons (primarily temperature induced) generated by the CCD itself
$L(\lambda,\Omega)$	number of photons of wavelength λ and angle Ω incident at the sensor entrance aperture
$S_{ij}(\lambda,\Omega)$	normalized sensor response at pixel i,j to photons of wavelength λ and angle Ω

$\tau(\lambda,\Omega)$ sensor optical throughput of photons of wavelength λ and angle Ω

$QE_{ij}(\lambda)$ Quantum Efficiency (conversion efficiency of photons into electrons by the detector) of pixel *i,j* for photons at wavelength λ

An inversion of these equations by the SDR code will yield Earth radiances as measured by each pixel. This inversion process is simplified by linearizing the governing equations. In particular, the detector response $Q_{photon}\ (i,j)$ can be broken into in-band, in-field contributions, and out-of-band, out-of-field contributions, such that

$$\begin{aligned} Q_{photon}(i,j) = & \iint_{IN} L(\lambda,\Omega)\, S_{i,j}(\lambda,\Omega)\, \tau(\lambda,\Omega)\, QE_{i,j}(\lambda)\, d\lambda\, d\Omega \quad + \\ & \iint_{OUT} L(\lambda,\Omega)\, S_{i,j}(\lambda,\Omega)\, \tau(\lambda,\Omega)\, QE_{i,j}(\lambda)\, d\lambda\, d\Omega \\ = & \quad Q_{ideal} \quad + \quad Q_{stray} \end{aligned} \tag{3-4}$$

The in-band and in-field regions are defined such that the Earth radiance *L* and sensor throughput τ can be assumed linear in wavelength and angle within the range. The resulting signal can then be written as

$$Q_{ideal}(i,j) = L_{ij} \cdot \tau QE_{ij} \cdot t_{\text{int}} \tag{3-5}$$

where sensor response has been combined into a single term, τQE, for each pixel, and the integration time is written as t_{int}. The in-band portion of $S_{ij}(\lambda,\Omega)$ is often referred to as the slit function or pixel bandpass, and the in-field portion the pixel FOV function. The $S_{ij}(\lambda,\Omega)$ term has been eliminated from the above equation because it is a normalized quantity for each pixel. However, it is certainly not linear in wavelength and angle, and ignoring it therefore constitutes an error. This error is corrected in the EDR retrieval code where the true bandpass and FOV functions are used to model measured radiances.

Representing the ideal signal as a simple product of sensor response and incoming radiance helps with sensor characterization as well as SDR corrections. In this way the source spectrum used in ground calibrations need no longer match the spectrum measured while in orbit. And every in-orbit spectrum need not be identical to maintain proper calibration.

Dependency of sensor response on the source spectrum has not been eliminated, but rather isolated in the Q_{stray} term. These are the photoelectrons that result from out-of-band, out-of-field stray light. This term is sometimes negligible in nadir-viewing sensors that use scan mirrors and that have good out-of-band rejection. Most UV/VIS limb sensors suffer from some form of stray light, and OMPS/LP is no exception. Treatment of stray light in the SDR is discussed in Section 3.2.5.

A description of the SDR pixel radiance computation begins by solving Equation $Q_{ideal}(i,j) = L_{ij} \cdot \tau QE_{ij} \cdot t_{\text{int}}$ (3-5 for *L* and replacing all electrons with counts using the conversion factor *g*.

$$L_{ij} = \frac{g \cdot Q_{ideal}(i,j)}{g \cdot \tau QE_{ij} \cdot t_{\text{int}}} = \frac{C^r_{ideal}(i,j)}{g \cdot \tau QE_{ij} \cdot t_{\text{int}}} \quad (3\text{-}6)$$

OMPS/LP has a single electronic gain, meaning g is a constant. Therefore a radiance calibration constant k^r_{ij} can be defined for each pixel.

$$k^r_{ij} = \frac{1}{g \cdot \tau QE_{ij}} \quad (3\text{-}7)$$

$$L_{ij} = \frac{k^r_{ij} \cdot C^r_{ideal}(i,j)}{t_{\text{int}}} \quad (3\text{-}8)$$

This set of constants, referred to as the radiance calibration coefficients, was measured during sensor radiometric calibration on the ground. Since the laboratory sources are calibrated in units of power rather than photons, the units of these coefficients are Watt·second·cm^{-3}·steradian^{-1}·count^{-1}. Note that since these coefficients relate source radiance to ideal counts, it was necessary to apply a stray light correction to the calibration measurements prior to deriving the coefficients.

3.2 Earth-view data processing

The goal of Earth signal processing is to obtain for each reported data cell, a calibrated Earth radiance and radiance uncertainty, observation angles, geo-locations, and ancillary co-located atmospheric data from assimilated external data or other NPOESS sensors. As discussed in Section 2.1, the SDR product contains both ungridded and gridded output, so a data cell represents a measured pixel for the case of the former, and a grid point for the latter. Gridded radiances are produced from the ungridded radiances. These constitute the set of OMPS data needed by the LP EDR algorithm for ozone profile retrievals. Figure 3-1 shows the flow for processing each orbit of raw data contained in a Level 1A file. Detailed discussions of the processes, corresponding to the individual elements in Figure 3-1, are contained in subsections that follow.

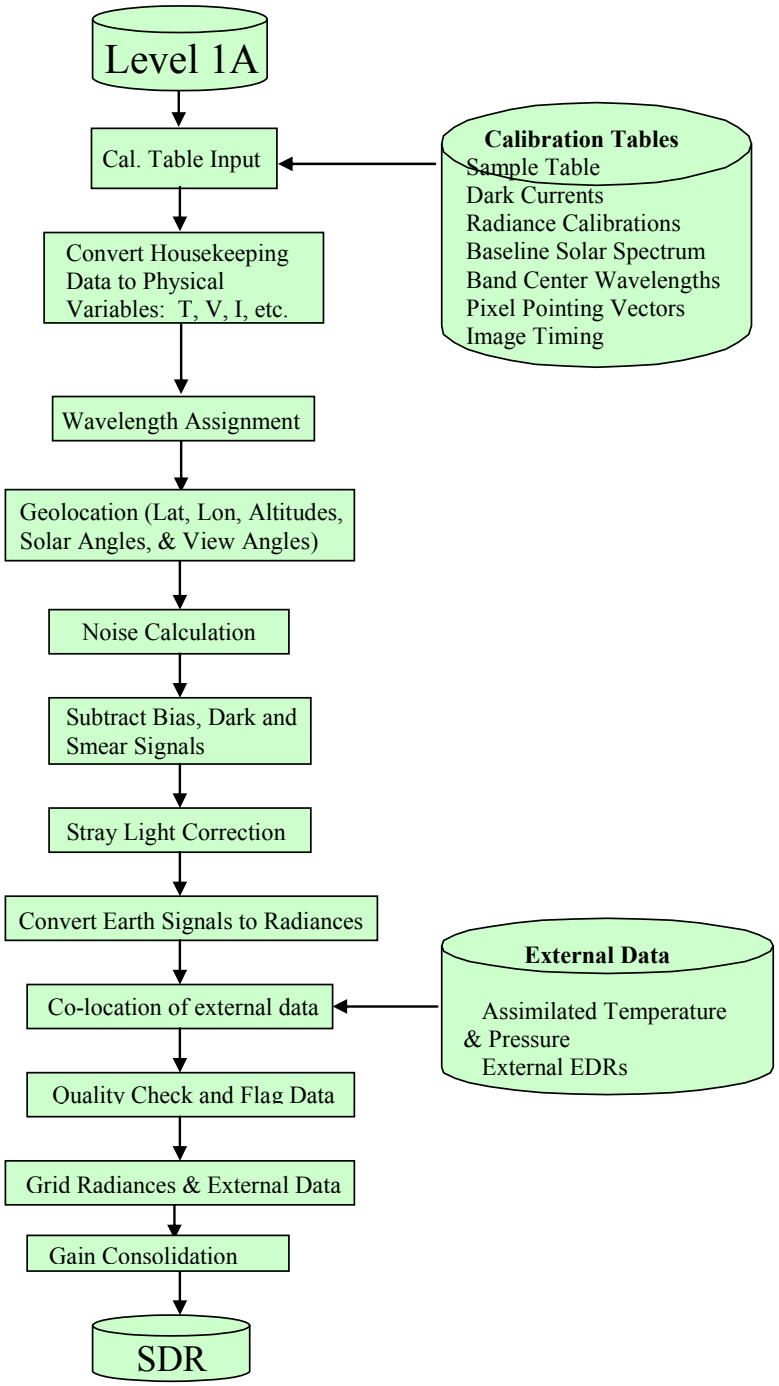

Figure 3-1 Schematic showing the Earth-view SDR generation process.

3.2.1 Wavelength Assignment

Table 3-1 Wavelength assignment input/output list

Input	**Input Source**
Solar calibration band center wavelengths, λ_{ij}	Calibration history file
Prism temperature during solar calibration, T_c	Calibration history file
Prism temperature during current image, T	Level 1A
Wavelength thermal coefficients, $(d\lambda/dT)_{ij}$	Operational parameter file
Output	**Output Destination**
Earth view band center wavelengths, λ'_{ij}	SDR File

Band center wavelengths are computed for every pixel reported in an SDR file. These wavelengths are derived from the initial or baseline wavelength registration, $\lambda_{ij\ initial}$, and the drift in band centers derived from subsequent solar measurements. The trending in time of the wavelength registration, described in Section 5.2, yields solar calibration band centers λ_{ij} for every pixel at an arbitrary point in time following the last solar measurement. Predictions of this type are quite accurate if the drift in wavelength registration is slow, such as from an annual thermal cycle.

The wavelength registration for solar measurements is not necessarily accurate for Earth view measurements due to changes in registration within each orbit. The primary cause of these changes is intra-orbital temperature variations resulting from solar illumination. These temperature changes cause the optics to shift, especially the focal plane. The index of refraction of the dispersing prism is also temperature dependent. The prism mount was designed to thermally isolate it from the rest of the sensor, with models indicating between 0.5 and 1.0 ºC peak-to-peak variation through an orbit. However, the index of refraction sensitivities are so large that this temperature change causes 5 – 10 hundredths of a pixel shift in the spectral direction.

$$n^2(\lambda) - 1 \quad = \quad \lambda^2 \sum_{k=1}^{3} \frac{B_k}{\lambda^2 - {\lambda_k}^2}$$

The Sellmeier equation (see Equation (5-6)) relates the index of refraction n of various transparent materials to wavelength. Differentiation of this relationship with respect to wavelength describes how the band center wavelength λ varies as the prism index of refraction n is thermally modified.

$$\frac{dn}{d\lambda} \quad = \quad -\frac{\lambda}{n} \cdot \sum_{k} \frac{B_k \lambda_k^2}{\left(\lambda^2 - \lambda_k^2\right)^2} \tag{3-9}$$

where B_k and λ_k are known constants for fused silica, but can also be derived empirically from the initial wavelength registration.

The following expression (ref: *Schott Glass*) approximates the thermal response of the refractive index for a wide number of materials:

$$\frac{dn(\lambda,T_c)}{dT} = \frac{n^2-1}{2n}\left[D_0 + 2D_1\Delta T + 3D_2\Delta T^2 + \frac{E_0 + 2E_1\Delta T}{\lambda^2 - {\lambda_{TK}}^2}\right] \tag{3-10}$$

where T_c is temperature of the prism during the solar measurements, ΔT is T_c minus some reference temperature (usually 20°C), and the D and E parameters, along with λ_{TK}, are empirical quantities determined for each material. The change in index of refraction, when applied to the Sellmeier equation, yields the change in band center wavelength. Using published parameters for fused silica (there is little or no difference in parameters for various types of fused silica), Equation $\frac{dn(\lambda,T_c)}{dT} = \frac{n^2-1}{2n}\left[D_0 + 2D_1\Delta T + 3D_2\Delta T^2 + \frac{E_0 + 2E_1\Delta T}{\lambda^2 - {\lambda_{TK}}^2}\right]$ (3-10 accurately describes the spectral registration shifts observed during pre-launch thermal vacuum tests of the OMPS/LP sensor.

For a pixel of wavelength λ_{ij} the temperature-induced wavelength shift $\delta\lambda_{ij}$ is simply

$$\begin{aligned}\delta\lambda_{ij} &= \delta T \cdot \left(\frac{dn}{dT}\right)_{ij} \Big/ \left(\frac{dn}{d\lambda}\right)_{ij} \\ &= \delta T \cdot \left(\frac{d\lambda}{dT}\right)_{ij}\end{aligned} \tag{3-11}$$

where the sensitivities in Equations $\frac{dn}{d\lambda} = -\frac{\lambda}{n}\cdot\sum_k \frac{B_k\lambda_k^2}{\left(\lambda^2-\lambda_k^2\right)^2}$ (3-9 and $\frac{dn(\lambda,T_c)}{dT} = \frac{n^2-1}{2n}\left[D_0 + 2D_1\Delta T + 3D_2\Delta T^2 + \frac{E_0 + 2E_1\Delta T}{\lambda^2 - {\lambda_{TK}}^2}\right]$ (3-10 are substituted and evaluated for each pixel i,j, and $\delta T = T - T_c$. The index of refraction n_{ij} associated with a specific pixel is derived from Equation $n^2(\lambda) - 1 = \lambda^2\sum_{k=1}^{3}\frac{B_k}{\lambda^2-{\lambda_k}^2}$ (5-6. The new wavelength registration is simply

$$\lambda'_{ij} = \delta\lambda_{ij} + \lambda_{ij} \tag{3-12}$$

Note that unlike the nadir view of the atmosphere, limb measurements are also subject to a Doppler red-shift. The pixel wavelength assignments in the SDR are accurate in that they have been corrected for the red-shift during solar calibrations. The Earth view red-shift affects the comparison between measured and modeled Earth spectra, and should therefore be accommodated in any retrieval.

Sources of uncertainty

Errors in the band center wavelengths are a result of uncertainties in the wavelength trending predictions and inaccurate or inadequate models describing intra-orbital changes in pixel registration. The first of these is discussed in Section 5.2, which includes the description of wavelength registration algorithm. The second relates to the causes of and corrections for shifts presented in this section. Errors include inaccurate parameterization of the prism thermal sensitivity and additional thermal sensitivities, e.g. focal plane shifts.

OMPS/LP is instrumented with 2 thermistors on the surface of its prism. While this should provide an accurate measure of the prism temperature throughout an orbit, the internal temperature could differ due to the low heat transfer rates of fused silica. In these situations the actual temperature would lag the thermistor readings used in the corrections described above.

Corrections based on prism properties ignore shifts of the focal plane relative to the prism as a result of intra-orbital temperature changes. While there was some evidence from Thermal Vacuum testing for temperature-induced shifts beyond those related to the prism index of refraction, these shifts were quite small in comparison.

To conclude, there are scenarios where index of refraction changes do not fully describe observed intra-orbital shifts. It is unlikely that additional shifts could exceed 1 hundredth of a pixel, the approximate accuracy of the solar spectrum wavelength registration. Should the correction described here still prove inadequate, it is possible to derive empirical shift corrections based on the Fraunhofer lines observed in the Earth backscatter spectrum. While not as precise as registration based on the solar spectrum, the highly repeatable nature of wavelength shifts means a great deal of Earth-view data can be averaged to obtain a result.

3.2.2 Geo-location and solar angles

Table 3-2 Geo-location input/output list

Input	**Input Source**
Pixel sample table	Sensor upload table
Pixel pointing vectors (spacecraft frame)	Sensor calibration database
Measurement times	Level 1A
Image timing	Sensor upload table
Attitude & Ephemeris	Level 1A
Output	**Output Destination**
Solar zenith angles at pixel tangent points	SDR File
Satellite zenith angles at pixel tangent points	SDR File
Solar azimuth angles at pixel tangent points	SDR File
Satellite azimuth angles at pixel tangent points	SDR File
Pixel tangent point altitudes	SDR File
Latitude of pixel tangent point	SDR File
Longitude of pixel tangent point	SDR File

Geo-location ("Earth Location") and related Sun and Moon location algorithms supporting the OMPS Limb Profiler (LP) Earth View and Calibration algorithms have a broad common basis with analogous algorithms developed for the OMPS Nadir sensors. For all three OMPS sensors, key algorithms for Earth and celestial body location, including reference frame transformations, follow the approach developed by Hughes/Raytheon for NASA's EOS satellites and described in the Science Data Processing (SDP) Toolkit (TK) Geolocation ATBD (1995). [1] Elements specific to OMPS Limb Profiler geolocation will be explained in this section.

Detailed descriptions of SDP Toolkit general principles and specific functions can be found in chapter 6 of the SDP Toolkit User's Guide. [2] In particular, section 6.2.6 discusses the approach to ephemeris and attitude handling; section 6.2.7 describes time and date handling; and sections 6.3.3-6.3.6 describe celestial body location algorithms, Earth-centered coordinate reference frames and conversion algorithms between them.

The raw material of Earth location are the satellite ephemeris and attitude. For NPP, ephemeris and attitude are updated once per second, time-tagged and downlinked in CCSDS packets (APID 11). Collectively APID 11 packets are the "Spacecraft Diary" component of each Raw Data Record (RDR).

3.2.2.1 Time

OMPS geolocation references several time streams. The NPP spacecraft time tags ephemeris and attitude in UTC in binary CDS (CCSDS Day Segmented) format: The first 2 bytes are the number of days since midnight, 1 January 1958; the next 4 bytes are the number of milliseconds of the day; and the last 2 bytes are the number of microseconds beyond the last integral millisecond. These times are collected in arrays in the Level 1A file along with science data (which have their own time tags). The geolocation routine converts the integer components back into 8-byte binary SCD format, which are then converted to "spacecraft time" or "internal Toolkit time", a modified form of TAI time, double-precision seconds since the epoch at midnight, 1 January 1993 (usually designated "secTAI93" in the code). This is then converted to the standard Toolkit UTC string format, "ASCII UTC", the form expected by SDP Toolkit ephemeris and attitude handling routines, as well the Earth, Sun, and Moon location routines, reference frame transformations, solar and satellite zenith and azimuth routines, etc.

3.2.2.2 Ephemeris

The NPOESS/NPP General Instrument Interface Document (NGIID) [5] requires ephemeris data – time-tagged geocentric Cartesian position (X, Y, Z) and velocity (Vx, Vy, Vz) vectors -- to be delivered in the native GPS reference frame, the real-time Earth-Centered, Earth-Fixed (ECEF) frame, also known as Earth-Centered Rotating (ECR).

Ephemeris data must be converted from ECEF to ECI (the Earth-Centered Inertial frame, currently synonymous with the J2000 frame) to satisfy SDP Toolkit ephemeris-handling input requirements. This conversion – executed using SDPTK Coordinate System Conversion (CSC) Tools described in Chapter 6 of the ref. [1] -- consists of 4 rotations (see ref. [1], section 6.2.3 and ref. [2], pg. 6-410):

(a) The Z-axis is corrected for polar wander from the "geographic" poles (locations on the Earth's physical surface) to the mean rotational poles of date;

(b) The X-Y plane is rotated about the new Z-axis so that the X basis vector rotates from 0° latitude, 0° longitude to the Vernal Equinox at the J2000 epoch (noon on 1 January 2000 = 1.5 January 2000 TT, Terrestrial Time; N.B.: The definition in ref. [1], sec. 6.2.1, is a typo); Julian days begin at noon);

(c) The Z-axis is transformed from of-date nutated to the mean nutated position at the J2000 epoch;

(d) The Z-axis is transformed from of-date precessed to the mean rotation axis at the J2000 epoch.

Correction for polar wander uses a frequently updated file from the USNO ("utcpole.dat"); the same file is used to correct small time scale variations due to nonuniform rotation (UT1-UTC); ref. [1], section 6.2, for further discussion of time-related geolocation corrections.

3.2.2.3 Attitude

Attitude determination involves more onboard input and processing than ephemeris handling. Real-time inertial guidance data are combined with real-time star tracker data; the latter are interpreted by means of star charts that must be transformed by the NPP flight software from J2000 to of-date star positions. (NPP Table 58, containing coefficients for this transformation, is regularly updated and uploaded.) The result is then transformed back to J2000 quaternions (to satisfy another NGIID [5] requirement) and written to APID 11 packets, with the scalar component following the 3 vector components (in contrast to the SDPTK quaternion format, in which the scalar component comes first).

A related requirement is that the NPP spacecraft Z-axis point (ideally) toward *geodetic* nadir. Attitude quaternions represent the orientation of basis vectors "fixed" to the spacecraft with respect to the J2000 inertial frame, determined on orbit by the spacecraft Attitude Determination and Control System (ADCS). The ideal geodetic [orbital] frame is referenced in various ways by the ADCS, but not by the attitude quaternions. However, the ideal spacecraft orientation must be considered when attitude is simulated for test data, or when actual attitude is evaluated post launch (e.g., by Cal/Val Teams).

SDP Toolkit attitude-handling routines expect input in the form of Euler "error" angles with respect to a *geocentric* orbital frame (standard for EOS satellites). These Euler angles are strictly mathematical constructs in this context; they are not output products and play no part in error reporting or correction.

Basis vectors to construct a geocentric orbital frame are modeled by the geolocation routine using the position and velocity ephemeris vectors after they are transformed from ECEF to ECI (see Section 3.2.2.2 above).

The Z unit vector is along the radius vector but pointed *toward* the center of the Earth:

$\mathbf{z} = -\mathbf{R}/R$

The X unit vector lies in the plane determined by the velocity (**V**) and **z**, in the general direction of **V**; the Y unit vector thus lies along the cross-product of **z** and **V** (in the anti-sun direction):

$\mathbf{y} = \mathbf{z} \times \mathbf{V} / |\mathbf{z} \times \mathbf{V}|$

The X unit vector is then the cross-product of unit vectors **y** and **z**:

x = **y**x**z**

This completes a right-handed Cartesian basis for an instantaneous geocentric orbital frame in J2000 ECI coordinates. It is not the actual or ideal spacecraft orientation, but a geocentric frame from which Euler "error" angles may be calculated as rotations to the actual spacecraft coordinate frame. These Euler angles are the attitude input in SDPTK form.

The first step is to construct a rotation matrix from components of the geocentric orbital frame basis vectors **x**, **y**, and **z** arranged as column vectors in a 3x3 matrix, $\mathbf{T}_{\mathbf{orb}\text{->eci}}$:

$$\mathbf{T}_{\mathbf{orb}\text{->eci}} = \begin{vmatrix} x1 & y1 & z1 \\ x2 & y2 & z2 \\ x3 & y3 & z3 \end{vmatrix}$$

where **x** = (x1, x2, x3), **y** = (y1, y2, y3), and **z** = (z1, z2, z3).

On the other hand, each Spacecraft Diary attitude quatenion represents the orientation of the spacecraft coordinate frame relative to J2000 ECI [see ref. 4, Table 3-123, pg. 398] at a given time . The attitude quaternion is can be converted to a rotation matrix [see ref. 3 (Wertz), section 12.1]. If the quaternion is represented as (Qs, Q1, Q2, Q3), where Qs is the scalar component and Q1, Q2, and Q3 together comprise the vector component, the ECI-to-spacecraft rotation matrix can be written

$$\mathbf{T}_{\mathbf{eci}\text{->sc}} = \begin{vmatrix} A11 & A12 & A13 \\ A21 & A22 & A23 \\ A31 & A32 & A33 \end{vmatrix}$$

where

$A11 = Q1^2 - Q2^2 - Q3^2 + Qs^2$, $A12 = 2*(Q1*Q2 + Q3*Qs)$, $A13 = 2*(Q1*Q3 - Q2*Qs)$

$A21 = 2*(Q1*Q2 - Q3*Qs)$, $A22 = -Q1^2 + Q2^2 - Q3^2 + Qs^2$, $A23 = 2*(Q2*Q3 + Q1*Qs)$

$A31 = 2*(Q1*Q3 + Q2*Qs)$, $A32 = 2*(Q2*Q3 - Q1*Qs)$, $A22 = -Q1^2 - Q2^2 + Q3^2 + Qs^2$.

The matrix product, $\mathbf{T}_{\mathbf{eci}\text{->sc}} \bullet \mathbf{T}_{\mathbf{orb}\text{->eci}} = \mathbf{T}_{\mathbf{orb}\text{->sc}}$, yields a rotation matrix (denoted by Bij below) from the geocentric orbital frame to the spacecraft frame, from which we can extract Euler angles

equivalent to the geocentric-orbital-to-spacecraft frame rotation[s]. If the Euler angles are applied in 3-1-2 order (yaw-roll-pitch, or rotations about the z, x, and y axes), then

$$\text{yaw} = -\arctan(B21/B22)$$

$$\text{roll} = \arcsin(B23)$$

$$\text{pitch} = -\arctan(B13/B33)$$

(see Wertz, section 12.1, p. 419). These represent spacecraft attitude in the required SDP Toolkit input form and reference frame; along with the ephemeris and time prepared as described above, geolocation and sun angle calculation can formally begin using the algorithms described in references [1] and [2].

3.2.2.4 Calculating Earth, Sun, and Moon location for OMPS/LP

The OMPS LP sensor, unlike the nadir sensors, determines the tangent point above the WGS 84 ellipsoid along the line of sight from the sensor using unit look vectors from each illuminated macropixel in the focal plane. Macropixels are pixels (or, in principle, aggregates of pixels) on the CCD selected by the appropriate sample table [q.v.] to collect radiances over the required range of wavelengths and altitudes, including smear and stray light data, while complying with downlink bandwidth restrictions. The following describes the major steps in the limb geolocation process.

Calculating the subsatellite point (the intersection of the geodetic nadir vector with the WGS 84 ellipsoid representation of the Earth) requires only ECI position input and WGS 84 Earth model parameters. See analysis in ref. [1], pp 7-13*ff*. This is not directly relevant to calculation of tangent points above the Earth's limb, but only to the ground track of the satellite.

The geocentric Solar Right Ascension (RA) and Declination (Dec) in the ECI frame are derived directly from the calculation of the Earth-Sun vector using a basic SDP Toolkit astronomy routine that depends only on the ASCII UTC date and time. The length of this vector is the instantaneous Earth-Sun distance. The Solar RA is the arc tangent of $Y_{earth\text{-}sun} / X_{earth\text{-}sun}$. The Solar Dec is arc tangent of

$Z_{earth\text{-}sun} / R_{earth\text{-}sun}$, where $R_{earth\text{-}sun}$ is the Earth-Sun distance.

The Sun-Earth vector is then normalized by its length and transformed to the orbital reference frame, and the Solar Beta angle is calculated: It is $-\arctan(Y_{orbit\text{-}sun} / \text{SQRT}(X^2_{orbit\text{-}sun} + Z^2_{orbit\text{-}sun}))$.

Then the normalized ECI Sun-Earth vector is transformed to the spacecraft frame, where Solar Azimuth and Elevation angles are calculated.

$$\text{Solar Elevation} = \arcsin(Z_{SC\text{-}sun});$$

$$\text{Solar Azimuth} = \arctan(Y_{SC\text{-}sun} / X_{SC\text{-}sun}).$$

To prepare for the calculation of solar zenith and azimuth angles at the tangent-point, the normalized ECI solar ray is transformed to the ECEF (ECR) frame – the inverse of the transformation applied to the original ECEF ephemeris data, as described in Section 3.2.2.2 above.

Stored look vectors in the spacecraft coordinate frame are retrieved for preselected sensor [macro]pixels. They are then rotated into the ECI frame and combined with ephemeris and attitude to calculate geodetic latitude and longitude at the tangent point, in addition to the tangent point height. The SDP Toolkit routine used for this (PGS_CSC_grazingray) calculates the point where the line of sight that is the continuation of the focal plane look vector is tangent to an ellipsoidal envelope referred to the WGS 84 ellipsoid.

In cases where the tangent height is positive, limb retrieval is possible; solar and satellite zenith and azimuth angles are calculated at the tangent point in these cases. The scheme for defining these angles used by the SDP Toolkit is followed in the LP Geo component of the LP Earth View SDR; namely, the reference vectors originate at the tangent point and point toward the object of interest (the Sun or the satellite, respectively). Zenith angles are measured between the vector and the normal to the reference ellipsoid; azimuth angles are measured eastward of north.

Because the LP Geolocation algorithm does not use the output of this routine when the line of sight penetrates the ellipsoid, the algorithm in such cases calls the function used by the OMPS nadir geolocation algorithms and extracts solar and satellite angles at the pierce point instead. Thus, it may be possible to interpret the radiance at such pixels even when a limb retrieval is not possible. In these cases, reference vectors for solar and satellite angles originate at the pierce point and point toward the object of interest (the Sun or the satellite, respectively).

If a check for moonlight through one or more of OMPS LP's 3 slits is ordered, the algorithm generates unit vectors based on preselected center and corner azimuth and elevation angles. These vectors are passed to the Toolkit function PGS_CBP_body_infov, with the Moon indicated as the target. That function tests the proximity of the vector to the Moon to vectors associated with the perimeter of each slit (with the knowledge that the "center" of the slit provides one internal point for comparison); a flag is set if there is a likelihood of moonlight through the slit.

If ordered, the OMPS LP Geo-location algorithm then checks for the possibility of a solar eclipse. This is accomplished in several stages. First, the measurement time is analyzed and compared with dates in a prepared lookup table (LUT). If the year of the measurement more than a year later than the year in the table entry, try the next entry; if the year of the entry is more than a year later than the year of the measurement, then there is no possibility of a solar eclipse.

If the date is still in the running, the penumbra time boundaries in the LUT are compared with the measurement time. If the latter falls within those boundaries, then the the algorithm checks the solar zenith angle; if daylight is still possible, the algorithm allows for a check at a specific FOV; but this option is currently skipped for LP, because it is difficult to determine where the influence of umbra and particularly penumbra might occur along the line of sight; thus, the swath is flagged for LP if there is penumbra somewhere during the daylight portion of the orbit.

The last test is whether the spacecraft, as indicated by its latitude and longitude (spacecraft, *not* tangent point), falls within the region known of influence of the South Atlantic Anomaly (SAA). This area is subject to variable levels of bombardment by charged particles trapped in the Earth's magnetic field, which can significantly impact satellite-borne instruments. The LP Geolocation algorithm tests (and flags) whether the satellite latitude and longitude fall within one of three concentric threshold regions, corresponding (rather arbitrarily) to 0-5%, 5-40%, and >40% of the

maximum mean SAA particle hit rate [as outlined in ref. 6 and discussed by ref. 7]. In the first case, bit 0 of the high byte of the 16-bit swath-level quality flag is set; in the second case, bit 1 (only) is set; in the third case, both bits are set.

See appendices for more detailed illustrations and explanations of the reference frames and mathematical methods referred to in this geolocation discussion.

3.2.2.5 Field of view smear

The absolute measurement times used in geolocating the spacecraft and the sensor field of view are from the midpoint of the 18.4 sec. exposure interval. In fact this midpoint differs between long and short integrations by a few milliseconds. This difference is ignored since it results in a negligible error in any of the important geolocation parameters. From the standpoint of product retrievals, the most important parameter is the altitude of the tangent points. The latitude and longitude of each tangent point is used for collocating with external data, but the sensitivity to these parameters is weak. Illumination and viewing conditions (solar/satellite zenith and azimuth angles) at the tangent point are also computed at the exposure midpoint. While the solar zenith angle can change by more than 2° over the exposure time, the variation is quite linear except near the sub-solar point.

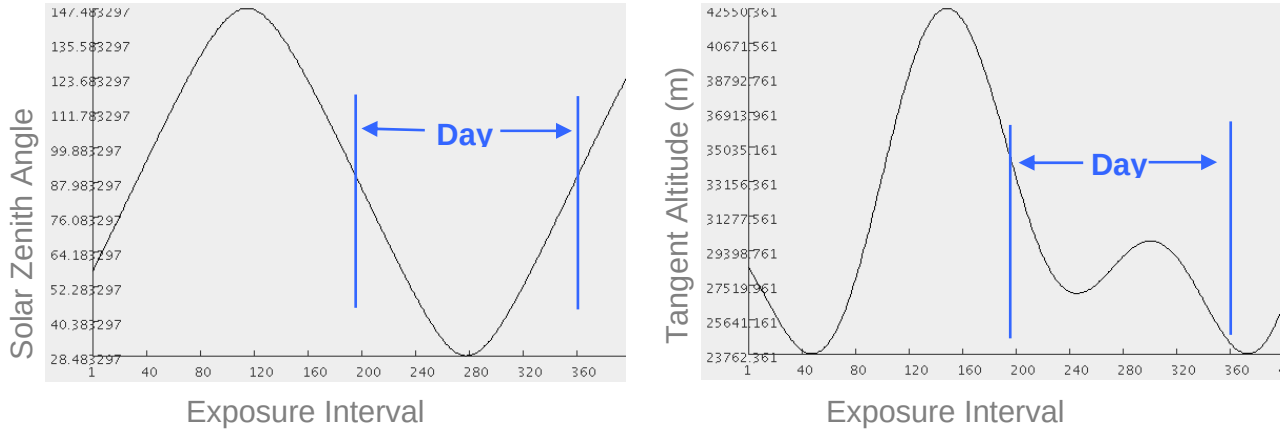

Figure 3-2 Tangent point solar zenith angle (left) and altitude (right) for a mid-detector pixel in a simulated 1 May orbit. Each exposure interval is 18.4 sec. The altitude scale covers ~20 km.

Changes in the tangent point altitude over the exposure period should be considered in any product retrieval. Figure 3-2 contains plots of a tangent point solar zenith angle and altitude for a single pixel as a function of time in the orbit. The maximum altitude change over an exposure interval is approximately 220 m. Since this distance is small compared to the IFOV (see Figure 1-17), the effective FOV broadens by less than 1 percent.

3.2.3 Detector Corrections

Table 3-3 Detector corrections input/output list

Input	**Input Source**
Uncorrected signals, C_{ADC}	Level 1A
Smear signals, C^{m}_{smear}	Level 1A
Dark currents, D_{imag} , D_{stor}	Calibration history file
Pixel binning, N_{bin}	Sensor upload table
Image timing, t_{int}, t_{stor}, N_{coadd}	Sensor upload table
Output	**Output Destination**
Corrected signals, C_{photon}	Internal

Detector corrections in the SDR algorithm reverse signal errors introduced in the on-board signal collection and processing. The 4 primary errors are dark signals, readout smear, gain non-linearity, and zero signal offsets. These error terms are described in Equations

$$C_{ADC}(i,j) = C_{Bias}(i,j) + g \cdot \ell(Q_{tot}) \cdot Q_{tot}(i,j)$$

(3-1

$$Q_{tot}(i,j) = Q_{photon}(i,j) + Q_{smear}(i,j) + Q_{dark}(i,j)$$

(3-2. Combining these two equations and converting from electrons to counts via the factor g yields the following expression for the portion of the final signal resulting from photoelectrons.

$$C_{photon}(i,j) = \frac{C_{ADC}(i,j) - C_{Bias}(i,j)}{\ell} \quad - \quad C_{smear}(i,j) \quad - \quad C_{dark}(i,j) \tag{3-13}$$

As indicated by this equation, the first correction applied to raw ADC signals is for detector non-linearity. This correction is applied by the flight software prior to pixel co-addition for the reasons discussed in Section 1.5. Values for C_{smear} and C_{dark} in Equation

$$C_{photon}(i,j) = \frac{C_{ADC}(i,j) - C_{Bias}(i,j)}{\ell} \quad - \quad C_{smear}(i,j) \quad - \quad C_{dark}(i,j)$$

(3-13 are assumed to be linearity-corrected. Since the smear signals are a part of the detector read-out, these signals are linearity-corrected in the flight software as well. Dark signals C_{dark} are derived from calibration data processing (see Section 5.6), where a non-linearity correction has been applied.

Values for C_{Bias} and C_{smear} are derived from C^{m}_{smear} , the measured smear signal. Since smear pixels are typically binned in the flight software to improve statistics, the following equality holds for all smear signals.

$$C_{smear}(i,j) + C_{bias}(i,j) \quad = \quad \frac{C^{m}_{smear}(j)}{N_{bin}} \tag{3-14}$$

A pixel collects dark signals primarily from the image and storage regions of the CCD. The dark signals from each region are corrected separately because the time spent in the storage region is a constant, whereas the frame integration time t_{int} can vary. An example of this is the short and long integration times used for LP Earth-view measurements.

$$C_{dark}(i,j) \;=\; N_{coadd}\left[D_{imag}(i,j)\cdot t_{\text{int}} + \sum_{1}^{i} D_{stor}(i,j)\cdot t_{stor}\right] \tag{3-15}$$

In this equation t_{stor} = 897μs is the time a pixel spends in each row of the storage region. Substituting into Equation $C_{photon}(i,j) = \frac{C_{ADC}(i,j) - C_{Bias}(i,j)}{\ell} \;-\; C_{smear}(i,j) \;-\; C_{dark}(i,j)$ (3-13 and eliminating the linearity correction $1/\ell$ yields an expression for a corrected signal.

$$C_{photon}(i,j) \;=\; C_{ADC}(i,j) \;-\; \frac{C^{m}_{smear}(j)}{N_{bin}} \;- N_{coadd}\left[D_{imag}(i,j)\cdot t_{\text{int}} + \sum_{1}^{i} D_{stor}(i,j)\cdot t_{stor}\right] \tag{3-16}$$

Sources of uncertainty

Signal errors have both random and systematic origins. Random errors are treated as noise, and are estimated in the next section. The subtraction of smear and dark signals described by Equation $C_{photon}(i,j) \;=\; C_{ADC}(i,j) \;-\; \frac{C^{m}_{smear}(j)}{N_{bin}} \;- N_{coadd}\left[D_{imag}(i,j)\cdot t_{\text{int}} + \sum_{1}^{i} D_{stor}(i,j)\cdot t_{stor}\right]$ (3-16 each has an associated systematic uncertainty.

The measured signal C^{m}_{smear} is derived from overclocks during the parallel transfer of the CCD readout, and is an estimate of the true smear signal. The two are equal only when the Earth scene does not vary between the beginning and end of a frame. For short integration times of 40 ms scene variation is very small and the smear estimation is quite accurate. Scene variation is larger for the 1.25 sec. long integration, and as a consequence so are the errors. If the overall signal change of a scene is 10%, the error in the smear amount for pixels at the top or bottom of a column can be as much as 10%. Errors are less towards the middle of a column. Since smear is approximately 0.1% of the total signal, the maximum smear error in this example is 0.01%.

Systematic errors in the dark current correction arise from a difference between the dark signals present in the Earth view measurements and the dedicated dark measurements used for characterization. One cause is detector temperature differences between the two. The detector temperature is maintained within 0.2 ºC all the time, which can result in a peak-to-peak variation of approximately 4% of thermally generated electrons in a pixel well. Dark signals during long integrations are of order 10 counts, meaning these temperature variations only rarely result in a 1 count error.

A larger source of error is occasional transients resulting from charged particle hits in the detector. Some transients can fill the pixel well, those most deposit less charge. The dedicated dark measurements are obtained outside the South Atlantic Anomaly, where most transients occur, and it is easier to screen the dedicated dark measurements for transients than it is the Earth view measurements. As a consequence transients are a significant but rare error in the dark corrections.

3.2.4 Noise Calculation

Table 3-4 Noise calculation input/output list

Input	**Input Source**
Uncorrected signals, C_{ADC}	Level 1A
Smear signals, C_{smear}	Level 1A
System noise, σ_{sys}	Operational Parameter File
Electrons to counts conversion, g	Operational Parameter File
Smear pixel binning, N_{bin}	Sensor upload table
Image timing, N_{coadd}	Sensor upload table
Output	**Output Destination**
Signal-to-noise ratio, SNR(i,j)	SDR File

Calculation of noise on the sensor signal proceeds via error propagation on Equation

$$C_{photon}(i,j) = C_{ADC}(i,j) - \frac{C^{m}_{smear}(j)}{N_{bin}} - N_{coadd}\left[D_{imag}(i,j)\cdot t_{\text{int}} + \sum_{1}^{i} D_{stor}(i,j)\cdot t_{stor}\right] \quad \text{(3-16.}$$

Other sources of uncertainty, such as corrections applied for stray light and linearity are not considered at this time. A term for signal processing noise σ_{sys} has been added to account for all noise sources in the sensor electronic chain. This term was determined empirically to be 30 electrons for OMPS/LP.

$$\sigma^{2}_{photon}(i,j) = \sigma^{2}_{ADC}(i,j) + \frac{\sigma^{2}_{smear}(j)}{N^{2}_{bin}} + N^{2}_{coadd}\cdot\sigma^{2}_{dark}(i,j) + N_{coadd}\cdot\sigma^{2}_{sys} \quad \text{(3-17)}$$

The dark currents will be characterized in orbit over a much longer time period than the individual integration times during Earth view measurements. And since the detector temperature is very stable, no error is expected due to dark current drifts. For these reasons the dark current uncertainty term is dropped. Noise due to charge transfer inefficiency (CTI) is also ignored.

With the exception of the σ_{sys} term, all remaining uncertainties in Equation

$$\sigma^{2}_{photon}(i,j) = \sigma^{2}_{ADC}(i,j) + \frac{\sigma^{2}_{smear}(j)}{N^{2}_{bin}} + N^{2}_{coadd}\cdot\sigma^{2}_{dark}(i,j) + N_{coadd}\cdot\sigma^{2}_{sys} \quad \text{(3-17}$$

result from electron counting statistics, often referred to as shot noise. These terms Poisson statistics apply and $\sigma^2 = Q$, where Q is the number of electrons. After substitution the resulting uncertainty in electrons is

$$\sigma_{photon} = \left[Q_{tot} + \frac{Q_{smear}}{N^{2}_{bin}} + N_{coadd}\sigma^{2}_{sys}\right]^{1/2} \quad \text{(3-18)}$$

where

$$Q_{tot} = \frac{C_{ADC} - C_{bias}}{g} \qquad Q_{smear} = \frac{C_{smear}}{g}$$

The signal to noise ratio is computed using corrected signals.

$$SNR = \frac{C_{ideal}}{g \cdot \sigma_{photon}} \tag{3-19}$$

3.2.5 Straylight Correction

$$Q_{photon}(i,j) = \iint_{IN} L(\lambda,\Omega)\, S_{i,j}(\lambda,\Omega)\, \tau(\lambda,\Omega)\, QE_{i,j}(\lambda)\, d\lambda\, d\Omega \quad + \iint_{OUT} L(\lambda,\Omega)\, S_{i,j}(\lambda,\Omega)\, \tau(\lambda,\Omega)\, QE_{i,j}(\lambda)\, d\lambda\, d\Omega$$
$$= Q_{ideal} + Q_{stray}$$

As described in Equation (3-4, the number of photons collected in a detector pixel can be separated into those collected in a narrow wavelength and angle region centered on the pixel and those originating out-of-field and out-of-band. This division simplifies the calibration process significantly because the stray light portion of the signal is usually small. The OMPS/LP stray light signals are small, but not negligible.

Straylight within OMPS/LP is primarily caused by photon scatter in the optics chain that slightly alters the ray paths. Since the sensor optics are designed to disperse light rays in altitude and wavelength, stray light tends to originate from altitudes and wavelengths where signals are greatest, and most affects regions where signals are the weakest. Photons enter the OMPS/LP sensor through separate low and high gain apertures for each slit, which complicates the situation due to stray light cross-talk between the two apertures. The imaging of all three slits onto a single focal plane further complicates the stray light situation. Inter-aperture sources of stray light tend to be small compared to intra-aperture sources, except at the extreme ends of the spectral range. There is no physical barrier between the far UV end of one slit and the IR end of an adjacent slit.

Stray light was recognized as an issue from the beginning of the OMPS/LP program, and its mitigation was an integral part of the sensor design. The instrument test program included a thorough characterization of sensor stray light properties culminating in the creation of two calibration databases, one for optical point spread functions (PSFs) and one for ghosts. The response across the focal plane is a sum of the 2-dimensional PSF and ghost response. These databases are the basis for all stray light corrections in the SDR algorithm. The characterization proceeded by measuring the response in all detector pixels to pseudo-point light sources Each aperture was independently offered 293, 350, 430, 495, 700, and 1000nm light at the bottom, middle, and top of each slit. Thus there are a total of 18 response images for each aperture, 108 images overall. A schematic showing these 108 point sources is found in Figure 1-24. An

assumption is made that a PSF and ghost map can be derived for a point source centered at any pixel in the active optics region of the detector by interpolating between the 108 maps.

In order to mitigate the risk associated with unknown stray light performance in flight, two distinct correction algorithms were developed. Each approach is presented in separate subsections. A major complication of OMPS/LP stray light correction is that only signals from portions of the focal plane image are downlinked due to data rate constraints. This means that an incomplete set of stray light sources in orbit are made available to the correction routines. The two algorithms differ in how they deal with the lack of information.

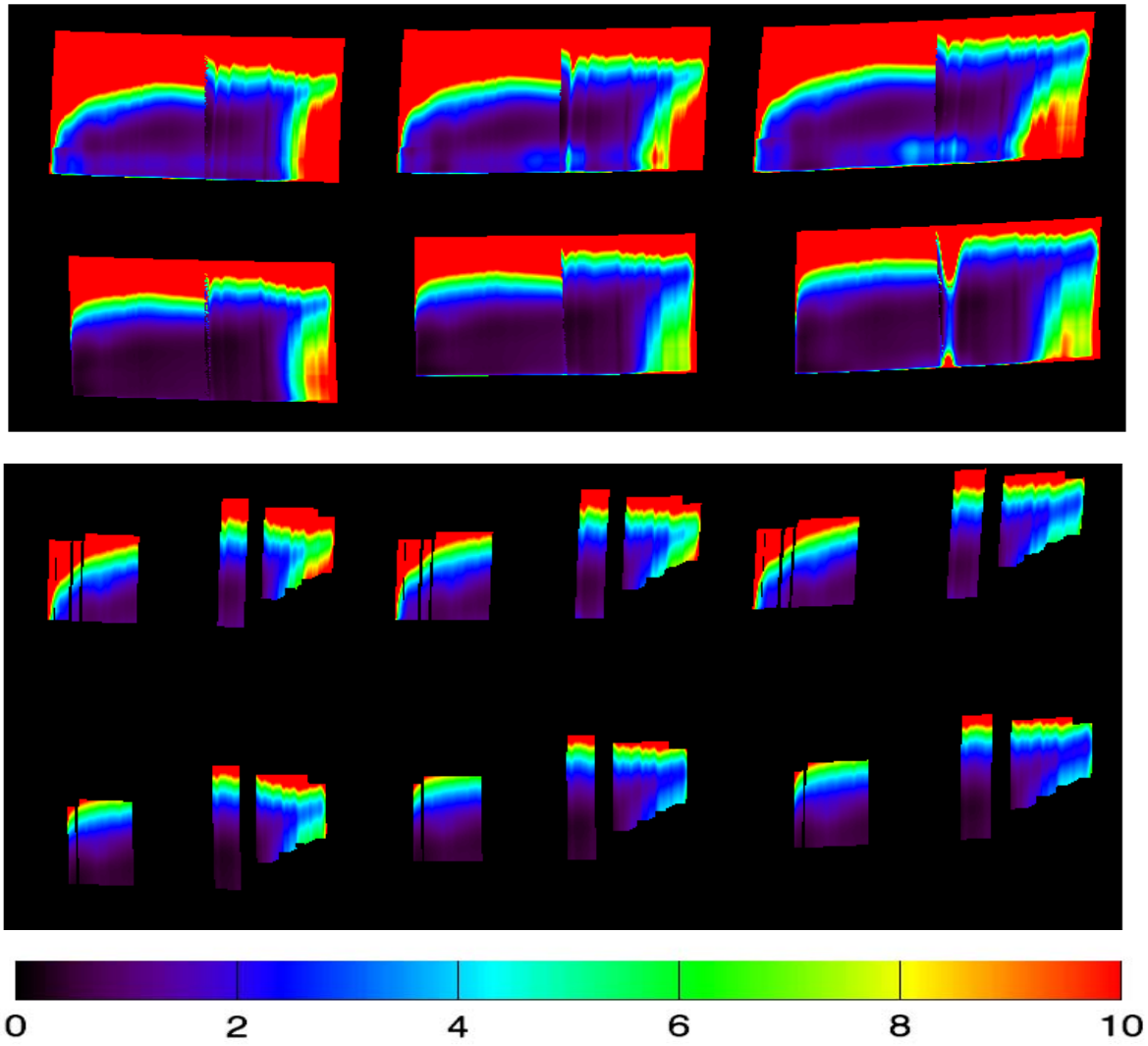

Figure 3-3 Simulated stray light percentages for a high latitude 575 DU ozone profile. The second panel shows the same results, but sampled according to pixels that are relevant to ozone retrievals.

3.2.5.1 Stray light technique A

Table 3-5 Stray light correction (A) input/output list

Input	**Input Source**
Uncorrected signals, C_{photon} Stray light Jacobian, f Pixel sample table	internal Static calibration file Sensor upload table
Output	**Output Destination**
Stray signals, C_{stray}	internal

This correction algorithm relies on the assumption that a 2-dimensional PSF can be estimated for every pixel in the image region of the detector. The resulting function $PSF(i_s,j_s,i_t,j_t)$ is discrete over the full detector. An similar function $GHOST(i_s,j_s,i_t,j_t)$ describes residual non-PSF structures seen in the test data. The total signal in pixel i_t,j_t is the sum of the near-band, near-field signal and the stray light signal.

$$\begin{aligned} C_{photon}(i_t,j_t) &= C_{in}(i_t,j_t) + C_{stray}(i_t,j_t) \\ &= C_{in}(i_t,j_t) + \sum_{i_s}\sum_{j_s} C_{in}(i_s,j_s)\cdot PSF(i_s,j_s,i_t,j_t) \\ &\quad + \sum_{i_s}\sum_{j_s} C_{in}(i_s,j_s)\cdot GHOST(i_s,j_s,i_t,j_t) \end{aligned} \tag{3-20}$$

Such large 4-dimensional matrices are impractical for an operational correction algorithm. Instead, the focal plane can be divided into a much smaller number of source regions k that capture the limb radiance variability necessary to describe stray light. The stray light portion of Equation (3-20 is rewritten as a sum over measured source signals in regions k. Since fractional stray light levels are relatively small, replacing source signals C_{in} with C_{photon} results in minimal error.

$$C_{stray}(i_t,j_t) = \sum_k C_{photon}(i_s,j_s)_k \cdot f(i_t,j_t,k) \tag{3-21}$$

Here $f(i_t,j_t,k)$ is a Jacobian matrix describing the total stray light sensitivity between one or more source signals in each region k and target pixels i_t,j_t. The 536 chosen source regions are shown in Figure 3-4 along with the current pixel sampling. The algorithm currently requires that at least 1 pixel i_s,j_s be sampled and downlinked for each region.

Each Jacobian element $f(i_t,j_t,k)$ is simply the ratio of the stray light generated by all pixels i_s,j_s within source region k to the signal in sampled source pixels i_s,j_s.

$$f(i_t, j_t, k) = \frac{\sum_{ij} C_{sim}(i_s, j_s)_k \cdot PSF(i_t, j_t, k)}{\sum_{ij} C_{sim}(i_s, j_s)_{meas}} \quad (3\text{-}22)$$

$$f(i_t, j_t, k) = \frac{\sum_{ij} C_{sim}(i_s, j_s)_k \cdot PSF(i_t, j_t, k)}{\sum_{ij} C_{sim}(i_s, j_s)_{meas}}$$

The sum in the numerator of Equation (3-22 is over an entire source region k, whereas the denominator sum is only over the measured source pixels i_s,j_s within region k. The matrix is computed using a full stray light simulation using a typical Earth scene and atmosphere. Since the sampled pixel(s) can change during on-orbit operations, the Jacobian must be regenerated whenever the selected pixels change.

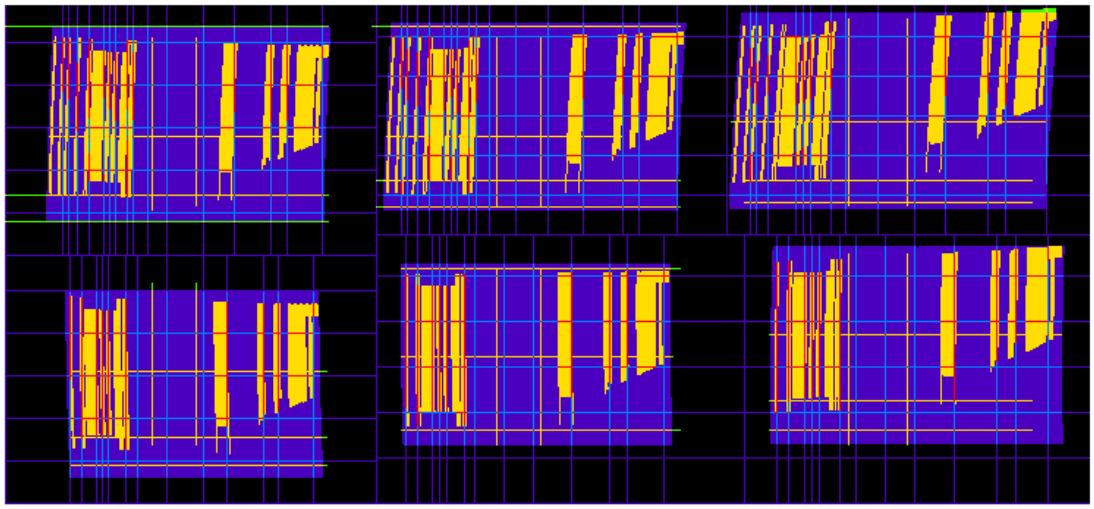

Figure 3-4 LP focal plane image containing the sampled pixels in yellow and stray light source regions outlined in light blue grid lines. Stray light sources do not extend outside the blue shaded regions that indicate the directly illuminated regions of the detector.

Sources of uncertainty

If the PSFs and ghosts are known exactly and all possible sources are well measured, little error remains in the stray light correction. The two correction error sources are therefore the pre-launch characterization accuracy and incomplete sampling of stray light sources from the measured radiance image.

Pre-launch characterization uncertainties, estimated in Section 1.7.8, are 5-10% in the UV, ~1% in the VIS and NIR, and as much as 100% at 1000 nm. To estimate residual errors in the stray light correction algorithm, the correction described above was applied to simulated stray light data.

Limb radiances were generated for various low, mid, and high latitude ozone profiles and surface reflectances of 0% and 100%. A full stray light simulation for each radiance image was computed using PSFs and ghosts as described in Section 1.7.8. Each image was then sampled in a manner similar to that shown in Figure 3-4. This means that only radiances from selected pixels were retained and the rest discarded. This selection mimics the pixel sampling by the flight software that sends fewer than 20% of the available pixels to the ground. Signals from the remaining pixels are used to evaluate Equation (3-21 and obtain an estimate of the stray light signal in those pixels.

$$C_{stray}(i_t, j_t) = \sum_k C_{photon}(i_s, j_s)_k \cdot f(i_t, j_t, k)$$

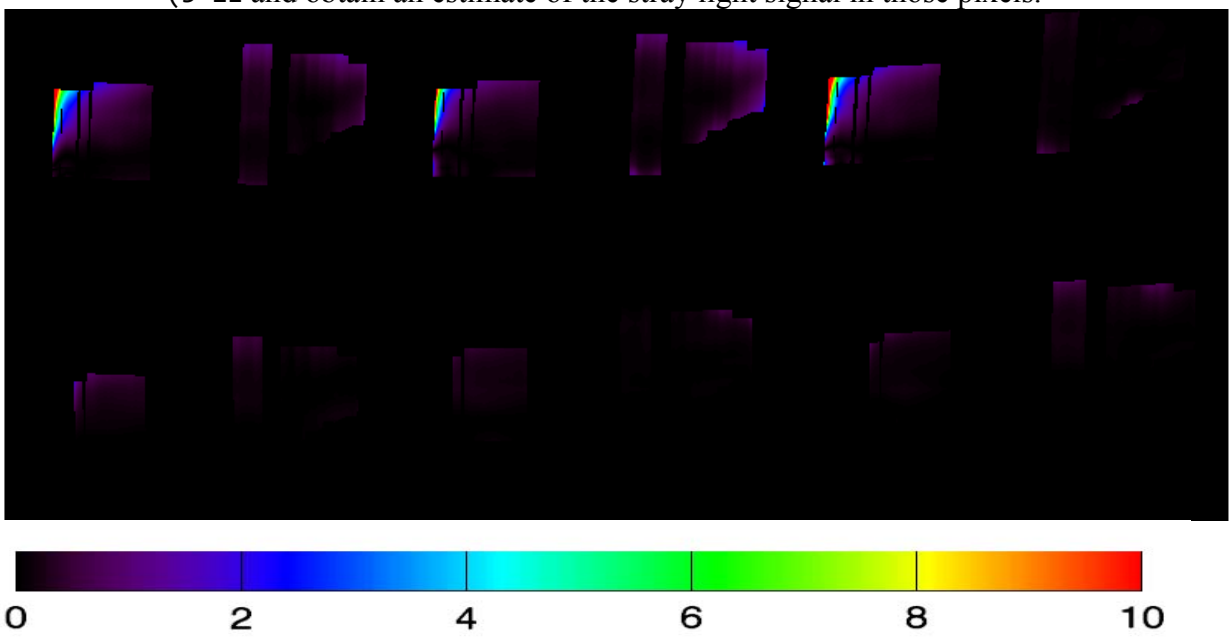

Figure 3-5 LP focal plane image indicating residual stray light correction errors (in percent). The simulated scene corresponds to that shown in Figure 3-3.

A comparison between the estimated stray light and the modeled amount yields the stray light correction error in each pixel. Errors are large when the Earth scene conditions underlying a modeled image differ significantly from the scene used to create the Jacobian correction *f*. In the example shown in Figure 3-5 *f* was generated from a simulated low latitude atmosphere with low ozone amount. The scene reflectance was 0%. The modeled scene, like that shown in Figure 3-3, was high latitude, had high ozone, and 100% surface reflectance. Even for this stressing case, most residual stray light errors are less than 1%. The exception is low gain IR signals at high altitudes. This is consistent with the large, complicated PSF at 1000 nm.

3.2.5.2 Straylight mitigation technique B

The straylight mitigation technique B, like technique A, is basically a deconvolution process:

$$R(i_0, j_0) = \sum_{all\ pixels} r(i,j) \cdot F(i - i_0, j - j_0) \quad (3\text{-}23)$$

where $r(i,j)$ is the true limb radiance of a pixel located at CCD pixel row i and column j. $R(i_0,j_0)$ is the measurement made by the pixel (i_0,j_0). To first order, Equation

$$R(i_0, j_0) = \sum_{all\ pixels} r(i,j) \cdot F(i - i_0, j - j_0) \quad (3\text{-}23)$$

can be rewritten as:

$$R(i_0, j_0) = r_{core}(i_0, j_0) + \sum_{\substack{all\ pixels \\ not\ in\ core}} r_{core}(i,j) \cdot F(i - i_0, j - j_0) \quad (3\text{-}24)$$

where $r_{core}(i,j)$ refers to the limb radiance integrated over the central part of the PSF for pixel (i,j). In

$$R(i_0, j_0) = r_{core}(i_0, j_0) + \sum_{\substack{all\ pixels \\ not\ in\ core}} r_{core}(i,j) \cdot F(i - i_0, j - j_0)$$

matrix form, Equation (3-24) can be written as:

$$[R] = [1 + \varepsilon].[r] \quad (3\text{-}25)$$

where ε denotes a matrix which is typically small compared to the identity matrix, and the square bracket identifies a matrix.

To invert Equation $[R] = [1 + \varepsilon].[r]$ (3-25), a Taylor expansion is used:

$$[r] = [1 - \varepsilon].[R] + HOT \quad 3\text{-}26)$$

where HOT refers to high order terms. An estimate of HOT can be evaluated from residuals. Upon reconvolution:

$$HOT \approx [R] - [1 + \varepsilon].[r^*], with\ [r^*] = [1 - \varepsilon].[R] \quad 3\text{-}27)$$

Equations $[r] = [1 - \varepsilon].[R] + HOT$ 3-26) and $HOT \approx [R] - [1 + \varepsilon].[r^*], with\ [r^*] = [1 - \varepsilon].[R]$ 3-27) are solved by iterations up to convergence. For each of the 740x340 CCD pixels (i_0,j_0), the summation must be carried over all the PSF elements affecting pixel (i_0,j_0). Consequently, solving Equations $[r] = [1 - \varepsilon].[R] + HOT$ 3-26) and $HOT \approx [R] - [1 + \varepsilon].[r^*], with\ [r^*] = [1 - \varepsilon].[R]$ 3-27) can be prohibitively CPU intensive. The approach used in the convolution process of the instrument model described in Appendix B is also used here to speed up the computations.

Since only a small fraction of the CCD pixels can be downloaded, a large fraction (85-90%) of the data matrix R has unknown values. However, these values can be estimated from the measured ones using a linear regression technique performed along CCD pixel rows:

$$Log\left[\frac{I(\lambda)}{S(\lambda)\cdot\lambda^4}\right] = -\sigma(\lambda)\cdot CD(TH) + polyn(\lambda) \quad (3\text{-}28)$$

where $I(\lambda)$ is the limb radiance measured on CCD pixel associated with wavelength λ, $S(\lambda)$ represents the solar input (evaluated by convolving a theoretical solar spectrum with the spectral slit function), $\sigma(\lambda)$ is the ozone cross section and $polyn(\lambda)$ is a closure polynomial. The effective ozone column density $CD(TH)$ is then used to estimate the signal value on all missing pixels.

3.2.6 Conversion to Radiances

Table 3-6 Radiance conversion input/output list

Input	**Input Source**
Corrected signals, C^r_{ideal}	internal
Image timing, N_{coadd}, t_{int}	Sensor upload table
Pixel sample table	Sensor upload table
Output	**Output Destination**
Radiances, L	SDR file

The fundamental radiometric calibrations for each pixel are described by Equation $L_{ij} = \frac{k^r_{ij}\cdot C^r_{ideal}(i,j)}{t_{\text{int}}}$ (3-8).

The signals C^r_{ideal} have had all corrections applied, including those for time-dependent sensor changes. One small complication is that the total signal obtained for one pixel is the sum of multiple frames of data, each with integration time t_{int}. This sum, referred to as co-addition, takes place in the OMPS electronics. The conversion to radiances, when data are co-added, is more properly written

$$L_{ij} = \frac{k^r_{ij}\cdot C^r_{ideal}(i,j)}{N_{coadd}\cdot t_{\text{int}}} \quad 3\text{-}29)$$

The constants k^r_{ij} were derived from pre-launch radiometric calibrations. A description of these constants is included in Section 1.7.5. Radiances are reported in units of $W\cdot cm^{-3}\cdot sr^{-1}$.

Sources of uncertainty

The conversion from ideal counts to radiances adds no uncertainty to that already present in C^r_{ideal}. The calibration coefficients k^r_{ij} have inherent uncertainties, and these are described in Section 1.7.5. The total sensitivity of pixel i,j is a product of the pixel quantum efficiency and the optical throughput of the sensor at the band center and look angle of that pixel. The two become decoupled

as the band center or pixel pointing drifts so that k^r_{ij} also drifts ever so slightly. Where sensitivities vary little, such as in the middle of the spatial or spectral range, these drift errors are negligible. Errors are larger at the slit edges and at filter edges, areas where pixel use is avoided.

3.2.7 Collocation of External Data

Table 3-7 Data collocation input/output list

Input	**Input Source**
Latitude of pixel tangent points	internal
Longitude of pixel tangent points	internal
Measurement times	Level 1A file
Pixel sample table	Sensor upload table
Temperature & pressure profiles	External files from NCEP
Output	**Output Destination**
Geographically and temporally interpolated temperature and altitude on a pressure scale	internal

In keeping with the philosophy that the SDR product contains all information necessary to perform retrievals, external data are ingested into the SDR algorithm, resampled to correspond to OMPS/LP measurements, and written to the output product. As of this writing, only vertical temperature and pressure profiles are brought in from external sources. These profiles are post facto data provided daily by the NCEP Global Forecast System, and have the following characteristics:

- 21 pressure levels: 1000, 850, 700, 500, 400, 300, 250, 200, 150, 100, 70, 50, 40, 30, 20, 15, 10, 5, 2, 1, 0.4 mb
- Geometric altitude (above sea level) at each pressure level
- Temperature at each pressure level
- Provided at 1°x 1° grid spacing in latitude and longitude
- Provided at 0000, 0600, 1200, and 1800 UTC

The collocation algorithm proceeds by selecting the two bracketing times of NCEP data for each measurement time. Then in each of these data sets, the temperature and altitude arrays are computed via bilinear interpolation at the latitude and longitude the limb measurement. Because every pixel has a slightly different tangent point altitude, the geolocation of every pixel is different. The latitude and longitude used in the interpolation is the mean location for pixels pointing at 25 km tangent point altitude. Following the geographic interpolation, the profiles are interpolated linearly in time to the measurement time.

3.2.8 Pixel Flagging

The primary purpose of pixel flagging is to identify those pixels whose reported signals may be suspect due to a variety of factors. A separate flag is used for each criterion, so it is possible to determine the source of the problem. These flags fall into two categories, static and dynamic. Static flags describe a persistent condition associated with a pixel, such as excessive dark current or

random telegraph behavior. These flags determined from off-line analysis of large statistical samples or long data records. Dynamic flags identify problems specific to an individual measurement, such as a transient or saturated signal.

3.2.8.1 Saturated pixel detection

Table 3-8 Saturated pixel detection input/output list

Input	Input Source
Uncorrected signals, C_{ADC} Saturation threshold, C_{thresh}	Level 1A file Operational parameter file
Output	Output Destination
Saturated pixel flag	SDR file

A saturated pixel is one where the addition of photons into the pixel results in no additional signal as seen in the raw data. This highly non-linear behavior results because 1) the pixel potential well contains at or near the maximum number of electrons, or 2) the input signal to the ADC exceeds the maximum bits available. These two are often referred to as detector saturation and ADC saturation. For OMPS/LP the electronic gain was set so that ADC saturation occurs at a lower signal level than detector saturation. In principle, then, a pixel is saturated when it has a signal of $2^{14} = 16384$, where 14 is the number of output bits of the ADC. The true situation is complicated by frame co-addition in the flight electronics.

The OMPS flight electronics typically adds together (co-adds) signals from multiple sequential detector readouts (frames) for each pixel in order to increase the dynamic range and therefore the signal to noise ratio of a measurement. Co-addition is a digital process and occurs after conversion to counts in the ADC. Therefore the final signal for an image can be much greater than 16384 counts. The co-addition register has 24 bits and will never overflow under nominal measurement conditions.

The intent of the algorithm is to flag pixels in an image for which at least one frame was saturated. Because of scene variability, it is possible to have saturated frames and still measure a signal for the co-added image less than N_{coadd}*16384. Rather, a threshold is used such that the saturation flag is set for an image when

$$\frac{C_{ADC}}{N_{coadd}} > 16384 - C_{thresh}$$

The value of C_{thresh} is established empirically based on natural scene variability, and is currently set to 20 counts.

3.2.8.2 Transient pixel detection

Table 3-9 Transient pixel detection input/output list

Input	**Input Source**
Uncorrected signals, C_{ADC}	Level 1A file
Sample window, N_{imag} Flagging interval, K_{Δ}	Operational parameter file Operational parameter file
Output	**Output Destination**
Transient pixel flag	SDR file

Energetic protons and electrons will deposit charge into one or more pixel wells as they pass through the detector. The charge from the most energetic particles can far exceed photoelectron charges, especially if the image time is short. This algorithm attempts to flag such transient pixels by comparing single pixel signals in a time series. The time window chosen for the data sample depends upon natural image variability.

The algorithm filter makes some simplifying assumptions about the data to be combed for transients. Specifically, it assumes that the transients in question represent anomalously high values in a distribution that is crudely symmetric about a median value for the chosen window. The algorithm masks anomalously low values below a threshold that is one of the input parameters, and computes the standard deviation σ of the remaining data. Pixels are flagged if the following condition exists

$$C_{ADC} > K_{\Delta} \cdot \sigma$$

unless they constitute a series of 2 or more consecutive transients. In that case anomalously high values are more likely a result of true scene variation. The standard deviation is recomputed after removing flagged pixels and the process repeated. Iterations cease when no more outliers are detected. The value of K_{Δ} is determined empirically, and is always chosen large enough that the iterations converge.

3.2.9 Two-dimensional gridding

Due to the sensor spectral/spatial smile, measured radiances are reported on a non-uniform, non-orthogonal altitude-wavelength frame. At this level, the data is labeled as “un-gridded”. Many retrieval algorithms, and the gain consolidation described below, require radiances to be on a uniform Tangent-Height (TH) versus wavelength (λ) grid. Thus, un-gridded radiance data must be interpolated and remapped onto a Cartesian [λ,TH] grid. This remapping involves a linear combination of radiances, the effect of which can be minimized if the associated weighting factors are stored and used in the construction of the retrieval vectors.

The re-gridding algorithm uses a bilinear interpolation routine, as illustrated in Figure 3-6. In spatial dimension, the grid is setup at 1 km interval, whereas in the spectral dimension, the grid depends on the available CCD pixels. The Cartesian grid radiance data I(λ,TH) is computed as a weighted sum over the four pixels n surrounding the [λ,TH] grid point:

$$I(\lambda,TH) = \sum_{n=4\ pixels} weight(n).data(n) \tag{3-30}$$

where weight(n) and data(n) are respectively the bilinear weight factors and the measured data on individual pixels n. Similarly, the variance is evaluated as:

$$var(\lambda,TH)^2 = \sum_{n=4\ pixels} weight(n)^2 .\sigma(n)^2 \tag{3-31}$$

where σ(n) represents the measurement uncertainty on pixel n (which include shot noise, read noise and quantization noise).

This two-dimensional re-gridding is applied independently for each of the four gains and each of the three slits.

3.2.10 Gain consolidation

As described in Section 1.5, the large dynamic range of limb radiances across the field-of-view is accommodated by the sensor splitting the incoming radiance across four gain levels. The EDR code requires combining the information contained in the four gain images into a unique set of radiance profiles. The gain consolidation process uses the two-dimensional Cartesian gridded radiances described above, weighting each of the four contributions according to (1) the Signal-to-Noise Ratio (SNR) and (2) the level of saturation for each CCD pixel involved in the gridding process. Basically, the lower portion of the radiance profile primarily uses the short-integration / small-aperture combination (unsaturated) while the upper portion uses the long-integration / large-aperture combination (higher SNR).

Once all the measurements for each slit are projected onto the same grid, the four gain images are consolidated into a single radiance profile I*(λ,TH):

$$I^*(\lambda,TH) = \sum_{4\ gains} [I_{gain}(\square]\lambda,TH).weight_{gain}(\lambda,TH) \tag{3-32}$$

where the summation is performed over the available images (narrow/wide aperture, short/long integration times), only for non-saturated pixels. The parameter $weight_{gain}$ is proportional to the data SNR at (λ,TH) for each image. The variance on the Cartesian point [λ,TH] is evaluated in two parts:

$$var^*(\lambda,TH)^2 = \sum_{4\ gains} [var_{gain}(\square]\lambda,TH)^2.weight_{gain}(\lambda,TH)^2 +$$

$$\sum_{4\ gains} \left[I_{gain}(\square)\lambda, TH(\square) - I^{*}(\lambda, TH) \right]^2 . weight_{gain}(\lambda, TH)^2 \tag{3-33}$$

where the second summation represents the error being made in the consolidation process. This term accounts for radiance biases across gain, such as residual straylight. Figure 3-7 shows a typical example of merging the four-gain images to construct the radiance profile for a given slit. In general, transition from one gain image to another will occur at higher altitudes for high radiance scenes such as over bright clouds. For a given scene, the gain transition typically occurs at different altitudes for each wavelength, which may result in a slight modulation of the retrieved ozone profile.

Once gridded onto a Cartesian grid and gain-consolidated, the radiance dataset is labeled "gridded" and stored as such in the SDR output file.

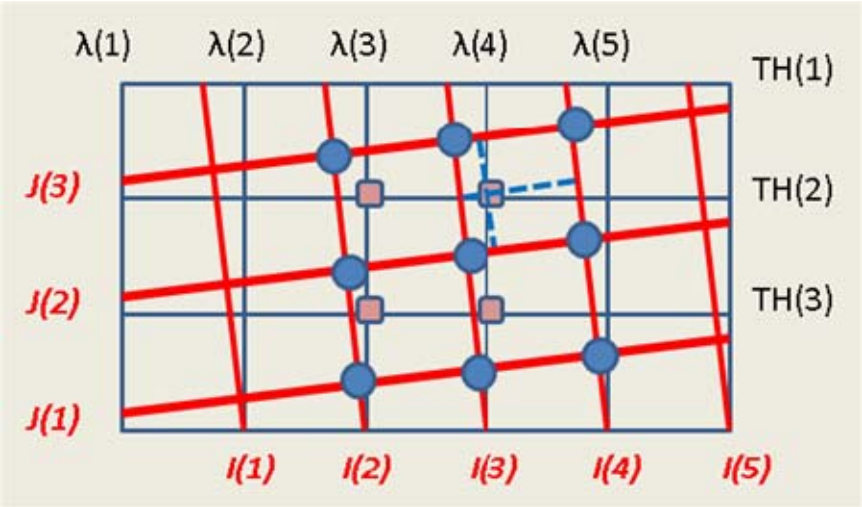

Figure 3-6 Bilinear interpolation. Blue circles represent CCD pixel center points. Red lines correspond to CCD pixel rows and columns. Blue lines represent the uniform Cartesian grid at wavelength λ and tangent height TH

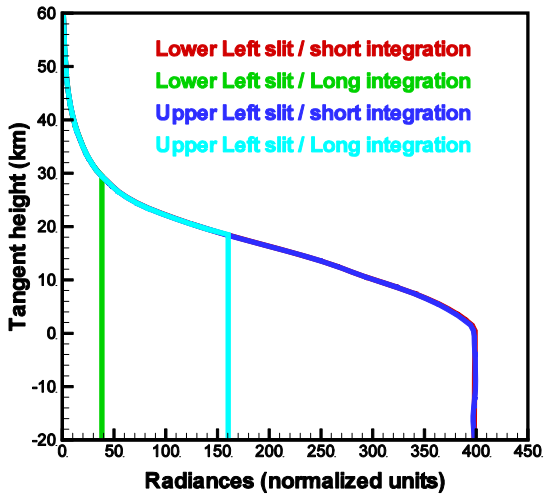

Figure 3-7 Gain consolidation process. The 4 gains (small/large apertures, short/long integration times) are combined into a unique profile. Saturated pixels are discarded.

4 CALIBRATION SENSOR DATA RECORD (SDR) ALGORITHM

4.1 In-flight calibrations – physical basis

Backscatter ultraviolet (BUV) instruments measure the response to solar irradiance by deploying a ground aluminum diffuser plate to reflect sunlight into the instrument. The calibration concept for the OMPS Limb Profiler sensor follows closely that of TOMS and SBUV/2. The three-diffuser system aboard TOMS [*Jaross, et al., 1998*] reduces the exposure and degradation of the diffuser used for the solar measurements and allows calibration through comparison of signals reflected off diffusers with different rates of exposure.

An identical concept is employed on OMPS, but only two diffusers are used because mechanical design differences obviate the need for the third diffuser. The transmissive diffusers, designated Working and Reference, are arranged in a rotating plane in front of the entrance apertures so that a given diffuser can be moved into view on demand. When a diffuser is commanded in front of one of the slits, the remaining two are automatically blocked. To calibrate OMPS, the Reference diffuser is exposed every 6 months for a solar measurement sequence (3 slits), and the Working diffuser is exposed every week. The Working diffuser is the primary sensor calibration diffuser. Periodic comparisons with Reference diffuser solar measurements are used to detect changes in the Working diffuser.

Knowledge of wavelength registration is established on-orbit using the solar Fraunhofer spectrum as a fixed reference. The registration is maintained through regular solar measurements. The initial wavelength scale, referred to as the baseline spectral registration, requires careful analysis to arrive at accurate band center values. The approach to routine monitoring is less exacting since spectral shifts are measured relative to the baseline. The SDR wavelength registration is primarily designed to conduct routine monitoring.

The OMPS/LP sensor also employs a red Light-emitting Diode (LED) directly in front of the detector. Light from the LED passes through no optics before reaching the detector window. It is intended for aliveness testing and detector linearity measurement, and is not suitable for radiometric monitoring.

Pixel dark currents are measured during the Earth eclipse portion of the orbit. The purpose of these daily measurements is to track long term drifts in the dark response and step changes caused by radiation damage.

4.1.1 Radiometric calibration

Conceptually, the calibration of measured Earth radiance and solar irradiance may be considered separately. But the purpose of solar measurements is to maintain calibration of Earth radiances rather than measure irradiance. With the BUV technique it is not possible to distinguish between solar flux changes and sensor response changes.

$$L_{ij} = \frac{k_{ij}^{r} \cdot C_{ideal}^{r}(i,j)}{t_{\text{int}}}$$

Measurements of Earth radiance can only be described by Equation (3-8 if sensor optical throughput and solar irradiance remain constant. The ideal radiance signal is related to the measured signal through the following:

$$C_{ideal}^{r}(i,j,t) = C_{meas}^{r}(i,j,t)\,\frac{F_{ij}(0)\cdot \tau QE_{ij}(0)}{F_{ij}(t)\cdot \tau QE_{ij}(t)} \tag{4-1}$$

where

C^{r}_{ideal} = Earth radiance signal for pixel *i,j* after correction for sensor degradation or solar irradiance change

C^{r}_{meas} = Earth radiance signal for pixel *i,j*, corrected for sensor electronics effects

F_{ij} = true solar irradiance over the band pass and field of view of pixel *i,j*

τQE_{ij} = total sensor response at pixel *i,j*, the product of optical throughput and detector quantum efficiency

In these equations, $t = 0$ corresponds to the time of a baseline solar irradiance measurement. The change since the baseline in measured solar irradiance, F_{meas}, can be written as the product of changes in true solar irradiance, sensor response, and solar diffuser transmittance *T*.

$$\frac{F_{meas}(i,j,t)}{F_{meas}(i,j,0)} = \frac{F_{ij}(t)}{F_{ij}(0)}\cdot\frac{\tau QE_{ij}(t)}{\tau QE_{ij}(0)}\cdot\frac{T_{ij}(t)}{T_{ij}(0)} \tag{4-2}$$

Substitution into Equation 4.1 yields the following estimate for ideal Earth radiance signals at time *t* in terms of measurable quantities.

$$\begin{aligned} C_{ideal}^{r}(i,j,t) &= C_{meas}^{r}(i,j,t)\cdot\frac{F_{meas}(i,j,0)}{F_{meas}(i,j,t)}\cdot\frac{T_{ij}(0)}{T_{ij}(t)} \\ &= \kappa(i,j,t)\cdot C_{meas}^{r}(i,j,t) \end{aligned} \tag{4-3}$$

where κ is a factor near 1 for a well-behaved sensor. It is worth noting that an accurate absolute measure of solar irradiance and diffuser transmittance is unnecessary. Only changes since a baseline measurement are used. Solar irradiance and diffuser measurements are described in Sections 5.3 and 5.5, respectively.

4.1.2 Aspects of radiometric calibration related to spectral registration

As discussed in the previous subsection, a comparison between a current solar measurement and the baseline solar measurement is the basis for correcting measured Earth signals for long-term changes in sensor response and solar irradiance. Radiometric response changes can have any number of causes, including a shift in the spectral registration of a given pixel.

The in-flight calibration approach expressed by Equation

$$C^r_{ideal}(i,j,t) = C^r_{meas}(i,j,t) \cdot \frac{F_{meas}(i,j,0)}{F_{meas}(i,j,t)} \cdot \frac{T_{ij}(0)}{T_{ij}(t)} = \kappa(i,j,t) \cdot C^r_{meas}(i,j,t) \quad \text{4-3}$$

accounts for all sensor changes, including a spectral registration shift, provided sensor changes are the same for Earth and solar measurements. Experience with spectroscopic data from instruments such as GOME and OMI suggests that correcting radiances for spectral shifts is an inaccurate method for dealing with the problem. Rather, the radiances should be reported at the wavelength scale at which they were measured. To accomplish this, a correction γ_{ij} must be applied in Equation

$$C^r_{ideal}(i,j,t) = C^r_{meas}(i,j,t) \cdot \frac{F_{meas}(i,j,0)}{F_{meas}(i,j,t)} \cdot \frac{T_{ij}(0)}{T_{ij}(t)} = \kappa(i,j,t) \cdot C^r_{meas}(i,j,t) \quad \text{4-3}$$

to place the numerator and denominator on the same spectral scale.

The expected spectral shifts for OMPS/LP are small, much less than 1 pixel. For functions such as diffuser transmission that vary slowly with wavelength, the correction is small enough that it can be ignored. But a correction for solar measurements must be implemented due to the highly variable Fraunhofer absorption present in the solar spectrum. Details of this adjustment are discussed with the radiometric trending approach in Section 5.3.

It bears restating that the spectral shift correction prior to radiometric trending ensures that the shift is not "calibrated out" of the reported radiances. A measured solar spectrum is also reported in the SDR output product should a retrieval require the use of a sun-normalized Earth radiance spectrum. Because OMPS LP solar measurements are used to correct measured radiances back to equivalent $t = 0$ values, only the baseline solar measurement is reported. Since the spectral scale differs between time t and $t = 0$, the baseline solar measurement must be placed on the same spectral scale as radiance measurements. This is accomplished by reporting the quantity $F_{meas}(i,j,0) / \gamma_{ij}$.

4.1.3 Diffuser degradation

The multi-diffuser approach to diffuser monitoring relies upon the fundamental assumption that all changes in diffuser reflectance at the sensor wavelengths are a result of solar exposure. Observations [*Jaross et al. 1998*] of diffuser reflectance changes in TOMS, SBUV, and SBUV/2 demonstrate that in the absence of UV radiation, there is no evidence for significant degradation of either a stowed or exposed diffuser surface. In a clean OMPS environment, the diffuser degradation rate should therefore be a function of the solar measurement rate. Analysis of previous instruments show some

evidence that initial rates depend on the diffuser material [*Hilsenrath, 1994*], but in the long term, UV exposure and contaminants appear to predominate [*Hall, 1994*].

In the multi-diffuser approach to calibration employed by OMPS a quantity derived from solar calibrations is the Working to Reference signal ratio

$$r = \frac{W}{R} \tag{4-4}$$

where W and R represent the mean signals from the Working and Reference diffusers, respectively, normalized to their baseline (initial post-launch) calibration values. A small fractional change in the value of this ratio, due to the degradation of either surface or a relative goniometric error, is then written as

$$\frac{dr}{r} = \frac{dW}{W} - \frac{dR}{R} \tag{4-5}$$

The assumption of exposure-dependent diffuser degradation implies

$$\begin{aligned} W &= f(t_W) \\ R &= f(t_R) \end{aligned} \tag{4-6}$$

where *f(t)* is an arbitrary function of the exposure time *t*. The differential changes are then

$$\begin{aligned} \frac{dW}{W} &= \frac{f'(t_W)}{f(t_W)} dt_W \\ \frac{dR}{R} &= \frac{f'(t_R)}{f(t_R)} dt_R \end{aligned} \tag{4-7}$$

Since a solar measurement sequence is the same for Working and Reference surfaces, exposure times can be rewritten in terms of the number of Working and Reference measurements, n_W and n_R.

$$\frac{t_R}{t_W} = \frac{dt_R}{dt_W} = \frac{n_R}{n_W} \tag{4-8}$$

Results from TOMS Cover diffusers indicate that degradation is truly an exponential process. In the specific case where *f(t)* is an exponential, the change in the working surface reflectance as a function of the change in the quantity *r* is

$$\frac{dW}{W} = \frac{n_W}{n_W - n_R}\frac{dr}{r} \tag{4-9}$$

For situations where the number of Working measurements far exceeds the number of Reference measurements, as with OMPS, the Working change is nearly equal to the change in the ratio of diffuser surfaces. An uncertainty ε_r in the value of r translates via Equation $\frac{dW}{W} = \frac{n_W}{n_W - n_R}\frac{dr}{r}$ (4-9 to an uncertainty in W.

$$\frac{\varepsilon_W}{W} = \frac{n_W}{n_W - n_R}\frac{\varepsilon_r}{r} \tag{4-10}$$

It is the uncertainty in W that ultimately drives the long-term sensor calibration uncertainty.The value of ε_r is actually a time-dependent quantity because, assuming Gaussian statistics, it varies roughly as $\varepsilon_r = \sigma_r/\sqrt{n_R}$. The current operations schedule calls for Reference measurements every 6 months. Thus there will be 2 values of r derived per year. Each data point will have a variance σ^2_r associated with it. The algorithm applies a linear regression to these data of the form

$$\ln(r) = b \cdot t_W \tag{4-11}$$

to determine the Working degradation at a time t_W. An uncertainty ε_W can be estimated (see *Bevington*, for instance) at an arbitrary time t using σ_r and the proposed exposure schedule.

$$\frac{\varepsilon_W}{W} = \frac{n_W}{n_W - n_R}\sigma_b \cdot t \qquad \sigma_b^2 = \frac{1}{\Delta}\sum^{n_r}\frac{1}{\sigma_r^2}$$
$$\Delta = \sum_i^{n_r}\frac{1}{\sigma_r^2}\sum_i^{n_r}\frac{t_W^2}{\sigma_r^2} - \left(\sum_i^{n_r}\frac{t_W}{\sigma_r^2}\right)^2 \tag{4-12}$$

It is worth noting that the uncertainty ε_W does not depend on the rate b of degradation. Each value σ_r depends upon several factors, but is predominantly related to the errors in the goniometric corrections applied to the solar data. The time-dependent Working diffuser transmission can be written

$$\frac{T(t,\lambda)}{T(0,\lambda)} = 1 - \left(\frac{dW}{W}\right) \tag{4-13}$$

So long as the relationship

$$\frac{\varepsilon_W}{W} > \frac{dW}{W} \tag{4-14}$$

holds, there are no plans to apply a correction for Working diffuser degradation.

4.2 Calibration data processing

The goal of calibration signal processing is to obtain for each sampled pixel, an appropriately corrected signal suitable for archiving. The corrections applied are ones generally not subject to interpretation or reevaluation. The Calibration SDR produced is the input to subsequent data analysis, discussed in the next section. Corrections applied in the Calibration SDR algorithm include all appropriate electronic signal corrections plus a conversion of solar signals to solar irradiances. Note that solar irradiances reported in the Calibration SDR are not calibrated. The basic data flow for this portion of the algorithm is shown in Figure 4-1. Detailed discussions of the processes, corresponding to the individual elements in Figure 4-1, are contained in subsections that follow.

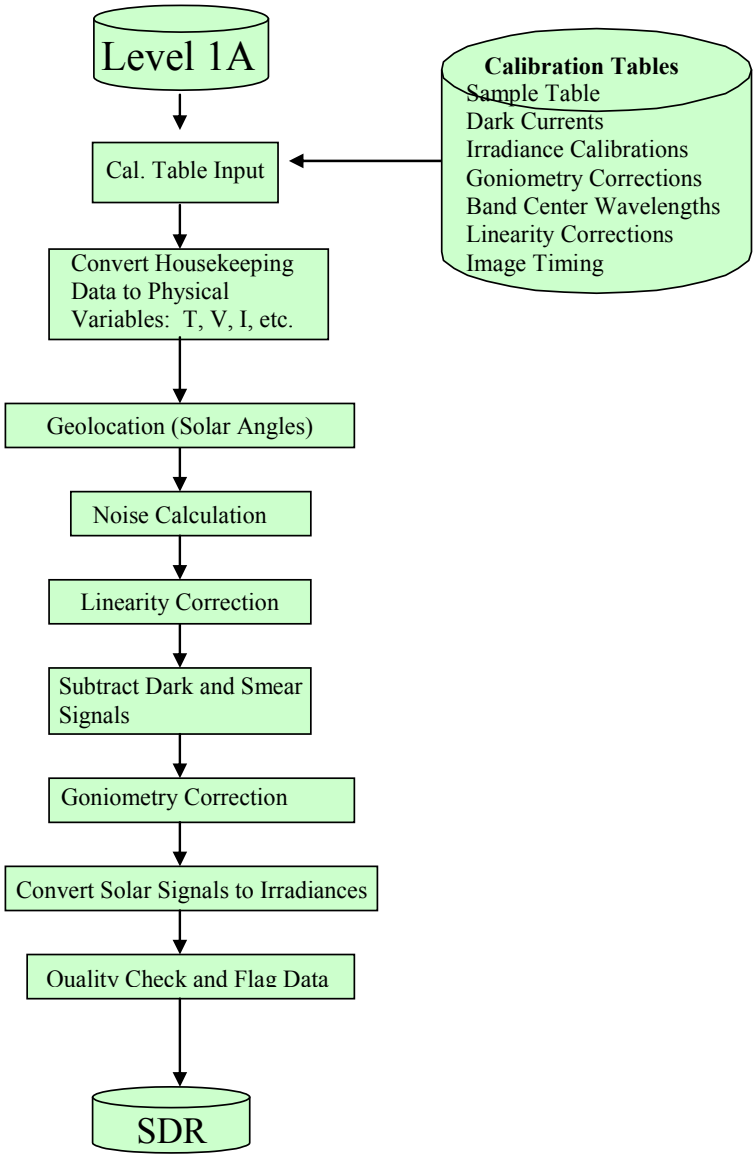

Figure 4-1 Schematic showing the Calibration SDR generation process.

4.2.1 Geo-location

Two basic types of geolocation are required for calibration data, spacecraft-centered solar angles and sub-satellite latitude and longitude. The solar angles are needed for computing goniometric corrections (see Section 4.2.4). Knowledge of the spacecraft position is needed for South Atlantic Anomaly flagging and helps when verifying the timing of calibration measurements. Section 3.2.2

contains a complete discussion of the OMPS/LP geolocation calculations. Calculations pertaining specifically to calibration data are not repeated here for the sake of brevity and clarity.

4.2.2 Detector corrections

Table 4-1 Detector corrections input/output list

Input	**Input Source**
Uncorrected signals, C_{ADC}	Level 1A
Smear signals, C^{m}_{smear}	Level 1A
Dark currents, D_{imag} , D_{stor}	Calibration history file
Smear pixel binning, N_{bin}	Sensor upload table
Image timing, t_{int}, t_{stor}, N_{coadd}	Sensor upload table
Non-linearity characterization, ℓ	Calibration history file
Output	**Output Destination**
Corrected signals, C_{photon}	Internal

Detector corrections are intended to reverse errors introduced in the in-flight signal collection and processing. These errors include dark signals, readout smear, gain non-linearity, and zero signal offsets. Corrections for these errors are as described in Section 3.2.3 for Earth signals. A major difference is that, unlike Earth signals, no in-flight correction is performed for non-linearity. The corrections applied in the SDR algorithm for the 4 main data types are given in Table 4-2.

Table 4-2 Detector corrections application map

	Earth	***Solar***	***Lamp***	***Dark***
Dark	X	X		
Smear	X	X		X
Linearity		X		X

As with Earth signals, the zero signal offset (a.k.a. Bias) in calibration data is corrected via the smear correction. This correction amounts to a subtraction of bias and smear signals, which are estimated in Equation (3-14.

$$C_{smear}(i,j) + C_{bias}(i,j) \quad = \quad \frac{C^{m}_{smear}(j)}{N_{bin}}$$

Corrections for dark signals amount to subtraction of a signal estimated in Equation (3-15.

$$C_{dark}(i,j) \quad = \quad N_{coadd}\left[D_{imag}(i,j)\cdot t_{\text{int}} + \sum_{1}^{i} D_{stor}(i,j)\cdot t_{stor} \right]$$

Dedicated dark measurements occurring during Earth eclipse yield the dark currents D_{imag} and D_{stor}. The same dark currents are used for Earth and calibration corrections.

Linearity corrections are performed in the SDR code in the same manner they are applied in the flight electronics. Since the SDR code works in units of counts rather than electrons, Equation $C_{ADC}(i,j) = C_{Bias}(i,j) + g \cdot \ell(Q_{tot}) \cdot Q_{tot}(i,j)$ (3-1 can be rearranged to yield a corrected count level C_{tot} in terms of the measured counts C_{ADC}.

$$C_{tot} = \frac{C_{ADC} - C_{bias}}{\ell} \tag{4-15}$$

The function ℓ describes deviations from linear response for signal levels above the bias level. For signals at or below the bias level the gain of the system is defined to be linear. The non-linearity is converted to a discrete correction for each input C_{ADC} (see discussion in Section 5.4). The correct value C_{corr} is simply a lookup table with 2^{14} entries, where 14 is the number of bits in the ADC.

$$\begin{aligned} C_{corr} &= C_{ADC} & C_{ADC} &\le C_{bias} \\ C_{corr} &= \frac{C_{ADC}}{\ell(C_{ADC} - C_{bias})} & C_{ADC} &> C_{bias} \end{aligned} \tag{4-16}$$

4.2.3 Noise calculation

The noise calculation for calibration data proceeds exactly the same as for Earth data. The formulation described in Section 3.2.4 applies equally to calibration data.

4.2.4 Goniometric corrections

Table 4-3 Goniometric corrections input/output list

Input	**Input Source**
Goniometry characterization, $G_{ij}(\alpha,\beta)$	Sensor calibration database
Spacecraft-centered solar elevation angle, α	internal
Spacecraft-centered solar azimuth angle, β	internal
Output	**Output Destination**
Pixel goniometric corrections, $1/G_{ij}$	internal

Irradiance sensitivity varies as the angle of solar illumination on the flight diffuser changes. This sensitivity variation, know as irradiance goniometry G, was characterized prior to launch in terms of spacecraft-centered solar angles α and β. G is a dimensionless quantity with a value of 1 at the angle at which radiometric calibrations were performed prior to launch. Variations in G between pixels is weak, with approximately linear dependence in the spectral dimension. There is no evidence of diffuser features in OMPS/LP irradiance measurements. Following detector corrections,

a correction $1/G_{ij}$ is applied to C^i_{photon}. The values G_{ij}, have been characterized by the following polynomial and provided in the pre-launch database.

$$G_{ij} = \eta_{ij0} + \eta_{ij1}\cdot\beta + \eta_{ij2}\cdot\beta^2 + \eta_{ij3}\cdot\beta^3 + \eta_{ij4}\cdot\alpha + \eta_{ij5}\cdot\alpha\beta + \eta_{ij6}\cdot\alpha\beta^2 + \eta_{ij7}\cdot\alpha\beta^3 + \eta_{ij8}\cdot\alpha^2 + \eta_{ij9}\cdot\alpha^2\beta + \eta_{ij10}\cdot\alpha^2\beta^2 + \eta_{ij11}\cdot\alpha^3 + \eta_{ij12}\cdot\alpha^3\beta + \eta_{ij13}\cdot\alpha^4 \quad (4\text{-}17)$$

The SDR algorithm uses the values η_{ijk} to independently derive a correction factor for every pixel i,j.

Sources of uncertainty

The single largest source of error in monitoring the radiometric calibration comes from the goniometric corrections. Inaccurate measures of the solar irradiance signals increase the uncertainty of radiometric response and diffuser reflectance change estimates (see Sections 4.1.1 and 4.1.3). Of the two possible goniometry error sources, solar incidence angle errors and pre-launch characterizations, the latter is by far the dominant one. Pre-launch uncertainties are discussed in Section 1.7.7. Small errors in the solar angles do occur, primarily because each solar measurement is approximately 4 seconds in duration. This smear of 0.22º in solar elevation α can be dealt with by integrating the goniometry function in Equation $G_{ij} = \eta_{ij0} + \eta_{ij1}\cdot\beta + \eta_{ij2}\cdot\beta^2 + \eta_{ij3}\cdot\beta^3 + \eta_{ij4}\cdot\alpha + \eta_{ij5}\cdot\alpha\beta + \eta_{ij6}\cdot\alpha\beta^2 + \eta_{ij7}\cdot\alpha\beta^3 + \eta_{ij8}\cdot\alpha^2 + \eta_{ij9}\cdot\alpha^2\beta + \eta_{ij10}\cdot\alpha^2\beta^2 + \eta_{ij11}\cdot\alpha^3 + \eta_{ij12}\cdot\alpha^3\beta + \eta_{ij13}\cdot\alpha^4$ (4-17 over this smear angle. But the response variation over this range is nearly linear, so correcting at the mid-point of the image incurs negligible errors.

4.2.5 Conversion to irradiances

Table 4-4 Irradiance conversion input/output list

Input	**Input Source**
Corrected signals, C^i_{photon}	internal
Irradiance calibration constants, k^j_{ij}	Sensor calibration database
Pixel goniometric corrections, G_{ij}	internal
Image timing, N_{coadd}, t_{int}	Sensor upload table
Pixel sample table	Sensor upload table
Output	**Output Destination**
Irradiances, F_{meas}	SDR file

The conversion from counts to irradiances proceeds in a manner similar to the Earth signal conversion to radiances discussed in Section 3.2.6. The main difference is that the irradiance conversion operates on C^i_{photon} rather than a C^i_{ideal}, the latter having been corrected for stray light and sensor changes. Since the purpose of F_{meas} is tracking sensor change, use of C^i_{ideal} here would be circular. And since the fractional stray light present in the irradiance measurements is small and not expected to change significantly in time, a stray light correction serves no purpose.

$$F_{meas}(i,j) = \frac{k_{ij}^{i} \cdot C_{photon}^{i}(i,j)}{N_{coadd} \cdot t_{\text{int}} \cdot G_{ij}} \tag{4-18}$$

Sources of uncertainty

The conversion from ideal counts to measured irradiances adds no uncertainty to that already present in C^{i}_{photon}. This is similar to the application of radiance calibrations described in Section 3.2.6. The calibration coefficients k^{i}_{ij} have inherent uncertainties, and these are described in Section 1.7.6.

5 CALIBRATION DATA ANALYSIS

The SDR processes described for Earth and calibration data require various sensor characterization inputs, some of which change in flight. The purpose of in-flight calibration is to monitor these time-dependent parameters and provide for updated corrections as needed. All updated parameters are derived automatically from in-flight calibration data by the SDR algorithm, which places the results in calibration history files. More detailed calibration evaluations are also conducted to provide monitoring of secondary parameters or alternate methods of calibration monitoring. Such secondary evaluations are not described here. A data flow for automated calibration data analysis is shown in Figure 5.1. It is worth noting that of all the calibration parameters monitored by these algorithms, only pixel dark currents will assuredly change. The calibration history files produced by the SDR process are made available to the main data processing arms should the need arise to modify calibration parameters.

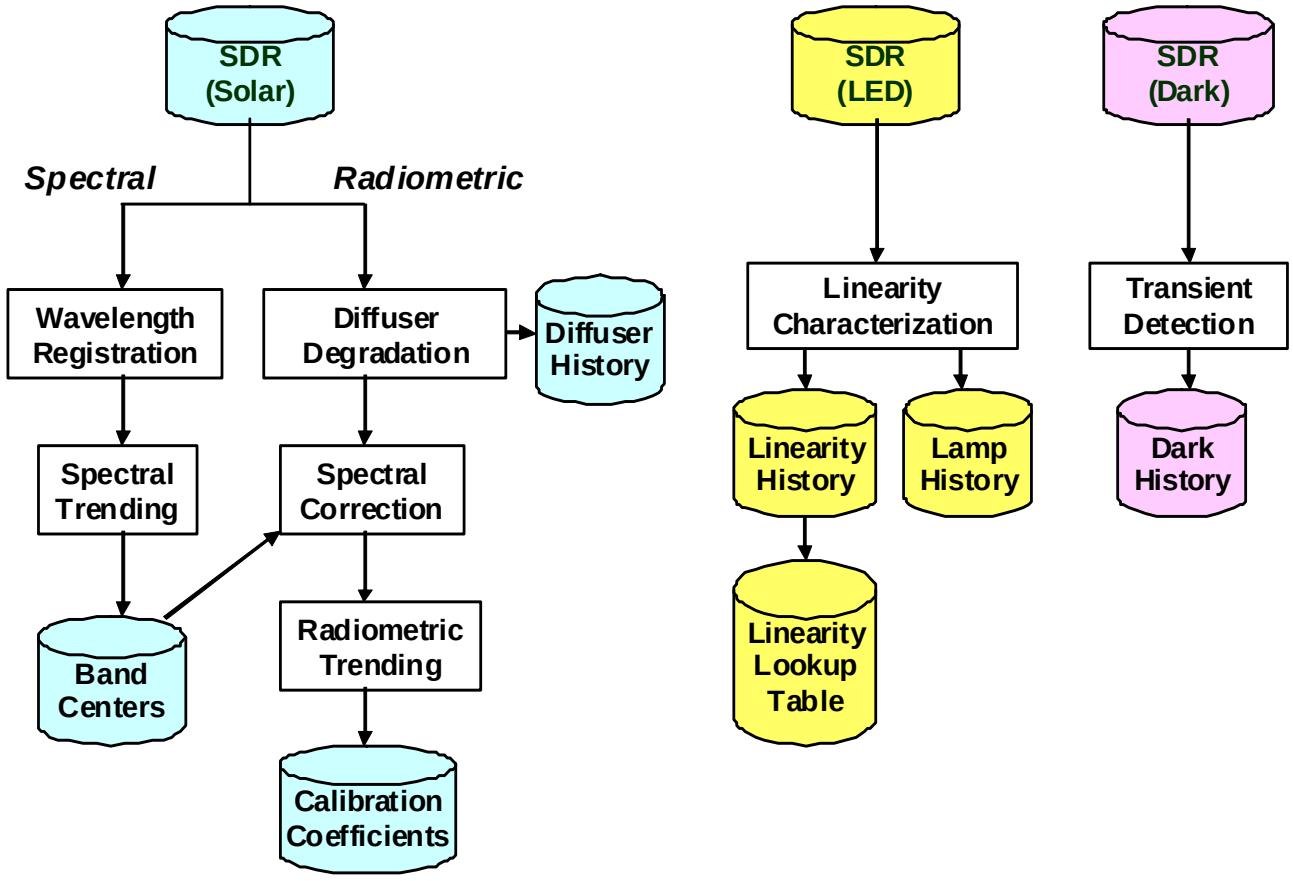

Figure 5-1 Schematic showing the Calibration SDR analysis processes.

5.1 Wavelength registration

Table 5-1 Wavelength registration input/output list

Input	**Input Source**
Measured solar spectrum, $F_{meas}(i,j)$	Calibration SDR
Reference solar spectrum, F_{ref}	Operational Parameter File
Pixel band pass functions, S_{ij}	Sensor calibration database
Fused silica oscillator strengths, B_k	Operational Parameter File
Fused silica resonance wavelengths, λ_k	Operational Parameter File
Output	**Output Destination**
Shift coefficients, A, n_o^2	Calibration History File

Spectral registration is the assignment of band center wavelengths to the CCD pixels. The band center is defined as the area-weighted mean of the slit function $S_{ij}(\lambda)$. The method for performing spectral registration is to match an in-orbit measured solar irradiance spectrum to a reference spectrum. The reference spectrum is based on a high resolution sun spectrum with an accurately known wavelength scale. The reference spectrum used for OMPS/LP has previously been used for OMI spectral registration.

The matching process is performed on pre-selected regions of the solar spectrum that are known to contain both stable and distinctive Fraunhofer structure. For OMPS/LP these fitting windows extend from approximately 300-350 nm and 400-500 nm. During each solar measurement sequence a full solar spectrum is obtained at every spatial position (CCD column) within each of the 6 aperture regions. A registration match is performed for each of these ~600 spectra.

Unlike grating spectrometers the OMPS/LP prism produces a dispersion that is highly non-linear. The spectrometer dispersion relation describes the wavelength of the dispersed light as a function of the physical distance in the spectral dimension of the focal plane. The non-linear dispersion of a prism results in a highly compressed spectrum at NIR wavelengths. This characteristic lends itself to spectral registration against the Fraunhofer spectrum which has the most structure at the blue and ultraviolet end of the spectrum. Changes in spectral registration between 500 and 1000 nm must be inferred from changes measured at shorter wavelengths. This requires independent knowledge of the dispersion relation over the full measurement range of the sensor.

Dispersion in a prism results from variation in the material's index of refraction with wavelength. For the equilateral OMPS/LP prism the angle θ of light exiting the prism is related to its index of refraction n by the following equation.

$$n^2 = (4/3)(\sin^2\theta + \sin\theta\sin\theta_i + \sin^2\theta_i) \quad (5\text{-}1)$$

The incidence angle θ_i at the front face of the prism is assumed to be constant. The index n is actually the ratio of the fused silica index of refraction to that of the surrounding medium. In the small angle approximation the exit angle θ is replaced with $\theta_o + \delta\theta$, where θ_o is a fixed angle falling within an OMPS/LP aperture. The angular shift (aka dispersion) $\delta\theta$ is found by expanding Equation $n^2 = (4/3)(\sin^2\theta + \sin\theta\sin\theta_i + \sin^2\theta_i)$ (5-1 about θ_o.

$$\delta(n^2) = (4/3)\cdot(2\sin\theta_o + \sin\theta_i)\cdot\cos\theta_o\cdot\delta\theta \quad 5\text{-}2)$$

Equation $n^2 = (4/3)(\sin^2\theta + \sin\theta\sin\theta_i + \sin^2\theta_i)$ (5-1 is then rewritten in expanded form

$$\begin{aligned} n^2 &= n_o^2 + \delta(n^2) \\ &= p\cdot\delta\theta + n_o^2 \end{aligned} \quad (5\text{-}3)$$

Where $p = 4/3\cdot\cos\theta_o\cdot(2\sin\theta_o + \sin\theta_i)$ is a constant with a value less than 2. Over the range 300-1000 nm n^2 for fused silica varies by ~0.06, which yields $\delta\theta < 2^o$. The small angle approximation is therefore applicable. The dispersion $\delta\theta$ relates to the physical dimension on the detector via

$$\delta\theta = f\cdot(i - i_o) \quad 5\text{-}4)$$

where i_o is the spectral pixel index where $\theta = \theta_o$ and f scales the spectral index to radians.

Combining Equations $\begin{aligned} n^2 &= n_o^2 + \delta(n^2) \\ &= p\cdot\delta\theta + n_o^2 \end{aligned}$ (5-3 and $\delta\theta = f\cdot(i - i_o)$ 5-4 relates the pixel index on the detector to the index of refraction of the prism.

$$n^2 = A*(i - i_o) + {n_0}^2 \quad (5\text{-}5)$$

where A is simply a new constant formed from the product of p and f. What remains is to connect index of refraction to wavelength. This is described quite accurately by the Sellmeier Equation (see for example Jenkins and White, section 23.5),

$$n^2(\lambda) - 1 \quad = \quad \lambda^2 \sum_{k=1}^{3} \frac{B_k}{\lambda^2 - {\lambda_k}^2} \tag{5-6}$$

where λ is the wavelength at which the refractive index, $n(\lambda)$, is being calculated, and the three B_k (oscillator strengths) and three λ_k (resonant wavelengths) values are parameters characteristic of the fused silica (Dynasil 1103) used to make the prism.

Finally, the model relating pixel index *i* on the detector with wavelength λ_i is written

$$1 + \lambda_i^2 \sum_{k=1}^{3} \frac{B_k}{\lambda_i^2 - {\lambda_k}^2} \quad = \quad A \cdot (i - i_o) + {n_0}^2 \tag{5-7}$$

In the spectral matching process the free parameters in Equation $1 + \lambda_i^2 \sum_{k=1}^{3} \frac{B_k}{\lambda_i^2 - {\lambda_k}^2} \quad = \quad A \cdot (i - i_o) + {n_0}^2$ (5-7 are determined for the minimum χ^2 between the measured and modeled spectrum. A modeled spectrum is written as a function of the pixel index *i*,

$$F_{\mathrm{mod}}(i) \quad = \quad \left(c_0 + c_1 \cdot \lambda_i + c_2 \cdot \lambda_i^2\right) \int F_{ref}(\lambda) \cdot S_i(\lambda - \lambda_i)\, d\lambda \tag{5-8}$$

where λ_i is derived from Equation $1 + \lambda_i^2 \sum_{k=1}^{3} \frac{B_k}{\lambda_i^2 - {\lambda_k}^2} \quad = \quad A \cdot (i - i_o) + {n_0}^2$ (**5-7** as the free parameters are adjusted in the regression.

$F_{mod}(i)$	The modeled solar irradiance in measured pixel *i*
λ_i	Band center wavelength of pixel *i*; a derived free parameter
c_0, c_1, c_2	Polynomial scaling function to match modeled and measured signal intensities; free parameters
$F_{ref}(\lambda)$	Fine resolution reference solar spectrum ; fixed function
$S_i(\Delta\lambda)$	Bandpass function for pixel *i*; fixed function

The regression is implemented using a Levenberg-Marquardt approach to χ^2 minimization.

Following the computation of λ_i, each band center wavelength is shortened to compensate for the red-shift caused by the 7.44 km/s NPP spacecraft motion away from the sun at the northern terminator. Since this velocity is far less than the speed of light *c*, the following approximation applies to computing the true wavelength λ_t. The mean component of velocity away from the sun, v = 6.90 km/s, is used in the following equation to compute the amount of shortening.

$$\frac{\lambda_i - \lambda_t}{\lambda_t} = \frac{\mathrm{v}}{c} \tag{5-9}$$

Since this correction is small and nearly constant for all solar measurements, it need only be applied to the baseline wavelength scale. Subsequent wavelengths are derived from shifts relative to the baseline values, so they automatically include the correction.

Sources of uncertainty

Equation (5-7 is used to detect changes in wavelength registration with pixel index. This equation fundamentally describes changes $\delta\theta$ in the exit angle from the prism as a result of changes in the index of refraction. However, it will also accommodate other changes such as variations in the incidence angle at the prism and rotations of the prism.

$$1 + \lambda_i^2 \sum_{k=1}^{3} \frac{B_k}{\lambda_i^2 - \lambda_k{}^2} = A \cdot (i - i_o) + n_0{}^2$$

The main sources of post-launch spectral registration shift are expected to be 1) thermally induced translation of the detector and 2) changes in the index of refraction. Thermal expansion of the detector is not expected, since its temperature is tightly controlled. Detector motions transverse to the optical axis are essentially pixel index shifts, accounted for by the i_o term in Equation (5-7.

$$1 + \lambda_i^2 \sum_{k=1}^{3} \frac{B_k}{\lambda_i^2 - \lambda_k{}^2} = A \cdot (i - i_o) + n_0{}^2$$

Motions along the optical axis appear as changes in the magnification factor f in Equation 5-4. A

$$\delta\theta = f \cdot (i - i_o)$$

non-uniform shift, often referred to as a stretch or squeeze, is not accounted for except when related to the index of refraction. There are no additional mechanisms known for this spectrometer design that will result in a significant stretch or squeeze.

Since the main causes for band center shifts are accommodated well by the model, remaining errors should stem from statistical uncertainty. Averaged solar measurements have typical signal to noise ratios in the thousands, and there are of order 100 pixels contributing to each regression, so these uncertainties can be very small. Heritage sensors using solar Fraunhofer structure for wavelength registration have rarely achieved uncertainties better than 1/100 pixel. This uncertainty arises primarily due to systematic differences between the measured and reference spectra.

5.2 Spectral trending

Table 5-2 Spectral trending input/output list

Input	Input Source
Baseline wavelength registration, $\lambda_{b\,ij}$	Operational Parameter File
Shift coefficients (full history), A, $n_o{}^2$	Calibration History File

Output	Output Destination
Wavelength registration, λ_{ij}	Earth-view and Calibration SDR

Spectral registration using solar measurement data is described in Section 5.1. A value for the spectral shift relative to an initial scale is obtained for each new spectrum processed through the algorithm. This shift is embodied in the parameters A and n_o^2 from Equation

$$1 + \lambda_i^2 \sum_{k=1}^{3} \frac{B_k}{\lambda_i^2 - \lambda_k^2} = A \cdot (i - i_o) + n_0^2 \quad \text{(5-7,}$$

which are maintained in a history file. Approximately 600 spectra (100 in each aperture region) are available for each solar measurement sequence. Initial spectral assignments are obtained from the baseline solar measurement sequence. Each of the 600 shift parameters and associated uncertainties are appended to the wavelength history file.

Depending on the exact cause for a spectral shift, it may or may not exhibit spatial dependence, i.e. vary across the 100 spectra. There is no reason to expect shifts to differ between aperture regions, though this cannot be ruled out either. In summary, the approach to characterizing wavelength history will depend upon the how the sensor performs in flight. The SDR algorithm currently assumes that sensor wavelength shifts will occur as expected, which means that averaging the ~600 shift parameters is appropriate. The wavelength trend software applies a simple linear fit in time to shift parameters encompassing no more than the previous 30 days. Since solar measurements always lag Earth measurements, and updated spectral registration is needed for operational processing, the wavelength shift fit is always used in extrapolation. The 30 day limitation arises from the need to adequately track annual cycles that may be present in the wavelength registration. Interpolation rather than extrapolation is used when data are reprocessed with updated calibrations.

The extrapolated values of A and n_o^2 are reintroduced into Equation

$$1 + \lambda_i^2 \sum_{k=1}^{3} \frac{B_k}{\lambda_i^2 - \lambda_k^2} = A \cdot (i - i_o) + n_0^2 \quad \text{(5-7 to}$$

derive new band center wavelengths λ'_{ij} for each pixel. The change in band centers is simply computed by comparison with the wavelength scale $\lambda'_{b\,ij}$ derived from the baseline solar data.

$$\lambda_{ij} = \lambda_{b\,ij} + \left(\lambda'_{ij} - \lambda'_{b\,ij}\right) \quad \text{(5-10)}$$

The default setting for automated wavelength shift adjustments is OFF. This means that shifts will be calculated but not assigned to incoming Earth-view data. This setting will be reevaluated based on post-launch analysis.

Sources of uncertainty

Wavelength shifts are expected to be small and vary slowly throughout the year. Consequently, extrapolations should be quite accurate. A potentially larger source of uncertainty arises from the fact that spectral shifts derived from solar data are applied to Earth-view wavelength registration. Additional shifts in Earth-view radiances result from intra-orbital temperature changes (see

discussion in Section 3.2.1). But solar measurements also incur shifts not present in the Earth-view data.

The primary purpose of the solar diffuser is to provide full illumination of the sensor entrance slits. Because the LP transmissive diffusers produce a distribution of photons peaked in the forward direction (scattering angle near zero), the illumination is non-uniform across the width of each slit. Such non-uniformity results in pixel band centers different than those of measurements where illumination is uniform. Whereas Earth limb measurements result in highly non-uniform illumination along each slit, it is relatively uniform across the width. The resulting offset between the two scales does not present a problem for monitoring unless the solar measurement uniformity changes. In fact the uniformity does change slightly as the solar azimuth varies through the year. Figure 1-22 suggests that the sensor response change with solar azimuth is close to linear, but these results are not necessarily indicative of changes in slit illumination uniformity.

Though it should be small, as of this writing the magnitude of this effect is unknown. Validation of wavelength shifts derived from solar measurements will come from Earth limb measurements, where the solar Fraunhofer structure is also observed. Should this validation indicate significant errors in the solar measurements, a correction for slit illumination can be employed at that time.

5.3 Radiometric calibration trending

Table 5-3 Radiometric trending input/output list

Input	**Input Source**
Solar measurements, $F_{meas}(i,j)$	Calibration History File
Spectral correction factors, γ_{ij}	Calibration History File
Output	**Output Destination**
Calibration correction factors, κ_{ij}	Calibration History File

Section 4.1 describes the approach used to maintain radiometric calibration as the sensor changes in flight. Specifically, Equation 4-3 defines an ideal signal C^r_{ideal} in terms of measured signal (corrected for all electronic and stray light effects), solar measurement changes, and diffuser transmission changes. In the absence of diffuser degradation, radiometric trending is concerned with characterizing long-term changes in the solar measurement. Since diffuser degradation is generally small, though not negligible, it is treated as separate correction.

$$C^r_{ideal}(i,j,t) = C^r_{meas}(i,j,t) \cdot \frac{F_{meas}(i,j,0)}{F_{meas}(i,j,t)} \cdot \frac{T_{ij}(0)}{T_{ij}(t)}$$

$$= \kappa(i,j,t) \cdot C^r_{meas}(i,j,t)$$

For the reasons discussed in Section 4.1.2, radiometric changes resulting from shifts in spectral registration are backed out of the solar measurements prior to radiometric trending. This is

accomplished by applying a correction factor γ_{ij} to the baseline solar measurements $F_b(i,j)$ to place them on the same spectral scale as measurements made at time t.

$$F_b'(i,j) = \frac{F_b(i,j)}{\gamma_{ij}} \qquad \text{where} \quad F_b(i,j) = F_{meas}(i,j) \text{ at } t = 0 \tag{5-11}$$

In this equation γ_{ij} are a set of correction factors that depend on the wavelength scale λ_{ij} at time t and the baseline wavelength scale $\lambda_{b\,ij}$ at $t = 0$. These factors are computed using a high resolution solar reference spectrum after convolution over the sensor band pass functions.

$$\gamma_{ij} = \frac{\int S_{b\,ij}(\lambda - \lambda_{b\,ij}) \cdot F_{ref}(\lambda)\, d\lambda}{\int S_{ij}(\lambda - \lambda_{ij}) \cdot F_{ref}(\lambda)\, d\lambda} \tag{5-12}$$

In this expression $S_{b\,ij}$ refers to the band pass function of pixel i,j as it existed during the baseline solar measurements, and S_{ij} is the current function. The band center pixel wavelengths at time t are reported in the SDR output.

The normalized solar measurements $F_{meas}(i,j)$ / $F'_b(i,j)$ are accumulated in a calibration history file

$$C^r_{ideal}(i,j,t) = C^r_{meas}(i,j,t) \cdot \frac{F_{meas}(i,j,0)}{F_{meas}(i,j,t)} \cdot \frac{T_{ij}(0)}{T_{ij}(t)}$$
$$= \kappa(i,j,t) \cdot C^r_{meas}(i,j,t)$$

for use in the radiance corrections given in Equation 4-3. These are equal to κ_{ij} in the absence of diffuser degradation. Rather than simply using the latest solar measurement for these corrections, which will include measurement noise, the algorithm performs a linear fit to the previous 10 normalized measurements. The choice of 10 is based on an optimization from earlier instruments, and may not prove optimum for OMPS/LP. The fit reduces the effects of measurement noise and minimizes discontinuities between successive solar measurements caused by a steady change in sensor response. Since the infrequent solar measurements always lag Earth measurements, fit results are used in extrapolation. Interpolation rather than extrapolation is used when data are reprocessed with updated calibrations.

The default setting for automated radiance calibration adjustments is OFF. This means that corrections will be calculated but not assigned to incoming data. This setting will be reevaluated based on post-launch analysis.

Sources of uncertainty

Retrieval algorithms often use paired or otherwise combined measurements to reduce sensitivity to radiometric changes. Radiometric trending takes advantage of this fact to further reduce trend calibration errors. Solar measurement errors tend to be dominated by goniometry correction errors. Since the goniometry of OMPS/LP has little or no spatial dependence and only a weak spectral dependence, many of the errors cancel in the ratio between pixels. Rather than fitting individual

pixel measurement s, the fit is applied to a ratio of measurements $r = s / s_{ref}$ and to s_{ref}, where the s_{ref} is from another pixel, or set of pixels, used by retrieval algorithms for normalization. An example of s_{ref} is pixel signals from the normalization altitude but at the same wavelength as s. The fit prediction $\langle r \rangle$ is much more accurate than $\langle s \rangle / \langle s_{ref} \rangle$ due to the large but correlated errors in s and s_{ref}. Reconstituted measurements are calculated from $\langle s \rangle = \langle r \rangle \cdot \langle s_{ref} \rangle$. A plausible scenario involves statistically significant changes in s and s_{ref}, but no observed change in r. In this situation the value of r can be kept constant while only s_{ref} is trended. The key to this approach is to use the same ratios as employed by the retrieval algorithm. A similar technique can be employed using triplets and other wavelength combinations.

5.4 Linearity trending

Table 5-4 Linearity trending input/output list

Input	**Input Source**
LED measurements, C_{int} , C_{ref}	Calibration SDR
LED integration times, t_{int}	Calibration SDR
Linear signal level and time, C_{cal} , t_{cal}	Operational Parameter File
Reference signal during calibrations, $C_{ref}(cal)$	Operational Parameter File
Output	**Output Destination**
Linearity polynomial coefficients, $a,b,c,...$	Calibration History File
Discrete linearity corrections, $C/\ell(C)$	Calibration History File

Linearity of sensor response is monitored using processed LED signals. Per Table 4-2, only smear corrections are applied to these data. Linearity corrections are omitted for obvious reasons. Dark signal corrections are omitted because these signals contribute to the overall signal level that is subject to non-linearity. In other words, non-linearity predominantly occurs in the detector output amplifier and downstream electronics, which is independent of how the electrons are produced. The CCD detector also exhibits non-linear response under extreme conditions, but it is operated in a manner to avoid these conditions.

The basis of in-flight linearity characterizations is the comparison of the electrons measured in a pixel well with the expected number. The expected signal is controlled by integration times, so linearity is effectively measured against the highly accurate timing clock. The linearity ℓ_{int} of the system at a specific signal level C_{int} can be written as the ratio of measured and expected signals at an integration time t_{int},

$$\ell_{\text{int}} = \frac{C_{\text{int}}}{\langle C_{\text{int}} \rangle} \tag{5-13}$$

where the expected, or ideal, signal

$$\langle C_{\text{int}} \rangle = \frac{t_{\text{int}}}{t_{cal}} \cdot C_{cal} \tag{5-14}$$

is defined in terms of a signal level C_{cal}, obtained at integration time t_{cal}, where the sensor is assumed linear. The value C_{cal}, which must be the same as was used to correct pre-launch radiometric calibration data, has a value of 12,000 counts.

Because the output of the LED and the pixel quantum efficiencies can drift in time, linearity in flight is measured relative to a reference signal C_{ref} is measured at during integration time t_{ref}. An LED linearity measurement sequence consists of sequential images of progressively longer integration times t_{int} interleaved with reference measurements. This interleaving helps to mitigate the effects of lamp drift within the sequence itself. It is important to note that $t_{ref} \neq t_{cal}$.

Unless corrections are made for short-term and long-term lamp drift, resulting changes in C_{int} will falsely appear as linearity changes via Equation $\ell_{\text{int}} = \frac{C_{\text{int}}}{\langle C_{\text{int}} \rangle}$ (5-13. A corrected signal C_{int}* can be defined in terms of the ratio of reference measurements during pre-launch calibrations and in flight.

$$C^*_{\text{int}} = C_{\text{int}} \cdot \frac{C_{ref}(cal)}{C_{ref}(now)} = C_{\text{int}} \cdot \frac{2C_{ref}(cal)}{C_{ref}(\text{int}-1) + C_{ref}(\text{int}+1)} \tag{5-15}$$

The effective C_{ref} is found through interpolation between reference measurements straddling the integration time of interest. Replacing C_{int} with C_{int}* in Equation $\ell_{\text{int}} = \frac{C_{\text{int}}}{\langle C_{\text{int}} \rangle}$ (5-13 yields the following expression for ℓ_{int}.

$$\ell_{\text{int}} = \frac{2C_{\text{int}}}{C_{ref}(\text{int}-1) + C_{ref}(\text{int}+1)} \cdot \left[\frac{C_{ref}(cal)}{C_{cal}} \cdot \frac{t_{cal}}{t_{\text{int}}} \right] \tag{5-16}$$

In the above equation only the first term changes with successive LED linearity sequences. The term within the brackets is determined prior to launch and is fixed for a given integration time.

For each LED linearity sequence a series of ℓ_{int} values (currently 41) are computed and stored for every sampled pixel. Since linearity is independent of the pixels selected, the system linearity can, in principle, be characterized using sequence data from a single pixel. Combining results from multiple pixels reduces the effects of noise and helps to fill in gaps over the full range of C_{int}* caused by the discrete integration times. The algorithm performs a linear regression on the ensemble of ℓ_{int} values of the form

$$\frac{1}{\ell} = 1 + aC_{\text{int}} + bC_{\text{int}}{}^{2} + \ldots \tag{5-17}$$

and stores the resulting coefficients in a linearity history file. The algorithm also evaluates this polynomial at every possible integer value of C. The possible values range from 0 to 2^{14} - C_{bias}. The values $C/\ell(C)$ are stored in the linearity upload table for possible upload to the instrument. This same lookup table is used by the SDR algorithm for correcting non-linearity in the calibration data (see Section 4.2.2).

The default setting for automated linearity correction updates is OFF. This means that new corrections will be calculated but not used to process incoming calibration data or uploaded to the sensor. This setting will be reevaluated based on post-launch analysis.

5.5 Diffuser degradation monitoring

Table 5-5 Diffuser monitoring input/output list

Input	**Input Source**
Measured solar signals, W_{ij} , R_{ij}	Calibration History File
Output	**Output Destination**
Working diffuser change, r_j	Calibration History File

The basic approach for determining Working diffuser changes is described in Section 4.1.3, where the Working to Reference signal ratio was introduced. The actual solar measurements when the Reference diffuser is deployed involves Working diffuser measurements on the orbits immediately preceding and following the Reference measurement. The following estimate is used for the diffuser ratio.

$$r_{ij}(\text{orbit } n) \;=\; \frac{W_{ij}(\text{orbit } n-1) + W_{ij}(\text{orbit } n+1)}{2R_{ij}(\text{orbit } n)} \tag{5-18}$$

W_{ij} and R_{ij} represent individual pixel signals from the Working and Reference diffusers, respectively, averaged over a solar measurement sequence. Each pixel along a column (spectral dimension) measures a unique diffuser change. Since the solar diffusers are near a sensor aperture, each pixel's view of the diffuser surface overlaps that of adjacent pixels. Consequently, the values r_{ij} from many pixels along a row i can be combined without loss of information. The following values are stored in a diffuser history file for each of the 6 aperture images.

$$r_j = \frac{1}{n_{col}} \sum_i r_{ij} \tag{5-19}$$

The algorithm takes no further action with these data. The values are monitored for change, and any observed change is evaluated in terms of retrieval algorithm sensitivity. Should a correction become

necessary, the spectral dependence of r_j will be characterized and the result entered into Equation (4-9. A

$$\frac{dW}{W} = \frac{n_W}{n_W - n_R}\frac{dr}{r}$$

Working diffuser transmission correction computed via Equation (4-13) will be entered automatically into

$$\frac{T(t,\lambda)}{T(0,\lambda)} = 1 - \left(\frac{dW}{W}\right)$$

the corrections described in Equation 4-3.

$$C^r_{ideal}(i,j,t) = C^r_{meas}(i,j,t) \cdot \frac{F_{meas}(i,j,0)}{F_{meas}(i,j,t)} \cdot \frac{T_{ij}(0)}{T_{ij}(t)} = \kappa(i,j,t) \cdot C^r_{meas}(i,j,t)$$

5.6 Dark current calculation

Table 5-6 Dark current input/output list

Input	**Input Source**
Measured dark signals, $C_{image}(i,j)$, $C_{stor}(i,j)$	Calibration SDR
Dark integration times, t_{image}, t_{stor}	Calibration SDR
Output	**Output Destination**
Dark currents, $D_{imag}(i,j)$, $D_{stor}(i,j)$	Calibration History File

The dark current of an individual pixel in a CCD is relatively constant, shot noise notwithstanding, provided the detector is operated under stable conditions. As with other CCD-based sensors, the OMPS/LP detector is designed to maintain a constant temperature even while the temperature of the remaining optics and electronics fluctuates. One change that is difficult to prevent is lattice damage caused by energetic solar protons. This damage has the effect of increasing the statistical probability that thermal electrons are excited into the conduction band of the CCD. The result is increasing pixel dark currents as the time in orbit increases. Since the lattice is damaged by a small fraction of the particle hits, the time between steps in current can be considerable. Such increases are quite manageable, provided each pixel's dark current is carefully monitored.

OMPS/LP utilizes dedicated measurements during Earth eclipse to collect dark signals. Due to the manner in which image pixel electrons are read out, the dark electrons in a single image pixel are actually collected in multiple places within the CCD. Besides the image pixel itself, dark electrons are primarily collected in storage region pixels and serial register pixels. Since the number of electrons collected is proportional to the time the signal resides in each region, dark electrons collected in the serial register are ignored. Dark electrons are contributed by the image and storage regions in proportions defined by Equation

$$C_{dark}(i,j) \quad = \quad N_{coadd}\left[D_{imag}(i,j)\cdot t_{\text{int}} + \sum_{1}^{i} D_{stor}(i,j)\cdot t_{stor}\right] \qquad \text{(3-15.}$$

Image and storage region dark currents are separately characterized in dedicated measurement sequences.

Once collected, these measurements are stored in separate calibration history files. Due to the stepwise increases in dark currents, it makes no sense to apply a fit to a pixel's dark current history. Rather, the most recent measurement is treated as the best estimate of the dark current in a given pixel.

The default setting for automated dark signal corrections is ON. This means that updated dark current corrections will be calculated and applied to incoming data. This setting will be reevaluated based on post-launch analysis.

6 REFERENCES

Bevington, P.R. (1969), *Data reduction and error analysis for the physical sciences*, McGraw Hill, New York.

Flynn, L.E., Seftor, C.J., Larsen, J.C., Xu P. (2007), The Ozone Mapping and Profiler Suite (OMPS), Earth Science Satellite Remote Sensing, Springer-Verlag and Tsinghua University Press.

Frederick, J.E, R. P. Cebula, and D. F. Heath (1986), Instrument characterization for the detection of long-term changes in stratospheric ozone: An analysis of the SBUV/2 radiometer, *J. Atmos. Oceanic Technol.*, **3**, 472-480.

Graf, P.H., I. Becker, M. Chrisp, M. Dittman, W. Fowler, P. Hendershott, G. Jaross, J. Larsen, P. Mehalko, D. Michaels, V. Minerva, J. Qu, R. Rathburn, J.V. Rodriguez, C. Seftor, R. Schwiesow, H.F. Snell, T.J. Swissler, R. Tarde and C. Wellemeyer (2000), The Preliminary design of the Ozone Mapping and Profiler Suite (OMPS), in *Atmospheric Ozone : Proceedings of the Quadrennial Ozone Symposium*, Sapporo, Japan 3-8 July 2000, Edited by R.D. Bojkov and K. Shibasaki, International Ozone Commision, 401-402.

Heath, D. F., A. J. Krueger, H. R. Roeder, and B. D. Henderson (1975), The solar backscatter ultraviolet and total ozone mapping spectrometer (SBUV/TOMS) for Nimbus G, *Optical Engineering*, **14**, 323-331.

Hilsenrath, E., R.P. Cebula, M.T. Deland, K. Laamann, S. Taylor, C. Wellemeyer, and P.K. Bhartia (1995), Calibration of the NOAA-11 Solar Backscatter Ultraviolet (SBUV/2) Ozone Data Set from 1989 to 1993 using In-Flight Calibration Data and SSBUV, *J. Geophys. Res.*, **100**, 1351-1366.

Janz, S.J. et.al.,"Calibration of limb sounding instruments for ozone and environmental research", Poster AO.2-0012, 32nd COSPAR Scientific Assembly, Nagoya, Japan, 12-19 July, 1998.

Jaross, G. et al.(1995), Calibration and postlaunch performance of the Meteor 3/TOMS instrument, *J. Geophys. Res.* **100***,* 2985-2995.

Jenkins, F.A.and H.E. White (1976), *Fundamentals of Optics*, Fourth Edition, McGraw-Hill, New York

Leitch, J.W., J.V. Rodriguez, M.G. Dittman, D. Frazier, B.K. McComas, R.H. Philbrick, D. Wasinger, Debra, T.J. Valle, T. Dixon, D. Dooley, R. Munzer, J.C. Larsen, (2003), Limb scatter ozone profiling sensor for the NPOESS ozone mapping and profiler suite (OMPS), *Optical Remote Sensing of the Atmosphere and Clouds III*. Edited by Huang, Hung-Lung; Lu, Daren; Sasano, Yasuhiro. Proc. Of the SPIE, Vol.4891,pp.13-21.

Mauldin, L. E., R. Salikhov, S. Habib, A. Vladimirov, D. Carraway, G. Petrenko, J. Comella (1998), Meteor-3M-/Stratospheric Aerosol and Gas Experiment III (SAGE III), *Proc. SPIE*, 3501, 355-365.

McCormick, M. P., J. M. Zawodny, R. E. Veiga, J. C. Larsen, and P.-H. Wang, (1989). An Overview of SAGE I and II Ozone Measurements, *Planet. Space Sci.*, 37, 1567-1586.

McPeters, R. D., and W. D. Komhyr (1991), Long-Term Changes in the Total Ozone Mapping Spectrometer Relative to World Primary Standard Dobson Spectrometer 83, *J. Geophys. Res.*, *96*(D2), 2987–2993.

McPeters, R.D., S.J. Janz, E. Hilsenrath, T.L. Brown, D.E. Flittner, and D.F. Heath (2000), The retrieval of O_3 profiles from limb scatter measurements: Results from the shuttle ozone limb sounding experiment, *Geophys. Res. Lett.*, *27*, 2597-2600.

Rault, D.F., et al. (2010), Algorithm Theoretical Basis Document (ATBD) for the Environmental Data Record (EDR) Algorithm of the Ozone Mapping and Profiler Suite (OMPS) Limb Profiler.

Assumptions contained in the SDR algorithm

(incomplete)

- Offsets in the flight electronics are all introduced after the sources of non-linearity in the electronic gain.
- No pixels will be brought down binned for which atmospheric absorption must be considered.
- Scene variations are small enough over the 19 sec. image report period that inter-pixel smear content variations along a readout column can be neglected.
- CCD Charge transfer inefficiency results in a negligible error.
- Changes in pixel quantum efficiency in flight are random and are of a magnitude that does not require individual pixel corrections.
- The stray light characteristics of solar irradiance measurements do no change significantly with time in flight.